Improved Understanding of Performance of Local Controls Linking the above and below Ground Components of Urban Flood Flows

Submitted by

Istvan Galambos

to the

University of Exeter

as a thesis for the degree of

Doctor of Philosophy in Engineering

July 2012

I certify that all material in this thesis which is not my own work has been identified and that no material has previously been submitted and approved for the award of a degree by this or any other University.

...dedicated to my family, with love and gratitude...

Abstract

This work is devoted to investigation of the flow interaction between above and below ground drainage systems through gullies. Nowadays frequent flood events reinforce the need for using accurate models to simulate flooding and help urban drainage engineers. A source of uncertainty in these models is the lack of understanding of the complex interactions between the above and below ground drainage systems.

The work is divided into two distinct parts. The first one focuses on the development of the solution method. The method is based on the unstructured, two- and three-dimensional finite volume method using the Volume of Fluid (VOF) surface capturing technique. A novel method used to link the 3D and 2D domains is developed in order to reduce the simulation time.

The second part concentrates on the validation and implementation of the Computational Fluid Dynamics (CFD) model. The simulation results have been compared against 1:1 scale experimental tests. The agreement between the predictions and the experimental data is found to be satisfactory. The CFD simulation of the different flow configurations for a gully provides a detailed insight into the dynamics of the flow. The computational results provide all the flow details which are inaccessible by present experimental techniques and they are used to prove theoretical assumptions which are important for flood modelling and gully design.

Acknowledgements

First of all I would like to express my gratitude to my supervisors, Dr Slobodan Djordjevic and Dr Gavin Tabor for their support and guidance throughout my research carried out at the University of Exeter during the past four years. I appreciate their valuable guidance on the subject and the freedom that gave me to develop my own interests.

I am deeply grateful for Prof. Adrian Saul, Naridah Sabtu and Gavin Sailor for the provision of experimental data. I am thankful to Dr Zeljko Tukovic for helping me clarify many tricky numerical issues. Valuable suggestions of Dr Hrvoje Jasak are gratefully acknowledged.

The research presented in this Thesis was funded through the Flood Risk Management Research Consortium (FRMRC) Research Priority Area X Urban Flood Management, which was lead by Professor Adrian Saul. The Consortium was funded by the UK Engineering and Physical Sciences Research Council under grant GR/S76304/01, jointly with the UK Natural Environment Research Council, the Department of Environment, Food and Rural Affairs, The Environment Agency of England and Wales, the Scottish Executive, the Rivers Agency (Northern Ireland) and the UK Water Industry Research.

Table of Contents

List of Tables

List of Figures

Nomenclature

Normal symbols represent scalar quantities and boldface symbols represent vector and tensor quantities. Generally, boldface Roman symbols represent vector and boldface Greek symbols represent tensor quantities, but this rule is not adhered too religiously

Latin characters

Symbol	Description	Unit
A	Cross-sectional area of flow	m^2
a_P	Diagonal matrix coefficient	variable dependent
a_N	neighbour-cell matrix coefficient	variable dependent
b	Length	m
B	Top width of flow (eq. 2.5)	m
B	Channel width	m
C_{d1}	Discharge coefficient for weir	-
C_{d2}	Discharge coefficient for orifice	-
C_M	De-Marchi coefficient of discharge	-
C_c	Contraction coefficient	-
C_v	Velocity coefficient	-
$\mathbf{d}$	Vector between two cells centre	m
e_M	Kinetic energy	J/kg
E	Specific energy	
$\mathbf{f}$	Acceleration vector due to body forces	m/s^2
Fr	Froude number	
g	Gravitational acceleration	m/s^2
G_k	Production limiter	
h	Water level	mAD
H	Total depth	m

$H(x,t)$	step (Heaviside) function	-
$\boldsymbol{I}$	Identity tensor	
k	Turbulent kinetic energy	J/kg
$\mathbf{k}$	Vector in the orthogonality treatment	m
K_1	Empirical constant	-
K_2	Empirical constant	-
L	Weir length, grating length	m
L'	Length of grating required to capture the flow	m
L_0	Length of grating required to capture the flow travelling on grating	m
$\mathbf{n}$	Unit normal vector	
p	Pressure	Pa
q_1	Flow between the kerb and the grating	m^3/s
q_2	Flow bypassing the outer edge of grating	m^3/s
q_3	flow carried over on the grating	m^3/s
Q	Discharge	m^3/s
Q_b	Bypassing flow	m^3/s
q	Discharge per unit length over the weir	
Re	Reynold number	
S_0	Channel slope	m/m
S_f	Energy slope	
S_f	Cell-face surface-normal vector	m^2
S	Source term	variable dependent
$\mathbf{S}$	Surface area vector	m^2
t	Time	s
$\boldsymbol{u}$	Velocity vector	m/s
v	Velocity	m/s
V	Volume	m^3
w	Weir crest above bed or height	m
W	Weber number	
x	Longitudinal direction	
y_1	Upstream flow depth	m
y_2	Flow depth at the edge	m

y'	Flow depth at the outer edge of grating	m

Greek characters

α	Kinetic energy correction coefficient	
β	Momentum correction coefficient	
δ	Delta function or very small scalar value	
ε	Turbulent energy dissipation rate	J/kgs
ϕ	General scalar property	
γ	Indicator function	
Γ	Diffusivity	
κ	Viscosity ratio or curvature of the interface	
λ	Under-relaxation factor	
μ	Dynamic viscosity	Ns/m^2
ν	Kinematic viscosity	m^2/s
ϖ	Turbulence energy dissipation rate	m^2/s^3
ρ	Density	kg/m^3
σ	Surface tension	N/m
$\boldsymbol{\tau}$	Stress tensor	Pa
χ	General tensorial property	
θ_0	Angle between the road surface and the vertical	

Chapter 1

Introduction

Storm water collection and conveyance systems are critical components of urban drainage systems. Proper design and management of these systems are essential to minimize flood damage and disruptions in urban areas during storm events. Runoff water must be captured mainly by gully inlets. To locate and size these inlets properly, designers need reliable information on their hydraulic performance. Nowadays frequent flood events reinforce the need for using accurate models to simulate flooding and help urban drainage engineers. A source of uncertainty in these models is the lack of understanding of the complex interactions between the above and below ground drainage systems. Such knowledge is essential for enhanced calibration and verification of 1D-2D hydrodynamic modelling approaches (Leandro, et al., 2009). However, general references in this subject disregard the complexity of the interaction between these two systems. They assume the inlet capacity is controlled solely by the inlet type and the flow on the surface (Almedeij & Houghtalen, 2003) or by gully efficiency (Balmforth, et al., 2006). The geometry of the inlet below ground is considered irrelevant. The most common way in which this element has been modelled is either as a weir or as an orifice, or as a combination of these. However, none of these elements are representative of the real flow

conditions. Moreover, the real linking elements include not only the surface inlet, but also the pipe inlet and its connections, the gully pot and the buried sewer pipe connections (Djordjevic, 2009).

1.1 Motivation

The Foresight Future Flooding study (Evans, et al., 2004a) (Evans, et al., 2004b), highlighted the lack of accurate tools and methodologies for the prediction of the cause and extent of urban flooding, and of urban flood impacts. The report also promoted the development of an integrated approach to flood modelling to support accurate analysis of integrated portfolios of flood management responses. The UK flooding in summer 2007 was a wakeup call to challenge scientists and experts to face this problem. The need for investment in developing flood modelling tools became an essential task. There has been significant development of urban flood modelling tools in last few years. These models have been developed to interact the flood flows between the above and below ground drainage systems. The major deficiency in their application relates to the way in which the flows enter the below ground system through inlets/gullies on the catchment surface and, subsequently, when the below ground drainage system is full, how the flows exit through the gullies onto the catchment surface.

Until recently, drainage system models have assumed that there is a "free" connection between the urban surface and the below ground system and vice versa, but it is becoming increasingly evident that this is not the case. In some

areas there is a significant lack of gullies whilst at other locations the gullies may be partially or completely blocked. The way in which these gulley inlets/outlets are described (free discharge, partially or fully blocked) is therefore critical to the accurate prediction of the hydraulic performance of the system. There is a need therefore to better describe the performance of such types of gulley system commonly found in practice. Such understanding is essential to improve the crude representation and uncertainty of existing techniques. This need has also been identified by researchers and the developers of urban flood risk software.

1.2 Objectives

The overall objective of the research described in this thesis was to improve understanding of the interaction between above and below ground elements of urban flood models. The present research focuses on the hydraulics of gully flows. The aim of this study was divided into a number of specific objectives which are presented below:

- Evaluate the application of CFD modelling for simulating flow into and from gullies;
- Examine flow patterns and flow regimes around the gully;
- Develop and test a novel algorithm to link 2D and 3D Computational Fluid Dynamics models;
- Application of CFD modelling to generate new knowledge for improving urban flood models;

- Provide a basis of generalizing hydraulic descriptions for gully flow.

1.3 Structure of thesis

This thesis is divided in six chapters including this introduction.

In Chapter 2 a review of relevant literature is provided. The review covers the main areas of research addressed including grate inlet hydraulics, discharge coefficient, linking surface and subsurface networks, CFD modelling applied in urban drainage.

Chapter 3 provides the description of full scale physical experiment (completed in Sheffield Laboratory) to mimic the hydraulic interaction between the above and below ground drainage system via gully inlet.

In Chapter 4 the mathematical and numerical models are described. A novel methodology, based on finite volume discretization, to link the 3D and 2D domain is proposed.

In Chapter 5 implementation of the proposed model is presented. Both flow into gully and surcharged gully are investigated with the numerical model. Conventional and new methods developed for calculation of discharge coefficient and estimation of bypassing flow rate are presented in this chapter.

In Chapter 6 the key findings of this thesis are summarised and relevant conclusions are drawn. The novel aspects introduced in this thesis are highlighted, followed by possible directions of future research to enhance and extend the methodologies presented.

Chapter 2

Previous and Related Studies

An overview of the literature relevant to this study is presented next. In the first section the studies related to grate inlets are reviewed.

2.1 Grate Inlet

The studies on grate inlets covered multiple interesting fields. Most researchers were keen to investigate the effectiveness of the grate inlet (Larson, 1947), (Li, et al., 1951), (Li, et al., 1954), others proposed several potential modifications on the existing grate inlet designs (Almedeij & Houghtalen, 2003), (Guo, 2000a) (Guo, 2000b). This section does not attempt to review all of the research and literature related to the street inlets but focuses on grate inlets without depression that are located on a gutter.

The literature indicates that there are many factors that contribute to the performance of a gully inlet:

- the type and shape of the grating;
- the transversal and longitudinal street slopes;
- the width and depth of the approaching flow;
- the depth and velocity of flow over the grating;

- the presence of vortices;
- the accumulation of debris.

Depending upon the depth of flow, grate inlets operate under three different conditions of flow:

1. weir flow;
2. transitional flow, indefinable flow because of vortices and other disturbances;
3. orifice flow.

The inlet may operate like a weir when the water depth is shallow, or like an orifice when it is submerged (Guo, 1997) (Guo, 2000a) (Guo, 2000b) (Guo, 2000c) (Mays, 2001). For a grate inlet that operates as a weir, the intercepted flow is given by the equation:

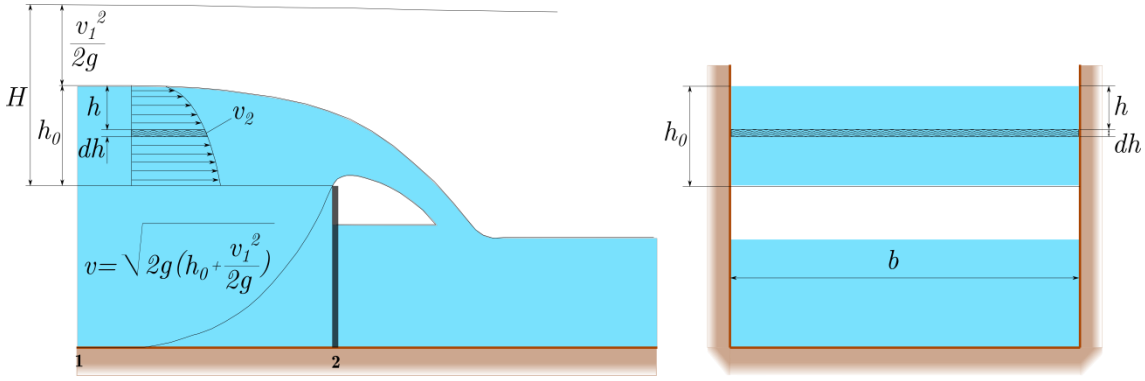

Figure 2.1 – Explanatory diagram for weir equation

$$Q = \int_0^Q dQ = b\sqrt{2g}\int_0^{h_0}\left(h + \frac{v_1^2}{2g}\right)^{\frac{1}{2}} dh = b\sqrt{2g}\,\frac{1}{1.5}\left[\left(h + \frac{v_1^2}{2g}\right)^{1.5}\right]_0^{h_0} \tag{2.1}$$

$$Q = \frac{2}{3}\sqrt{2g}b\left[\left(h_0 + \frac{v_1^2}{2g}\right)^{3/2} - \left(\frac{v_1^2}{2g}\right)^{3/2}\right] \tag{2.2}$$

where, b is the width of weir, h_0 is the water level above weir crest level, v is flow velocity and g is the gravitational acceleration.

Introducing the discharge coefficient to incorporate the local losses:

$$Q = \frac{2}{3} C_{d1} \sqrt{2g} b \left[\left(h_0 + \frac{v_1^2}{2g} \right)^{3/2} - \left(\frac{v_1^2}{2g} \right)^{3/2} \right] \tag{2.3}$$

In case of small velocity the term $-\left(\frac{v_1^2}{2g} \right)^{3/2}$ is negligible or can be included in discharge coefficient (C_{d1}), therefore:

$$Q = C_{d1} \frac{2}{3} \sqrt{2g} b H_1^{3/2} \tag{2.4}$$

The flow over the gully inlet can be assumed to be similar to the flow over the weir, in which case $h_0 = y_1$. In accordance with the procedure applied to compute the discharge: zero pressure distribution, parallel streamlines and neglecting the contraction of the nappe is assumed:

$$Q = \int_0^{y_1} C_c \sqrt{2g(H-z)} b dz = \frac{2b\sqrt{2g}}{3} \left[H^{3/2} - (H - y_1)^{3/2} \right] \tag{2.5}$$

C_s is a contraction coefficient, equal to the ratio between the two cross-section area, z is the vertical distance measured from reference level. Taking into account the convergence of streamlines and rearranging the equation leads to:

$$\frac{Q}{b g^{1/2} y_1^{3/2}} = \frac{2b\sqrt{2g}}{3 b g^{1/2} y_1^{3/2}} \frac{y_2}{y_1} [H^{3/2} - (H - y_1)^{3/2}] \tag{2.6}$$

Introducing $Fr_1 = Q / b g^{1/2} y_1^{3/2}$ we obtain:

$$Fr_1 = \frac{2\sqrt{2}}{3} \frac{y_2}{y_1} \left[\left(\frac{H}{y_1} \right)^{3/2} - \left(\frac{H}{y_1} - 1 \right)^{3/2} \right] \tag{2.7}$$

Considering that

$$\frac{H}{y_1} - 1 = \frac{Fr_1^2}{2} \tag{2.8}$$

the depth ratio is:

$$\frac{y_2}{y_1} = \frac{3Fr_1}{(2 + Fr_1^2)^{3/2} - Fr_1^3} \tag{2.9}$$

Applying the continuity equation between the two sections give us the following equation:

$$\left(\frac{y_1}{y_2}\right)^3 = \frac{Fr_2^2}{Fr_1^2} \tag{2.10}$$

Rearranging

$$Fr_2 = Fr_1 \left[\frac{\left(2 + Fr_1^2\right)^{3/2} - Fr_1^3}{3Fr_1} \right]^{3/2} \tag{2.11}$$

and the theoretical discharge relationship is:

$$Q = Fr_2 b g^{1/2} y_2^{3/2} = Fr_1 \left[\frac{\left(2 + Fr_1^2\right)^{3/2} - Fr_1^3}{3Fr_1} \right]^{3/2} b g^{1/2} y_2^{3/2} \tag{2.12}$$

For transitional flow, the grate inlet capacity is somewhere between the inflows predicted by the weir and orifice flow equations.

Larson's (Larson, 1947) investigation of inlet gratings indicated that the inlet characteristics which are of primary importance in determining inlet interception capacity are: the inlet width (normal to the direction of flow) and the efficiency of inlet openings. He also stated that the characteristic of

approach flow has a significant effect on efficiency. His tests showed that high velocities tend to decrease the inlet capacity due to splashing.

Li (Li, et al., 1951) used dimensional analysis to identify variables which have a significant effect on inlet capacity. The hydraulic tests were conducted at ½ scale model to determine the effect of each identified variable. Li treated the flow bypassing the grating as separate portions of flow. The bypassing flow Q_b is made up of three components:

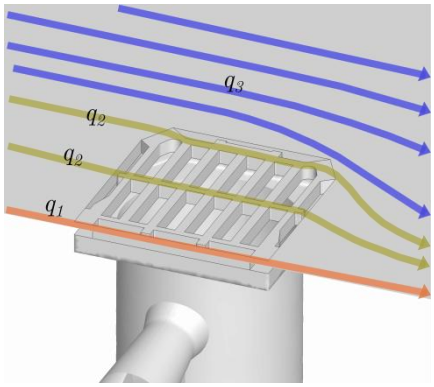

Figure 2.2 – Elements of bypassing flow

1. flow between the kerb and the grating (q_1);
2. flow bypassing the outer edge of grating (q_2);
3. flow carried over on the grating (q_3).

The quantity of flow between the kerb and the grating was neglected in Li's analysis. He found it is small in practice when compared to the main flow. Li found that:

$$q_2 = K_1(L' - L)y'\sqrt{gy'} \tag{2.13}$$

where $K_1 = 0{,}25$, L' is the length of grating required to capture the flow, L is the length of the grating and y' is the depth of flow at the outer edge of the grating. The length of grating required to capture the flow is given by:

$$\frac{L'}{v_0}\sqrt{\frac{g}{y'}} = K_2 \tan\theta_0 \tag{2.14}$$

where θ_0 is the angle between the road surface and the vertical.

Li proposed the following equation for flow travelling over the grating:

$$q_3 = Q_0\left(1 - \frac{L^2}{L_0^2}\right)^2 \tag{2.15}$$

where L_0 is the length of grating required to capture all the flow travelling on grating. It was calculated from the following equation:

$$\frac{L_0}{v_0}\sqrt{\frac{g}{y_0}} = K_3 \tag{2.16}$$

The value of K_3 depends on the ratio of the width of openings to the width of bars.

The design method for grate inlets in HEC-12 is based on Burgi and Grober's (Burgi & Gober, 1978) work. They found that the hydraulic efficiency of grate is improved as the longitudinal slopes increases. They also found that the transverse slope had a large effect on hydraulic efficiency, since steeper transverse slope would concentrate more flow over the inlet.

The inlet bar orientation significantly influences the inlet behaviour. Grate inlets with longitudinal bars are more preferable than inlets with transverse

bars. The transverse bars reduce the effectiveness of the grating because they reduce the effective length of the grating and increase the splashing across the inlet. The study of John Hopkins University (John Hopkins University, 1956) showed that short and wide grating is more effective for general street conditions than long and narrow grating. Bourchard and Towsend (Bourchard & Towsend, 1984) investigation of inlet bar orientation indicated that inlets with transverse bars (90°) are the least effective. Inlets with 135° opening showed good correlation with longitudinal bars for low discharges but less effective for high discharges. The study involved full scale model with different inlet patterns, in which the bar orientation were ranged from 0° to 165° at 15° intervals.

2.2 Discharge Coefficient

Johnson's study (Johnson, 2000) showed that the important variable governing discharge over weirs was H_t/w. The use of this variable, coupled with the inclusion of the weir height in the velocity head, resulted in the formulation of a single curve rather than a family of curves. He also pointed out that the importance of the velocity head should not be neglected.

Kindsvater and Carter (Sturm, 2001) proposed that the effect of Reynolds and Weber number should be included in the discharge equation.

Johnson (Johnson, 2000) and Rehbock (Rehbock, 1929) research showed that the transverse length of the weir has little influence on the discharge coefficient, and this is valid for surface roughness of the weir as well.

Flow over the grating represents a typical example of spatially varied flow with decreasing discharge. Several authors proposed equations for spatially varied flow profile. The dynamic equation of spatially varied flow for over a weir is

$$\frac{dy}{dx} = \frac{S_0 - S_f - \left(\frac{\alpha Q}{gA^2}\right)\left(\frac{dQ}{dx}\right)}{1 - \left(\frac{\alpha Q^2 B}{gA^3}\right)} \tag{2.17}$$

Subramanya (Subramanya & Awashty, 1972), El-Khasab and Smith (El-Kashab & Smith, 1976), Ranga Raju (Ranga Raju, et al., 1979), Hager (Hager, 1987) and Singh (Singh, et al., 1994) used experimental results to evaluate the rectangular weir equation. Swamee (Swamee, et al., 1994) developed elementary discharge coefficients that are related to the discharge through an elementary strip along the side weir.

De-Marchi has introduced the discharge coefficient (Chow, 1959) as:

$$C_d = \frac{3B}{2L}\Phi + const. \tag{2.18}$$

Where Φ is a varied flow function:

$$\Phi = \frac{2E - 3w}{E - w}\sqrt{\frac{E - y}{y - w}} - 3\sin^{-1}\sqrt{\frac{E - y}{E - w}} \tag{2.19}$$

According to Froude number the discharge coefficient can have four different expressions:

$Fr < 0.6$

$$C_d = 0.611\sqrt{1 - \frac{3Fr^2}{Fr^2 + 2}} \tag{2.20}$$

$0.6 < Fr < 1.0$

$$C_d = 0.45 - 0.06(Fr - 0.6) \tag{2.21}$$

$1.0 < Fr < 1.8$

$$C_d = 0.95\sqrt{2 - \frac{3Fr^2}{Fr^2 + 2}} \tag{2.22}$$

$1.8 < Fr$

$$C_d = 0.632 - 0.018(Fr - 1.8) \tag{2.23}$$

Despotovic (Despotovic, et al., 1990) modelled the grating as a series of weirs. All of the slots were modelled as a weir except the outmost ones which were treated as a combination of side weir and weir. The experimental part of the research involved covering up all slots apart from one and measuring the captured flow. This was repeated in turn for all slots. Treating the flow as a combination of side weir and weir at each slots, and assuming the discharge coefficient of weir equal to 0.42, they calculated the discharge coefficient for each side weir. They found it is independent from the Froude number upstream of each slot. However if the slots treated as a weir, then there is a strong relation between the Froude number and the discharge coefficient. The following exponential relationship was suggested:

$$C_d = \exp(-0.453Fr + 0.226) \tag{2.24}$$

Tomanovic (Tomanovic, et al., 1990) applied the above equation for grating in their study and obtained good results at lower cross-falls and flow rates.

Borghei (Borghei, et al., 1999) conducted more than 250 laboratory tests to find the influence of the flow hydraulics and the geometric, channel, and weir shapes on the discharge coefficient. The results show that for subcritical flow the De-Marchi assumption of constant energy is acceptable. He found that the De-Marchi discharge coefficient is a function of the upstream Froude number and the ratios of weir height to upstream depth and weir length to channel width. Borghei proposed the following equation for calculation of discharge coefficient:

$$C_M = 0.7 - 0.48Fr_1 - 0.3\frac{w}{y_1} + 0.06\frac{L}{B} \tag{2.25}$$

Matthew (Matthew, 1963) outlined a simple theory which clearly explains the influence of surface tension, viscosity and streamline geometry on discharge coefficient. Martino and Ragone (Martino & Ragone, 1984) conducted a comprehensive study on the effect of surface tension and viscosity on discharge coefficient.

The study stated that an increase in the influence of surface tension (or reduction in Weber number) will engender an increment in the coefficient of contraction exceeding the decrement in that of velocity, but only for values of Weber number above a certain threshold, which is a function of both slot

breadth and the head. Below the threshold the decrements in the velocity coefficient exceed the increments of the contraction coefficient due to viscosity and to surface tension. Increase in the influence of viscosity (or reduction in Reynolds number) implies an increment in the contraction coefficient, always prevailing over the decrement in that velocity arising from the loss of head due to viscous drag.

Similarly to Martino's research the models proposed by Kindsvater (Kindsvater & Carter, 1957), Getti (Ghetti, 1966), Gavis (Gavis, 1964), Linquist (Linquist, 1929), Datei (Datei, 1966) and Sarginson (Sarginson, 1972) give valuable information on the effect of surface tension and viscosity on discharge coefficient.

De Martino's (De Martino & Ragone, 1979) study concluded that both viscosity and surface tension have each opposite effects on the contraction coefficient C_e and velocity coefficient C_v. The investigation concentrated on Reynolds and Weber numbers and found that reduction in the Reynolds number accompanied by an increase in C_e and decrease in C_v. Similar effects are also caused by an increase in surface tension (a decrease in the Weber number). The fact that C_e and C_v tend to increase and decrease respectively, for an increase in either viscosity or surface tension accounts for the possible arising of conditions when, for values of the Reynolds and Weber numbers below a certain threshold (i.e.. for the slots investigated, for low head values), the reductions in the velocity

coefficient prevail on the increments in the contraction coefficient, so that the discharge coefficient (the product of C_e and C_v) will tend to decrease.
The existence of such conditions was also confirmed by Swift (Swift, 1926) and surmised by Sarpkaya (Sarpkaya, 1958) as well.

Honar (Honar & Keshavarzi, 2008) conducted more than 90 laboratory tests to develop a model for estimation of discharge coefficient in rounded-edge entrance shape and find the influence of non-dimensional hydraulic parameters on the discharge coefficient. It was found that under subcritical flow condition the rounded-edge entrance discharges 10% more flow rate than the squared edge entrance.

2.3 Linking surface and sub-surface networks

The interaction between surface and subsurface drainage network is complicated, while knowledge of their hydraulic characteristics is very limited. A general hydraulic description is yet to be derived. Current practices of gully designs mostly rely on empirical relations from a limited number of experimental studies. Further study to advance the knowledge of gully hydraulics is necessary and valuable, especially when existing drainage systems are challenged today by a combination of urban growth, ageing of sewers and climate change.

Poor knowledge of the hydraulic behaviour of surface drainage structures could produce unreliable simulations from storm water management models (Russo, et

al., 2005) (Gomez & Russo, 2011). Kidd and Helliwell (1977) described the urban runoff process as a two-phase phenomenon including a surface phase and an underground phase. They recognized the complex interactions between these two phases and stated "there is no clear-cut interface between the two phases". Inasmuch as the inlet efficiency governs the amount of water that can enter the drainage system, the above surface and below surface elements cannot be considered separately. Nowadays the lack of knowledge about the hydraulic behaviour of these types of structures has not been fully overcome (Gomez & Russo, 2011).

Three different linkage types are available for dynamically linking the 1D and 2D storm water management models:

1. Point to point link: is a standard link type, coupling between a computational point in the 1D model and a computational point in the 2D model. It can be used to couple upstream river branch to a downstream flood plain.
2. Lateral link: couples the 1D model with 2D domain over a part of the river system. The flow is described through a weir equation in each linked grid point. This type of link can be used for simulation of overtopping levees
3. Structure link: uses 1D model in a 2D domain to model flow through a structure, which is –usually- defined in the 1D model. This type of link is useful for modelling small features which cannot be adequately resolved using the typical grid size of the 2D domain.

With the increasing requirements for integrated modelling, particularly 1D to 2D linking for surface water flooding, a need has arisen to provide a unit to simulate discharge through a manhole or gully from a surcharged culvert.

In ISIS (www.halcrow.com/isis) the manhole outlet can be connected to a dummy boundary unit for linking to TUFLOW (www.tuflow.com), or to a reservoir to represent overland storage. The manhole unit can also incorporate an energy loss term, governed by Bernoulli's equation. TUFLOW has a similar connection to ESTRY as it has to ISIS.

HEC-HMS (www.hec.usace.army.mil/software/hec-hms/)was designed to simulate rainfall-runoff process. The inlet can be represented as a flow diversion and its hydraulic efficiency can be described with the approaching flow – intercepted flow curve.

SWMM (Storm Water Management Model) is a dynamic rainfall-runoff simulation model (www.epa.gov./athens/wwqtsc/html/swmm.html). The routing part of the software transports the runoff through a system of pipes and channels using kinematic or dynamic wave. The hydraulic behaviour of the street is described as an open channel and the inlet is characterised as a divider node describe by hydraulic efficiency data. This is represented by the ratio between total discharge approaching to the inlet and captured flow.

MOUSE (www.dhisoftware.com) is a comprehensive surface runoff, open channel flow and pipe flow modelling package. The behaviour of street inlets can be described with flow depth using the weir equation.

Many different techniques exist to connect the 1D and 2D domains via gullies or manholes. The most frequently used representation of street inlets in numerical models can be summarized as:

- Diversion elements characterized by inflow-captured flow table;
- Diver nodes characterized by inflow-outflow table;
- Weir equation;
- Orifice equation;
- Combination of orifice and weir equation;
- Efficiency-head curve.

2.4 CFD Modelling

Due to the limitation with experimental investigation numerical models seem to be a reliable alternative for studying gully hydraulic performance. Compared to conventional measurements methods, a significant advantage of Computational Fluid Dynamics (CFD) model is the reduction in both the time and cost that are typically required to investigate gully flow. Another important factor, that it can be applied to different environmental condition including those that could not be modelled under laboratory conditions. It has been widely accepted that a good numerical model can be complementary to experimental tests. CFD is a tool that has tended to be used in "high-tech" industries. However, computational power has become more affordable and CFD is getting more frequently used in urban drainage. The published information shows that CFD

is most commonly applied in order to gain detailed design knowledge or to evaluate structural or operational variables (Jarman, et al., 2008).

Huang (Huang, et al., 2002) and Shakibainia (Shakibainia, et al., 2010) used three-dimensional models to compute flow characteristics in 90° junction and showed that most flow structures observed experimentally were accurately simulated.

Fang (Fang, et al., 2010) investigated the efficiency of curb inlets using three-dimensional CFD model. The model used a finite-volume-finite-difference method to discretise the 3D Reynolds Averaged Navier-Stokes equations in fixed Eulerian rectangular grid system. Simulation runs were performed for 1.52 m and 4.56 m opening at various longitudinal and cross slopes. Simulated intercepted flow rate agreed well with laboratory test. The simulation results were used to develop a linear regression equation between inlet efficiency and water spread.

Stovin (Stovin & Saul, 1998), Cullivan (Cullivan, et al., 2004) and Schuetz (Schuetz, et al., n.d.) have used CFD technique to investigate particle tracking in order to assess the separation efficiency in CSO tanks.

Fach (Fach, et al., 2009) study is focused on the development of rating curves exemplarily for CSO structures using three-dimensional CFD model. The study showed that discharge determined by using the standard weir equation together with sonic water depth measurement can significantly differ from the discharge based on CFD simulation. Especially, for side weirs which did not correspond to

the standard weir layout, the results from the CFD model were closer to the reality than the simplified standard weir equation.

The prediction of the water surface profile is fundamental in urban drainage modelling. However this is absent from the majority of the studies in which the free surface was assumed as flat and fixed. Jarman et al (Jarman, et al., 2008) reviewed CFD studies where water surface profiles were not predicted as a part of the solution process. The free surface was approximated by a fixed, horizontal frictionless boundary, predefined as part of model geometry. The investigated models were concerned with the application of CFD for engineering objectives rather than with the development of modelling methodology. The investigation concluded that this type of approach is reducing the computational effort but is not always appropriate.

A similar approach in numerical simulation of free surface flow is when the water surface is replaced by a rigid lid (Mignot, et al., 2012). This is valid only if the free surface does not change much along the domain. In the case of this study the rigid lid approximation likely introduced nonphysical errors.

Ismail and Nikraz (Ismail & Nikraz, 2008) conducted an experimental and numerical analysis to establish the hydraulic characteristics and pollution removal efficiency of the cylindrical screen of VersaTrap. It has been designed to remove suspended solids, floatables and sediments from the storm water and to prevent re-entrainment. A three-dimensional model was constructed using tetrahedral meshes comprising of 268000 computational cells. Inlet flow rates

(11, 13 and 20 l/s) were defined by uniform velocities across the inlet plane. System outlets were defined with a pressure outlet corresponding to atmospheric pressure, representing a free outflow. The VOF model was used to determine the hydraulic characteristics and Eulerian-Eulerian model was used to obtain the efficiency of the system. The simulated peak flow was similar to the experimental results within an error of 22%.

More literature on CFD modelling will be reviewed when CFD methods are introduced with more detail in Chapter 4.

2.5 Conclusion

Urban storm water collection and conveyance systems are critical components of the urban drainage. Proper design of these systems is essential to minimize flood damage and disruptions in urban areas during storm events. Excess water must be captured mainly by gully inlets. To locate and size these inlets properly, designers need reliable information on their hydraulic performance.

Despite of many theoretical and experimental studies carried out on weir, orifice, free overfall, manhole and gully grating the flow calculation for gratings has not been completely solved. As discussed above the general references disregard the interaction between the above and below ground elements of linked 2D/1D or 1D model. None of the expressions presented this chapter are directly valid for modelling the link between surface and sub-surface flow. Most

of the existing models consider a weir or an orifice type link between the two systems. Some of them use a combination of these elements which can switch from one to the other depending on the water level around the edge of gully inlet.

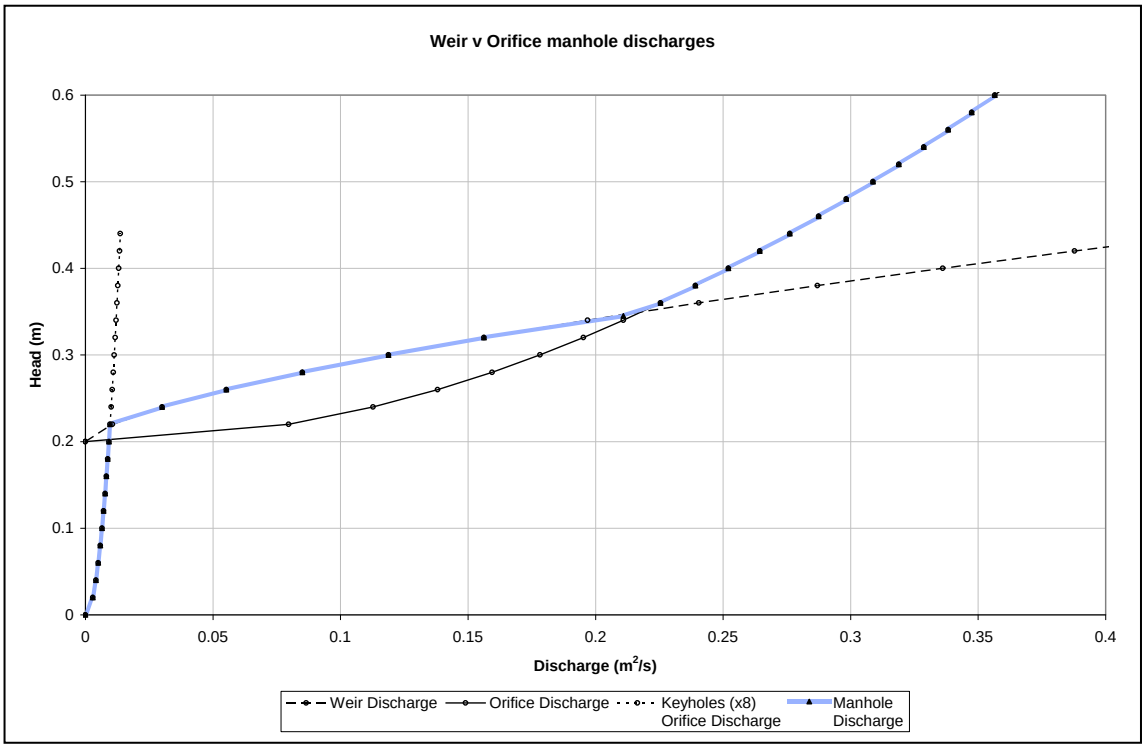

Figure 2.3 – The combined Head-Discharge relationship for manholes/inlets (Allitt, et al., 2009)

The application of combined Head-Discharge curve gives more reliable results than weir or orifice equation. However there are several concerns about this type of calculation method. The main weakness of the combined Head-Discharge curve is the transition zone/zones. Namely, the mechanism of transition and the lower and upper boundary of transition zone are unknown. The method reliable in case of very shallow (less than 1 cm) or deep water (more than 30 cm), but gives uncertain result between this two values.

Regarding the distinct stages and processes for the case of a surcharged drain system the urban flooding simulation models are required to accurately describe the hydraulic phenomena of a surcharged gully, particularly:

- the transition from free surface flow to pressurized flow
- the interaction between surface flow and pressurized flow
- the rise of the water level above surface level

Numerous experiments have been undertaken worldwide in connection with grate efficiency. These are based on the most frequent situation, when the flow direction is from the surface into the gully. The surcharging flow condition is getting more attention nowadays from numerical modellers; however it has not been studied experimentally before. There is a need therefore to better describe the performance of gulley system commonly found in practice. Such understanding is essential to improve the crude representation and uncertainty of existing techniques.

Chapter 3

Description of Physical Experiments completed in the Sheffield Laboratory

A full scale laboratory system has been built at the Water Engineering Laboratory of University of Sheffield to mimic the hydraulic interaction between the above and below ground drainage system via a gully inlet. The physical experiments are not the subject of this thesis but they are used to test the CFD modelling approach; therefore they are described here without too much detail. A comprehensive overview of the physical experiments and analysis of results is given by Sabtu (Sabtu, 2012).

3.1 Experimental rig

3.1.1 Testing platform

The testing platform is a 4.27 m long and 1.83 m wide rectangular area with inlet and outlet tanks of either end of the platform that are each equipped with sluice gates to control the flow rate onto the testing platform. Both the outlet tank and the outflow from the gully are connected to a measuring tank which allows flow rate measurements to be taken. The dimension for the inlet and outlet tank itself is 2.44 m x 0.61 m. The flow for this system is provided by an overhead tank and is circulated through the entire system before being

transferred into a sump to be pumped back to the overhead tank again (Sabtu, 2012).

Figure 3.1 – Experimental rig (viewed from downstream, gully left)

The testing platform was designed as a flatbed representing non-sloping road conditions (Figure 3.1). Longitudinal slopes were later incorporated. For sloping tests, the width of the testing platform has been halved (Figure 3.2) due to the difficulty of depth measurement of very shallow flow.

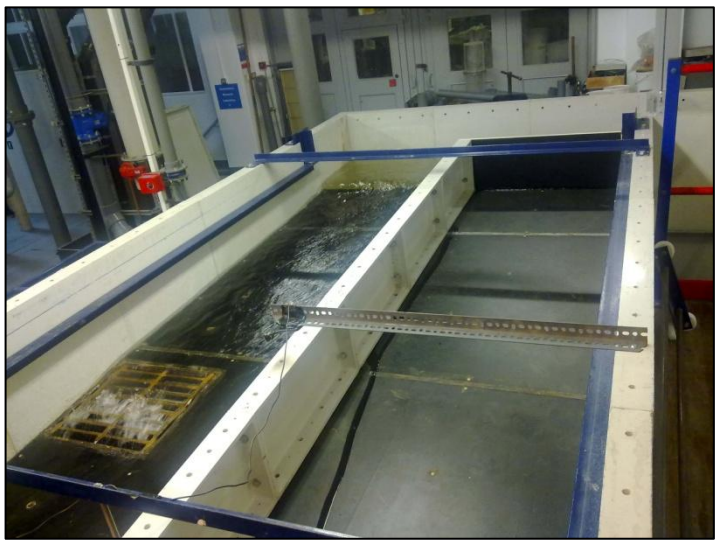

Figure 3.2 – Experimental rig for sloping conditions

3.1.2 Gully and grates

The gully itself is a trapped gully with spigot outlet. This is one of the most commonly used gully type designed with an outlet that forms a water seal and a rodding eye which helps to retain floating pollution within the gully pot. The gully has a 375 mm diameter and 750 mm nominal depth.

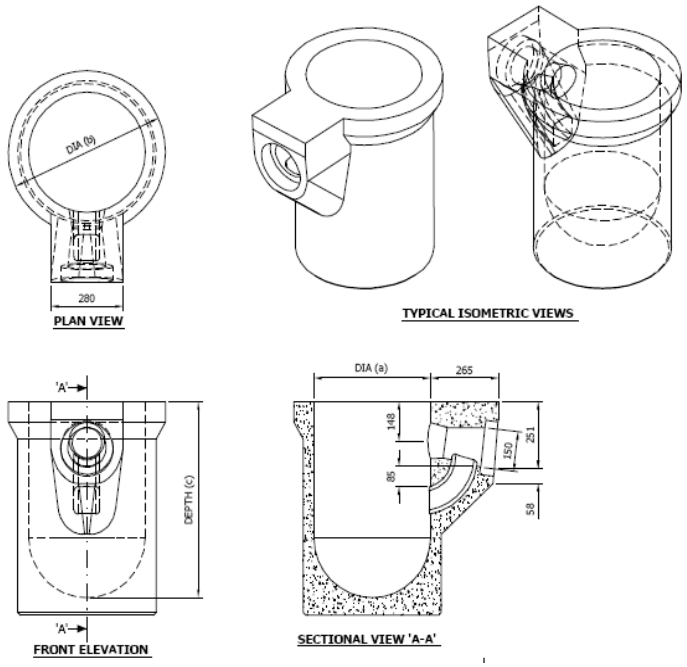

Figure 3.3 – Dimensions of gully pot (Milton Precast)

Figure 3.3 shows the dimensions of the gullies as specified by the manufacturer. The dimensions have been checked against BS5911-6:2004 and are in accordance to the specifications. The physical properties of gully are:

- Internal diameter: 375 mm
- Internal depth: 750 mm
- Outlet diameter: 150 mm
- Inside depth to centre of outlet: 148 mm
- Outside depth of outlet: 251 mm

- Dimension of riser: 85 mm
- Depth of water seal: 85 mm
- Weight: 180 kg

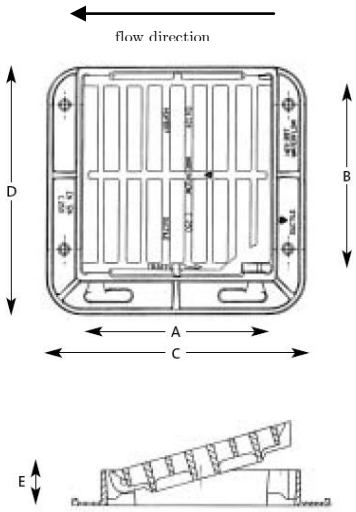

Figure 3.4 – Properties of grates (Sain-Gobain Pipelines, 2007)

Figure 3.4 and Table 3.1 shows dimensions and hydraulic properties of the grates also as specified by the manufacturer.

Table 3.1 – Physical properties of applied grates (Sain-Gobain Pipelines, 2007)

Loading class	Clear opening AxB [mm]	Over base CxD [mm]	Depth E [mm]	Waterway area [cm^2]	HA102 reference
C250	325 x 437	475 x 524	75	933	S
C250	400 x 432	550 x 530	75	1128	R

3.1.3 Pressure transducer and point-gauge

In order to measure the depth of flow, seven pressure transducers have been set up on the rig. Six of these are recessed in the platform and one at the bottom of the gully pot. Figure 3.5 shows the location of the transducers.

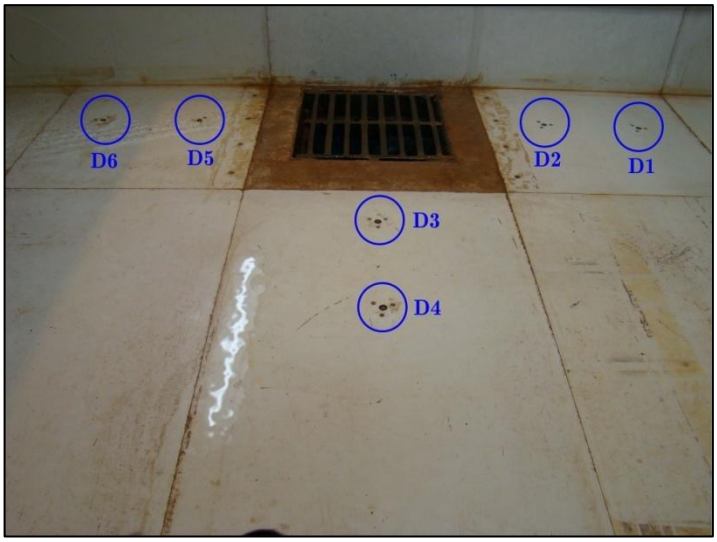

Figure 3.5 – Location of pressure transducers

The GEMS 5000 series (0-30mbar) pressure transducer has been used for the bed and GEMS 5000 series (0-150mbar) for the gully pot. Both sensors give an output of between 4-20 mA and uses 9-35V of supply power. These pressure transducers have been selected due to their long term stability and high accuracy ($\pm 0.2\%$).

Point-gauge measuring equipment (see Figure 3.6) has also been set up in order to calibrate the pressure transducers. A point-gauge is equipment commonly used to measure the depth of water. It is basically a stainless steel gauging rod attached to a vernier scale. This is mounted on a small square platform with 4 roller foot which allows it to be moved and rolled to different sections of the testing platform. The stainless steel gauging rod is held with a screw-like

attachment which allows the gauging rod to slide up and down over the water surface. This also allows for fine adjustments for accurate reading and can be released for large rapid changes in positions (Sabtu, 2012).

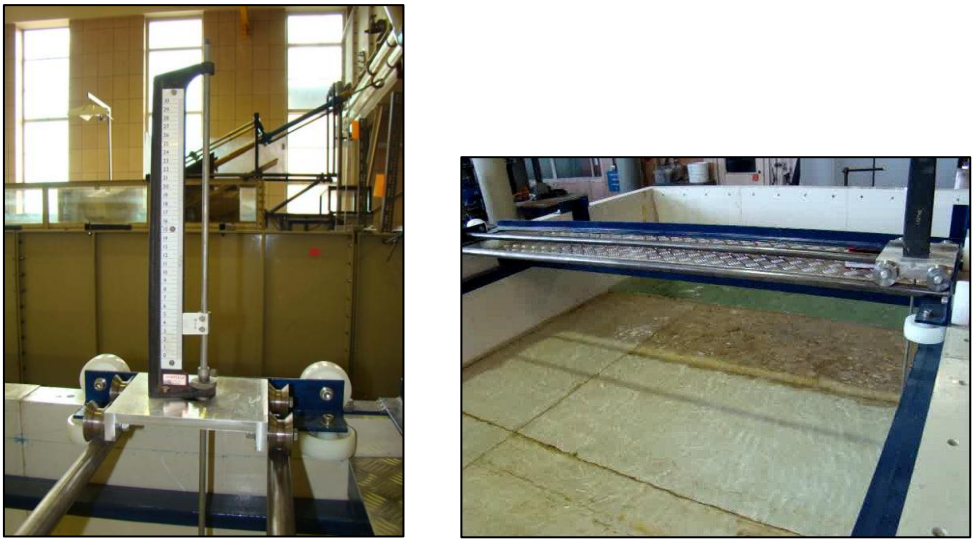

Figure 3.6 – Point-gauge equipment

Three different set ups have been tested during the study: terminal system, intermediate system and surcharged system.

3.2 Terminal system

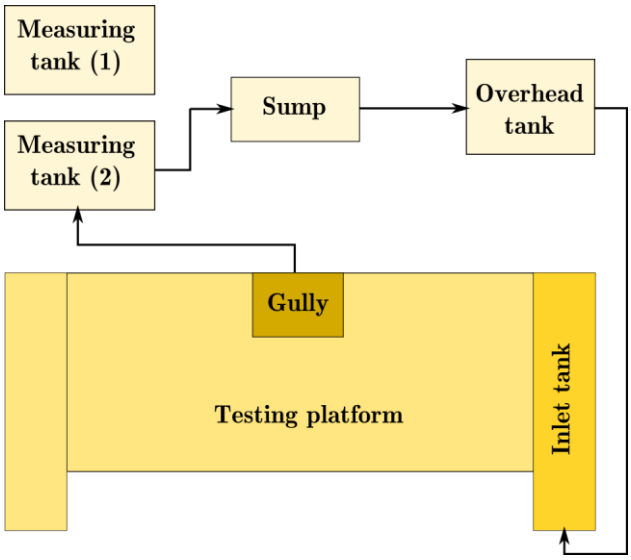

Figure 3.7 – Schematic of terminal system

The terminal gully is a special gully which can have no carryover. Therefore this type of system has only one outlet, which is through the gully

The flow from the overhead tank is transferred into the inlet tank and then towards the gully pot. Some of the flow is intercepted by the gully which then leaves the gully pot via a 150mm diameter outlet pipe into a measuring tank (2). There is no outflow from the outflow tank therefore it is working as a storage tank. Figure 3.7 shows a schematic of the terminal system.

3.3 Intermediate system

The intermediate gully system permits a portion of the approaching flow to pass the gully and flow into the next downstream one. Therefore in this type of system, there were two consecutive outlets in use. The first is the gully system itself whereas the second is the outlet tank at the far end of the testing platform.

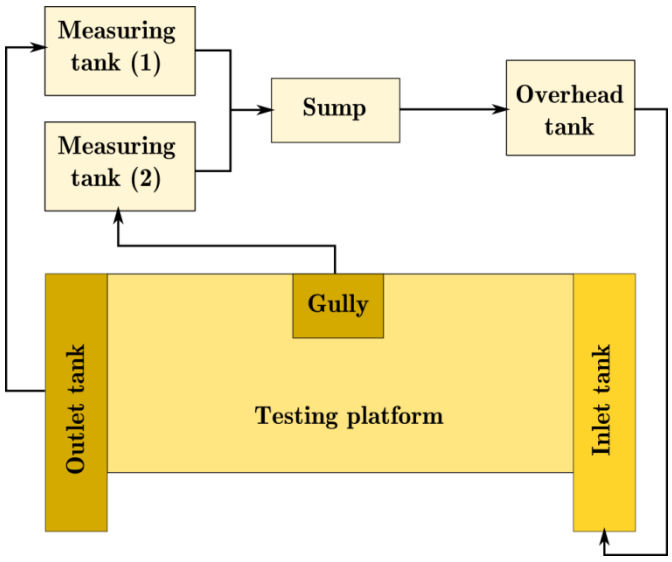

Figure 3.8 – Schematic of intermediate system

The basic of the system is the same as a terminal system where the only difference is that the bypassed flow is not passed back onto the testing platform. Instead, it is collected separately in measuring tank (1) (Sabtu, 2012). Figure 3.8 shows the schematics of the intermediate system.

3.4 Surcharged system

The surcharged condition can occur when the flows exceed the design capacity, therefore the storm sewer becomes surcharged. This type of system has two inflows. The first is the gully itself and the second one is the inlet tank. The outflow from the outlet tanks is transferred to the measuring tank, from there to the overhead tank through the sump. Figure 3.9 shows the schematic of a surcharged system.

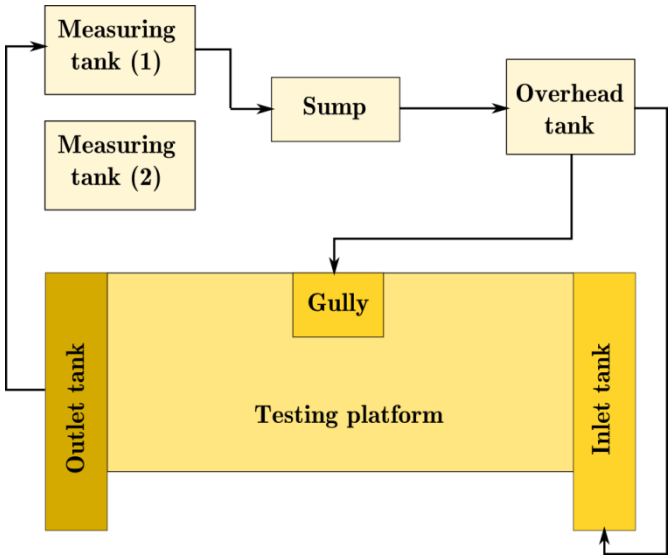

Figure 3.9 – Schematic of surcharged system

The design process traditionally relies on experimental pilot scale studies and empirical correlations. These experiments are usually expensive and time

consuming. Furthermore, the use of pilot scale studies requires the use of scaling laws to the full-size plant, which may not be well established. In addition the disruption caused by the installation of the measuring device is often intolerable.

3.5 Testing protocol

As a first step of the experimental test the transducers were installed and calibrated. After the calibration the rig was tested without grate later with grates. Terminal, intermediate and surcharge conditions were tested with 0% longitudinal and 0% cross-slopes. After the first phase of experimental tests the rig has been modified: (a) 1:30 longitudinal slop was introduced, (b) rig width has been halved. The testing protocol established the following conditions:

- Total discharge approaching to inlet – Terminal system: 15 l/s, 21 l/s, 26 l/s, 30 l/s, 33 and 36 l/s;
- Total discharge approaching to inlet – Intermediate system: 6.0 l/s, 10.5 l/s, 19.9 l/s, 23.8 l/s, 26.9 l/s, 29.6 l/s, 33 l/s;
- Surcharging discharge: 1 l/s, 3 l/s, 5 l/s, 10 l/s and 14 l/s;
- Longitudinal slope: flat and 1:100;
- Cross-slope: flat and 1:30;
- Gratings: without grate, Waterflow “S” and Waterflow “R”;
- Other condition: with rodding eye and without rodding eye.

Chapter 4

CFD Modelling

Free surface flows appear nowadays in many engineering and mathematical problem. In the last few years many numerical methods have been developed for the simulation of free-surface flows. A free surface is an interface between a liquid and a gas in which the gas can only apply a pressure on the liquid. Free surface flow is an especially difficult class of flows with moving boundaries. The position of the boundary is known only at the beginning of simulation, its location at later times has to be determined as part of the solution procedure. The flow of immiscible fluids can be divided into three groups based on the interfacial structures: (1) segregated flow, (2) mixed flow and (3) dispersed flow. This study deals with the segregated type flow. Three different free surface computation methodologies can be distinguished in modelling of segregated flow, each of which treats the interfacial jump in a different way (Ferziger & Peric, 1996), (Ubbink, 1997):

1) **Interface tracking methods**: interface is represented and tracked explicitly either by marking it with special marker points, or by attaching it to a mesh surface which is forced to move with the interface.

a) ***Mesh based tracking***:

i) *Moving mesh method*: directly align the phase interface with the edges of computation mesh cells, which then distracts as the interface evolves;

ii) *Front tracking method*: the interface is represented by an additional two dimensional mesh being superimposed on a fixed three dimensional mesh;

b) ***Marker based tracking***: the interface is tracked by directly marking it using massless marker particles;

2) **Interface capturing methods**: either side of the interface are marked with massless particles or an indicator function. This class can be divided into two sub-classes:

a) ***Marker based capturing***: the interface is captured by marker particles attached to one of the phases in order to gather information about interfacial morphology from their distribution in the phase volume;

b) ***Indicator based capturing***: a scalar indicator function is used to distinguish between two different fluids. The indicator function can be either a scalar step function representing the volume fraction of the space occupied by one of the fluids (Volume of Fluid) or a smooth function (Level Set) encompassing a pre-specified iso-surface which identifies the interface. Two main approaches can be distinguished in indicator based capturing:

i) *Single fluid (mixture) approach*: the two phases treated as a mixture having one velocity and pressure. Material properties like viscosities and densities are taken into account as mixture quantities. This approach enforces particular properties within the phase, while fostering a smooth transition across the interface.

ii) *Two fluid approach*: opposite to single fluid approach the two phases are treated separately, both having its own velocity and pressure field. A field belong to one of the phases is consistently transferred to a fictitious field using the indicator parameter.

3) **Hybrid methods**: apply elements from both interface capturing and interface tracking methods. Many combination of above mentioned approaches have been developed in last decade with the aim of improving deficiencies of the phase modelling approach.

4.1 Interface capturing methods

The interface capturing methods use an Eulerian mesh, which is fixed in space. In contrast to interface tracking these approaches do not define the interface as a sharp boundary as the exact position of the interface is not known explicitly; therefore special techniques need to be applied to capture the interface. This is commonly achieved with the following methods (Figure 4.1):

- Marker and Cell method
- Level Set function
- Volume of Fluid method

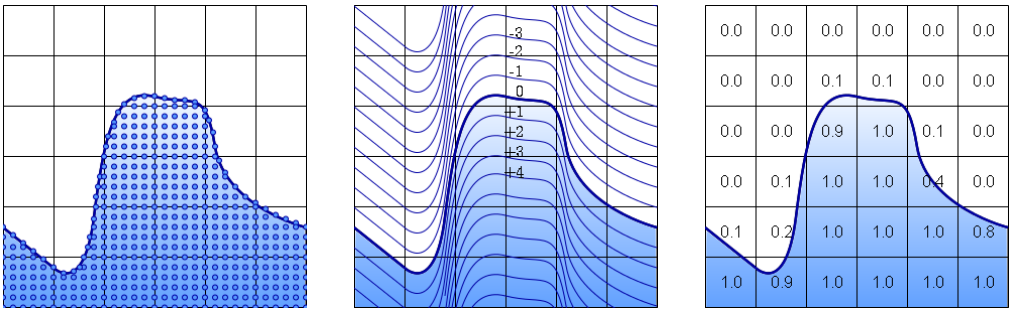

(a) Marker and Cell (b) Level Set (c) Volume of Fluid

Figure 4.1 – Interface capturing methods

The Marker and Cell (MAC) method tracks the location of the fluid within a fixed Eulerian mesh through the use of massless marker particles (Figure 4.1a). These particles are convected through the computational domain at the end of each time step using the interpolated local fluid velocity. The free surface is then constructed from the cells partially filled with marker particles and having neighbouring empty cells. In the MAC method, the normal stress boundary condition at the interface is simplified to

$$p_l = p_g \tag{4.1}$$

where subscript l and g refer to liquid and gas phases. This simplified boundary condition is applied to the cell centres rather than the actual interface location. This greatly reduces the accuracy of the computational method.

The Level Set method was proposed by Osher and Sethian (Osher & Sethian, 1988).

A continuous function is initialized throughout the computational domain as signed distance from the interface. The function is positive in one phase and negative in the other. The zero level represents the free surface (Figure 4.1b). The movement of the interface is calculated by solving the transport equation for the level set function:

$$\frac{\partial \phi}{\partial t} + \boldsymbol{v} \cdot \nabla \phi = 0 \tag{4.2}$$

This equation is derived from the assumption that each particle of liquid moves with the liquid velocity along the characteristic curves. In the Level Set approach (4.2) is transformed by setting $\boldsymbol{v}_N = \boldsymbol{v} \frac{\nabla \phi}{\|\nabla \phi\|}$ to obtain a Hamilton-Jacobi equation:

$$\frac{\partial \phi}{\partial t} + \boldsymbol{v}_N \|\nabla \phi\| = 0 \tag{4.3}$$

where $\boldsymbol{v}_N$ is the normal velocity along the gradient ϕ. Many numerical algorithms have been developed to solve (4.3). The most used algorithms are the ENO (Essentially Non-Oscillatory) and WENO (Weighted Essentially Non-Oscillatory) introduced by Osher and Sethian (Osher & Sethian, 1988) and modified by Jiang (Jiang & Peng, 2000) and Croce (Croce, et al., 2004).
The well known drawbacks of the Level Set approach are the degeneration of ϕ and that the method is not mass conservative. Therefore it requires a re-initialization procedure in every time step to keep the accuracy of approximation of the interface.

The MAC method has evolved into the Volume of Fluid (VOF) method which can be looked upon as the limit when the number of marker particle becomes infinite. The original VOF method was proposed by Hirt and Nichols (Hirt & Nichols, 1981) and represents a compressive scheme with the donor-acceptor technique for the approximation of fluxes to be advected through cell faces and it reconstructs the interface as a piecewise constant line segments aligned with the mesh. The VOF belongs to the Eulerian methods and is based on a scalar indicator function. The value of the indicator function is equal to one if the cell is full with fluid, while a zero value would indicate that the cell contained no fluid (Figure 4.1c). The cells with values between one and zero must contain the free surface.

Volume of Fluid method is perhaps the most widely used method for free surface flows despite the difficulties which have to be overcome, namely: how to advect the interface without diffusing, dispersing or wrinkling it (Ubbink & Issa, 1999). The computation of curvature is difficult, because it involves the derivitives at the interface of the non-smooth function. The advection of the characteristic function introduces numerical diffusion which is results in a significant loss of accuracy around the interface (Figure 4.2).

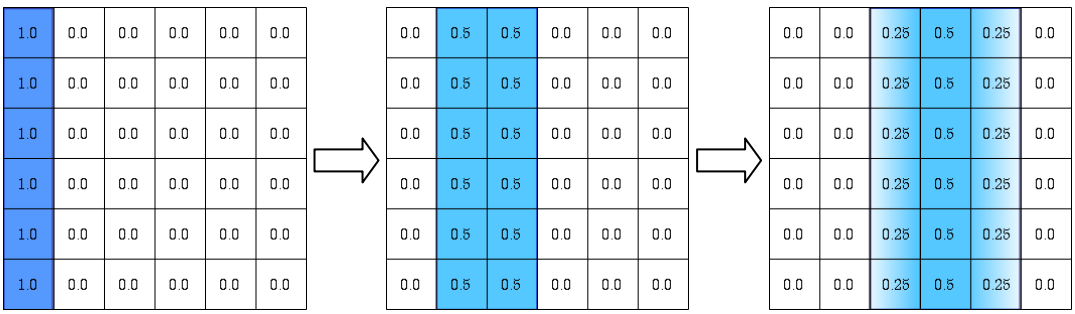

Figure 4.2 – Numerical diffusion of volume fraction in VOF

Numerous techniques have been investigated to reduce the numerical diffusion. One of the most common is the Simple Line Interface Calculation (SLIC) proposed by Noh and Woodward (Noh & Woodward, 1976). This technique approximates the interface in each cell as a line parallel with one of the coordinate axes. The direction and position of the line are deduced from the values of the volume fraction of liquid in the cell and certain neighbourhood of the cell considered. Another commonly used technique is the Piecewise Linear Interface Calculation (PLIC). This geometric algorithm has been developed to increase order of the convergence of SLIC for interface reconstruction. In this technique all the line directions are allowed for a line in one cell to construct the interface. Similarly to SLIC, the volume fraction of liquid in the cell in and its neighbourhood are taken into account. Both of these techniques do not reconstruct the interface as a series of connected line segments but rather a discontinuous chain of segments. This can lead to isolated, separated fluid bodies or disconnected free surfaces.

Several reconstruction methods have been developed to eliminate the drawbacks of the above mentioned algorithms. The direction-split algorithm, developed by Rudman (Rudman, 1997), is based on the flux corrected transport method without explicit interface reconstruction. The idea is to determine intermediate values for the phase fraction by using diffusive low order schemes and correct them by applying high order anti-diffusive fluxes. Scardovelli (Scardovelli & Zaleski, 2003) used a quadratic least-square fit to approximate the interface. Later this method was improved by Aulisa (Aulisa, et al., 2003). Renardy

(Renardy & Renardy, 2002) proposed a method where the interface is reconstructed locally with a smooth parabolic function, the result of least-square minimization. This method gives very good results in case of spurious currents which are introduced by numerical algorithms.

The Volume of Fluid method is more economical than MAC as only one value is needed for each cell. Another advantage of VOF is that only a scalar convective equation needs to be solved to propagate the volume fraction through the computational domain. Normal differencing schemes applied to the volume fraction convection equation introduce too much numerical diffusion and smear the interface over several cells. To avoid this effect special care needs to be taken to minimise the numerical diffusion.

Several improvements have been introduced in the VOF method due to its popularity. Rider and Kothe (Rider & Kothe, 1998) developed a PLIC (piecewise linear interface calculation) method and a multidimensional unsplit time integration scheme. Harvie and Fletcher (Harvie & Fletcher, 2000) introduced a new VOF advection algorithm that uses a PLIC method coupled to a fully multidimensional cell face flux integration technique. Lopez proposed an improved VOF method based on multidimensional advection using edge-matched flux polygons and spline-based interface reconstruction. Numerous hybrid methods that combine the characteristics of VOF, Level Set and front tracking methods have been proposed by researchers (Aulisa, et al., 2003), (Enright, et al., 2002) (Sussman & Pucket, 2000). In the last few years, there

have been successful attempts to simplify VOF procedures by introducing smooth basis functions (Pan & Chang, 2000), (Xiao, et al., 2005), (Yoloi, 2007). These better represent the discontinuity on the mesh but do not require geometric reconstruction.

4.2 Mathematical model

The fluid flow is mathematically described by three conservation laws, namely: (1) the conservation of mass, (2) conservation of momentum and (3) conservation of energy.

4.2.1 Navier-Stokes equations

The equations describing fluid flows were derived independently by Claude-Luis Navier and George Gabriel Stokes. The equations are an extension of the Euler equations and include the effect of viscosity. These equations describe how the velocity, pressure, temperature and density of moving fluid are related:

1. Continuity equation:

$$\frac{\partial \rho}{\partial t} + \nabla \cdot (\rho \boldsymbol{u}) = 0 \tag{4.4}$$

2. Momentum equation:

$$\frac{\partial \rho \boldsymbol{u}}{\partial t} + \nabla \cdot \left(\rho \boldsymbol{u}\boldsymbol{u}\right) = \rho g - \nabla\left(P + \frac{2}{3}\mu \nabla \cdot \boldsymbol{u}\right) + \nabla \cdot \left[\mu\left(\nabla \boldsymbol{u} + \left(\nabla \boldsymbol{u}\right)^{T}\right)\right] \tag{4.5}$$

3. Energy equation:

$$\frac{\partial \rho e}{\partial t} + \nabla \cdot (\rho e \boldsymbol{u}) = \rho g \cdot \boldsymbol{u} + \nabla \cdot (P\boldsymbol{u}) - \nabla \cdot \left(\frac{2}{3} \mu \left(\nabla \cdot \boldsymbol{u} \right) \boldsymbol{u} \right) + \nabla \cdot \left[\mu \left(\nabla \boldsymbol{u} + \left(\nabla \boldsymbol{u} \right)^T \right) \cdot \boldsymbol{u} \right] + \nabla \cdot \left(\lambda \nabla T \right) + \rho Q \tag{4.6}$$

The transport equations for internal and kinetic energy have the following form (Aris, 1989):

$$\frac{\partial \rho u}{\partial t} + \nabla \cdot \left(\rho u \boldsymbol{u} \right) = \nabla \boldsymbol{u} : \left[\mu \left(\nabla \boldsymbol{u} + \left(\nabla \boldsymbol{u} \right)^T \right) - \left(\frac{2}{3} \mu \nabla \cdot \boldsymbol{u} \right) I \right] - P \nabla \cdot \boldsymbol{u} + \nabla \cdot \left(\lambda \nabla T \right) + \rho Q \tag{4.7}$$

$$\begin{aligned} \frac{\partial \rho e_M}{\partial t} + \nabla \cdot \left(\rho e_M \boldsymbol{u} \right) &= \rho g \cdot \boldsymbol{u} - \nabla \cdot \left(P\boldsymbol{u} \right) + P \nabla \cdot \boldsymbol{u} \\ -\nabla \cdot \left(\frac{2}{3} \mu \left(\nabla \cdot \boldsymbol{u} \right) \boldsymbol{u} \right) &+ \nabla \cdot \left[\mu \left(\nabla \boldsymbol{u} + \left(\nabla \boldsymbol{u} \right)^T \right) \cdot \boldsymbol{u} \right] \\ - \nabla \boldsymbol{u} : \left[\mu \left(\nabla \boldsymbol{u} + \left(\nabla \boldsymbol{u} \right)^T \right) - \left(\frac{2}{3} \mu \nabla \cdot \boldsymbol{u} \right) I \right] & \end{aligned} \tag{4.8}$$

For incompressible isothermal fluid (ρ = constant, $\lambda = \infty$) the system can be simplified:

$$\nabla \cdot \boldsymbol{u} = 0 \tag{4.9}$$

$$\frac{\partial \boldsymbol{u}}{\partial t} + \nabla \cdot \left(\boldsymbol{u}\boldsymbol{u} \right) = g - \nabla p + \nabla \cdot \left(\nu \nabla \boldsymbol{u} \right) \tag{4.10}$$

where ν is the kinematic viscosity and p kinematic pressure (P/ρ). Most dependent variables require a gradient-diffusion term of the following form (Pantakar, 1980):

$$-\nabla \left(\Gamma_\phi \nabla \phi \right) \tag{4.11}$$

This term will be included into the transport equation for a general tensorial property χ:

$$\frac{\partial \rho \chi}{\partial t} + \nabla \cdot \left(\rho \chi \boldsymbol{u} \right) - \nabla \cdot \left(\rho \Gamma_\chi \nabla \chi \right) = S_\chi \left(\chi \right) \tag{4.12}$$

4.2.2 Turbulence modelling

Turbulence is one of the most challenging problems in fluid dynamics.
The distinction between laminar, transitional and turbulent flow is not unambiguous. Sometimes the flow appears in different states depending on the location of the area of interest. The simplest way around this problem is to calculate the flow as turbulent. The turbulent nature of the flow plays a crucial part in the determination of relevant engineering parameters.
The most straightforward approach to the solution of turbulence is Direct Numerical Simulation (DNS), which directly solves the Navier-Stokes equations. Despite the performance of modern supercomputers a direct simulation of turbulence by the time-dependent Navier-Stokes equation is applicable only to relatively simple flow problems. To calculate the flow in other more realistic cases, the complexity of the problem has to be reduced. This reduction is carried out by applying an averaging operation to the Navier-Stokes equations. The classical averaging method is the ensemble average, which produces the Reynolds Averaged Navier-Stokes equations (RANS).

The most commonly used turbulence model in environmental CFD is the standard k-ε model, since it has proven to be quite stable and often produces reasonably realistic results. Many researchers have shown that the standard k-ε turbulence model often produces a high turbulent viscosity and is not able to capture the proper behaviour of turbulent boundary layers up to separation

(Bates, et al., 2005) (ERCOFTAC, 2000). The weaknesses of the standard k-ε model can be summarized as follows:

- Laminar and transitional regimes of flow cannot be modelled with the standard k-ε model;
- Regions of recirculation in a swirling flow are under-estimated;
- The turbulent kinetic energy is over-predicted in regions of flow impingement and reattachment leading to poor prediction of the development of flow around leading edges;
- Flow separation from surfaces under the action of adverse pressure gradients is poorly predicted;
- Flow recovery following re-attachment is poorly predicted;
- Turbulence driven secondary flows in straight ducts of non-circular cross section are not predicted at all.

Finally, considering the pros and cons of different methods, the k-ω turbulence model was chosen for the turbulence modelling. This solves one equation for turbulent kinetic energy and a second equation for the specific turbulent dissipation rate (or turbulent frequency). The disadvantage of k-ω model is that it requires fine mesh resolution near the wall. The advantages of k-ω turbulence model are that it:

- Allows for a more accurate near wall treatment;
- Demonstrates superior performance for wall-bounded and low Reynolds number flows;
- Shows potential for predicting transition;

- Performs significantly better under adverse pressure gradient;
- Does not employ damping functions which leads to significant advantages in numerical stability.

To include the best features of above mentioned models Menter (Menter, 1992) has combined different elements of the k-ε and k-ω models to form a new two-equation turbulence model. Two versions of Menter's model are referred as baseline (BSL) and shear-stress transport (SST) model.

The k-ω SST model features an automatic wall treatment and uses a k-ω type model within the boundary layer and a k-ε type model in the free stream flow. The zonal formulation is based on the blending functions, which automatically ensure the proper selection of k-ω and k-ε zones.

$$\frac{\partial(\rho k)}{\partial t}+\frac{\partial(\rho u_i k)}{\partial x_i}=G_k-\beta^*\rho k\omega+\frac{\partial}{\partial x_i}\left[\left(\mu+\sigma_k\mu_t\right)\frac{\partial k}{\partial x_i}\right] \tag{4.13}$$

$$\begin{aligned}\frac{\partial(\rho\omega)}{\partial t}+\frac{\partial(\rho u_i\omega)}{\partial x_i}=\alpha\rho S^2-\beta\rho\omega^2+\frac{\partial}{\partial x_i}\left[\left(\mu+\sigma_\omega\mu_t\right)\frac{\partial\omega}{\partial x_i}\right]\\ +2(1-F_1)\rho\sigma_{\omega2}\frac{1}{\omega}\frac{\partial k}{\partial x_i}\frac{\partial\omega}{\partial x_i}\end{aligned} \tag{4.14}$$

The role of production limiter (G_k) is to prevent turbulence in stagnation regions:

$$P_k=\mu_t\frac{\partial u_i}{\partial x_j}\left(\frac{\partial u_i}{\partial x_j}+\frac{\partial u_j}{\partial x_i}\right)\quad\rightarrow\quad G_k=\min(P_k,10\beta^*\rho k\omega) \tag{4.15}$$

F_1 is the blending function and defined by:

$$F_1=\tanh\left\{\left\{\min\left[\max\left(\frac{\sqrt{k}}{\beta^*\omega y},\frac{500\nu}{y^2\omega}\right),\frac{4\rho\sigma_{\omega2}k}{CD_{k\omega}y^2}\right]\right\}^4\right\} \tag{4.16}$$

The value of F_1 is between one and zero. In case of one (inside the boundary layer) the k-ω model is in use, while if it is equal to zero the k-ε model used. $CD_{k\omega}$ is defined as:

$$CD_{k\omega} = \max\left(2\rho\sigma_{\omega 2}\frac{1}{\omega}\frac{\partial k}{\partial x_i}\frac{\partial \omega}{\partial x_i}, 10^{-10}\right) \tag{4.17}$$

The turbulent eddy viscosity is defined as:

$$\nu_t = \frac{a_1 k}{\max(a_1\omega, SF_2)} \tag{4.18}$$

where S is the invariant measure of strain rate and F_2 defined by:

$$F_2 = \tanh\left[\left[\max\left(\frac{2\sqrt{k}}{\beta^*\omega y}, \frac{500\nu}{y^2\omega}\right)\right]^2\right] \tag{4.19}$$

The k-ω SST model is a mixture of k-ε and k-ω models; therefore all the constants are computed by a blend form: $\alpha = \alpha_1 F + \alpha_2(1-F)$

4.2.3 Final form of equations

The equations of motion are closed with the constitutive relation for density and dynamic viscosity. If the system consist two fluids then this yields:

$$\rho = \gamma\rho_1 + (1-\gamma)\rho_2 \tag{4.20}$$

$$\mu = \gamma\mu_1 + (1-\gamma)\mu_2 \tag{4.21}$$

where γ is an indicator function and defined as:

$$\gamma(x,t) = \begin{cases} 1 \text{ for the point } (x,t) \text{ inside fluid 1} \\ 0 \text{ for the point } (x,t) \text{ inside fluid 2} \end{cases} \tag{4.22}$$

In order to model two fluids as a continuum the density should be continuous and differentiable (Brackbill, et al., 1992), (Lafaurie, et al., 1994). It can be

achieved with transitional area between the two fluids, which has a very small finite thickness:

$$\gamma(\boldsymbol{x},t)=\begin{cases} 1 & \text{for the point } (\boldsymbol{x},\text{t}) \text{ inside fluid 1} \\ 0 & \text{for the point } (\boldsymbol{x},\text{t}) \text{ inside fluid 2} \\ 0<\gamma_0<1 & \text{for the point } (\boldsymbol{x},\text{t}) \text{ inside the transitional area} \end{cases} \tag{4.23}$$

Since the value of γ is associated with both fluids, it propagates with the fluids as a Lagrangian invariant and has a zero material derivative (Hirt & Nichols, 1981):

$$\frac{\partial\gamma}{\partial t}+\boldsymbol{u}\cdot\nabla\gamma=0 \tag{4.24}$$

The equations derived above completely describe the motion of two fluids; however analytical solutions are only available for simple circumstances. Due to the discontinuity of ρu at the interface the above equations need to be reformulated for numerical solution. This reformulation can be accomplished as Spalding (Spalding, 1974) suggested:

$$\begin{aligned} &\frac{\partial\boldsymbol{\rho}}{\partial t}+\boldsymbol{u}\cdot\nabla\boldsymbol{\rho}+\boldsymbol{\rho}\nabla\cdot\boldsymbol{u}=0 \\ &\Rightarrow\nabla\cdot\boldsymbol{u}=-\frac{1}{\boldsymbol{\rho}}\left(\frac{\partial\boldsymbol{\rho}}{\partial t}+\boldsymbol{u}\cdot\nabla\boldsymbol{\rho}\right)=-\frac{1}{\rho}\frac{D\boldsymbol{\rho}}{Dt}=-\frac{D(\ln\boldsymbol{\rho})}{Dt} \end{aligned} \tag{4.25}$$

In order to simplify the simulation, in this study both fluid (air and water) were assumed as incompressible. This is a reasonable assumption for the operation conditions of atmospheric pressure and for a non-temperature dependent problem. This assumption simplifies the equation(4.25), because the right hand side becomes equal to zero.

$$\nabla\cdot\boldsymbol{u}=-\frac{1}{\boldsymbol{\rho}}\frac{D}{Dt}\left(\gamma(\boldsymbol{\rho}_1-\boldsymbol{\rho}_2)+\boldsymbol{\rho}_2\right)=\frac{-(\boldsymbol{\rho}_1-\boldsymbol{\rho}_2)}{\boldsymbol{\rho}}\left(\frac{D\gamma}{Dt}\right)=0 \tag{4.26}$$

It is better to rearrange the transport equation for finite volume discretization using the identity $\nabla \cdot \gamma \boldsymbol{u} = \gamma \nabla \cdot \boldsymbol{u} + \boldsymbol{u} \cdot \nabla \gamma$ and the incompressibility condition:

$$\frac{\partial \gamma}{\partial t} + \nabla \cdot \gamma \boldsymbol{u} = 0 \tag{4.27}$$

The momentum equation can also be simplified using the incompressibility condition:

$$\frac{\partial \boldsymbol{\rho u}}{t} + \nabla \cdot \left(\boldsymbol{\rho u} \cdot \boldsymbol{u} \right) - \nabla \cdot \left(\mu \nabla \cdot \boldsymbol{u} \right) = -\nabla P + \boldsymbol{\rho} g + f_{\sigma} + \left(\nabla \cdot \boldsymbol{u} \right) \cdot \left(\nabla \mu \right) \tag{4.28}$$

where f_{σ} is the surface tension source term.

The final form continuity equation for incompressible flow, momentum equation and α transport equation need to be solved simultaneously together with the constitutive relations for density and dynamic viscosity.

4.2.4 Initial and boundary conditions

Regardless of the numerical methodology chosen to solve the governing equations, suitable initial and boundary conditions have to be specified. The initial conditions determine the state of fluid at time t=0, or at first step of an iterative scheme.

Since the governing equations are a mixture of elliptic, parabolic and hyperbolic behaviour, boundary conditions must be specified at each point of the closed solution domain. Boundary conditions (BC) can be divided into two types:

- **Dirichlet** BCs prescribe the value of the dependent variable on the boundary and are therefore termed “fixed value”;
- **von Neumann** BCs prescribe the gradient of the variable normal to the boundary and are therefore termed “fixed gradient”

The most common physical boundary conditions in the discretised equation of the finite volume are (Versteeg & Malalasekera, 2007):

Inlet boundary: The most common method is to fix the inlet velocity. Another option is to specify the upstream stagnation pressure and velocity magnitude. For this study, just like all multiphase flow modelling, this implies that the inlet condition of the indicator function needs to be fixed.

Outlet boundary: It is vital that the outlet boundary condition is always selected on the basis it has a weak influence on the upstream flow. It should be placed as far away as possible from the region of interest and should be avoided in regions of strong geometrical changes. The most common physical condition for internal flows is to fix the downstream static pressure and zero gradient condition is applied to the velocities. Another commonly used approach is when the first row of cells next to the boundary is used to construct the velocity distribution. The boundary velocities are then scaled according to this velocity profile. If the boundary is placed where variation in the flow is small, then a zero gradient condition to the indicator function can be applied.

Solid wall boundary: The normal velocity is zero; therefore no mass or other convective flux can penetrate the solid body. The other variables at the wall, the tangential velocity and pressure have to be determined by extrapolation from the interior boundary.

Symmetry plane boundary: The surface normal gradients of all scalar fields are zero at the symmetry plane, thus the convection flux through the symmetry is

zero as well. Viscous stress of velocity component parallel to the boundary is zero.

The correct implementation of boundary condition is crucial point of every flow solver. The accuracy of the solution is strongly depends on a proper physical and numerical treatment of boundaries (Blazek, 2001). Furthermore the robustness and convergence speed are considerably influenced.

4.3 Numerical Model

4.3.1 Introduction

This Section describes the procedure by which the equations presented in Section 4.1 are solved numerically. The discretization used in the present study is the well established finite volume method (Versteeg & Malalasekera, 2007), (Blazek, 2001), (Hirsch, 2007). Finite volume method became popular in CFD as a result of two advantages:

1. it ensures that the discretization is conservative (mass, momentum and energy are conserved in a discrete sense);
2. it does not require coordinate transformation in order to be applied on irregular meshes.

While the first property usually can be obtained using the finite difference formulation, it is obtained naturally from the finite volume method. The second property means that the finite volume method can be applied on unstructured mesh consisting of arbitrary polyhedral. This increased flexibility is a great advantage in generating a mesh for arbitrary geometries.

The finite volume method subdivides the flow domain into small control volumes. The transport equations are integrated over the control volumes by approximating the variation of flow properties between mesh points with piecewise profiles. These piecewise approximations – or differencing schemes – are constructed to support physical flow behaviour such as convection or diffusion.

The solution procedure can be divided into three parts:

1. Discretization of solution domain into control volumes;
2. Numerical solution procedure;
3. Post processing where the results of the simulation are checked and contour, vector plots prepared.

4.3.2 Full 3D model

4.3.2.1 Spatial discretization

The main advantage of the finite volume method is that the spatial discretization is carried out directly in the physical space. In other words, there are no problems with any transformation between coordinate systems, as in the case of finite difference method (Blazek, 2001). There are several possibilities of defining the shape and position of the control volume. Two basic approaches can be distinguished: cell-centred scheme and cell-vertex scheme. The cell-centred scheme, when the flow quantities are stored at the centroids of the control volumes. In case of cell-vertex scheme the flow variables are stored at the mesh points. The approach used in this study the so called co-located variable arrangement (Peric, 1985) where all the flow properties are defined at

the centre of the control volume. The general notation used by Jasak (Jasak, 1996) and Ubbink (Ubbink, 1997) is also used in this study.

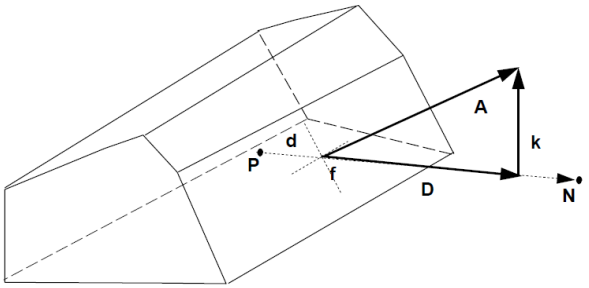

Figure 4.3 – Control volume

Figure 4.3 represents a typical control volume with an arbitrary number of faces. The computational point P is at the centre of the control volume. The vector $\boldsymbol{d} = \underline{PN}$ connects the computational point P with its neighbour N and $\boldsymbol{A}$ is the outward-pointing face area vector normal to the face. The mesh is defined as being non-orthogonal if the angle between the vectors $\boldsymbol{A}$ and $\boldsymbol{d}$ is not zero. The vectors $\boldsymbol{D}$ and $\boldsymbol{k}$ are then introduced to account for the orthogonal; and non-orthogonal contributions to the gradients at cell faces respectively. Jasak (Jasak, 1996) describes three different approaches for splitting of the non-orthogonal contribution $\boldsymbol{k}$ from the orthogonal component $\boldsymbol{D}$. The so called over relaxed approach has shown to be the superior of the three approaches and will be used in this study for the discretization of momentum and pressure equations. The vectors $\boldsymbol{D}$ and $\boldsymbol{k}$ are defined as:

$$\boldsymbol{D} = \frac{\boldsymbol{d}}{\boldsymbol{d} \cdot \boldsymbol{A}} \left| \boldsymbol{A} \right|^2 \tag{4.29}$$

$$\boldsymbol{k} = \boldsymbol{A} - \boldsymbol{D} \tag{4.30}$$

4.3.2.2 *Discretization of the governing equations*

Once the solution domain has been defined, the governing equations are discretized by integrating them over all cells and applying Gauss' theorem which translates a volume integral to a surface integral (Peric, 1985). The values of primitive variables on the cell faces are then rewritten in terms of neighbouring cell centre values yielding an algebraic equation for that cell. The result is a set of linear algebraic equation written in terms of mesh cell centre values (Hill, 1998).

The standard form of the transport equation for a scalar property ϕ is:

$$\underbrace{\frac{\partial \rho \boldsymbol{\phi}}{\partial t}}_{\text{temporal derivative}} + \underbrace{\nabla \cdot (\rho \boldsymbol{u} \boldsymbol{\phi})}_{\text{convection term}} - \underbrace{\nabla \cdot (\rho \Gamma_{\phi} \nabla \boldsymbol{\phi})}_{\text{diffusion term}} = \underbrace{S_{\phi}(\boldsymbol{\phi})}_{\text{source term}} \tag{4.31}$$

where ρ is the density, $\boldsymbol{u}$ is the velocity and Γ_{ϕ} is the diffusion coefficient. This is a second order equation, as the diffusion term includes the second derivative of ϕ in space. The finite volume method requires that equation (4.31) is satisfied over the control volume V_P around the point P in the integral form:

$$\begin{aligned} \int_t^{t+\Delta t} \left[\frac{\partial}{\partial t} \int_{V_P} \rho \boldsymbol{\phi} dV + \int_{V_P} \nabla \cdot (\rho \boldsymbol{u} \boldsymbol{\phi}) dV - \int_{V_P} \nabla \cdot (\rho \Gamma_{\phi} \nabla \boldsymbol{\phi}) dV \right] dt \\ = \int_t^{t+\Delta t} \left(\int_{V_P} S_{\phi}(\boldsymbol{\phi}) dV \right) dt \end{aligned} \tag{4.32}$$

The generalized form of Gauss' theorem is used throughout the discretization procedure and defined below for various spatial derivatives of a vector or scalar quantity ϕ:

$$\int_V \nabla \cdot \boldsymbol{\phi} dV = \oint_{\partial V} dS \cdot \boldsymbol{\phi} \tag{4.33}$$

$$\int_V \nabla \boldsymbol{\phi} dV = \oint_{\partial V} dS \boldsymbol{\phi} \tag{4.34}$$

$$\int_V \nabla \otimes \boldsymbol{\phi} dV = \oint_{\partial V} dS \otimes \boldsymbol{\phi} \tag{4.35}$$

where ϕ is an arbitrary scalar function, $\boldsymbol{\phi}$ an arbitrary vector function, dS the surface area vector and ∂V the surface area of the control volume.

Since the control volume is bounded by flat faces the (4.33) can be transformed into sum of integrals over all faces:

$$\begin{aligned}\int_{V_P} \nabla \cdot \boldsymbol{\phi} dV = \oint_{\partial V_P} dS \cdot \boldsymbol{\phi} &= \sum_{f=1}^{n} \left(\int_f dS \boldsymbol{\phi} \right) \\ &\approx \sum_{f=1}^{n} A_f \cdot \boldsymbol{\phi}_f\end{aligned} \tag{4.36}$$

where f is the centre of the cell face, A_f the face area vector and n is the number of faces of a control volume. Every face is shared by two neighbouring cells of which one owns the face and the other is the neighbour. The face area vector $\boldsymbol{A}_f$ always points from the owner cell into the neighbour cell of the face. Unless is stated otherwise the face values are obtained by linear interpolation:

$$\boldsymbol{\phi}_f = L_P \boldsymbol{\phi}_P + (1 - L_P) \boldsymbol{\phi}_N \tag{4.37}$$

The interpolation of a vector means the interpolation of each of its components. L_P is the interpolation factor and defined as ratio of the distances $\underline{fN}$ and $\underline{PN}$:

$$L_P = \frac{\left| \underline{fN} \right|}{\left| \underline{PN} \right|} \tag{4.38}$$

Similar relations to (4.36) can be derived for (4.34) and (4.35):

$$\int_{V_P} \nabla \boldsymbol{\phi} dV \approx \sum_{f=1}^{n} \boldsymbol{A}_f \boldsymbol{\phi}_f \tag{4.39}$$

and

$$\int_{V_P} \nabla \otimes \boldsymbol{\phi} dV \approx \sum_{f=1}^{n} \boldsymbol{A}_f \otimes \boldsymbol{\phi}_f \tag{4.40}$$

Equations (4.36), (4.39) and (4.40) can be used to get a second order accurate discretised prediction of the gradient of a flow property over a cell:

$$\left(\nabla \cdot \boldsymbol{\phi}\right)_P \approx \frac{1}{V_P}\sum_{f=1}^{n} \boldsymbol{A}_f \cdot \boldsymbol{\phi}_f \tag{4.41}$$

$$\left(\nabla \phi\right)_P \approx \frac{1}{V_P}\sum_{f=1}^{n} A_f \phi_f \tag{4.42}$$

$$\left(\nabla \otimes \boldsymbol{\phi}\right)_P \approx \frac{1}{V_P}\sum_{f=1}^{n} A_f \otimes \boldsymbol{\phi}_f \tag{4.43}$$

These equations will be used in the derivation of the discretized transport equations given in the following sections.

4.3.2.3 Momentum equation

The finite volume discretization is based on the integral form of (4.28) over the control volume and the time step Δt:

$$\begin{aligned}\int_t^{t+\Delta t}\left(\int_V \frac{\partial \boldsymbol{\rho u}}{\partial t} dV\right) dt + \int_t^{t+\Delta t}\left(\int_V \nabla \cdot (\boldsymbol{\rho u} \otimes \boldsymbol{u}) dV\right) dt - \int_t^{t+\Delta t}\left(\int_V \nabla \cdot (\mu \nabla \otimes \boldsymbol{u}) dV\right) dt \\ = -\int_t^{t+\Delta t}\left(\int_V \nabla P dV\right) dt + \int_t^{t+\Delta t}\left(\int_V \boldsymbol{\rho} g dV\right) dt \\ + \int_t^{t+\Delta t}\left(\int_V \sigma \kappa \nabla \alpha dV\right) dt + \int_t^{t+\Delta t}\left(\int_V (\nabla \otimes \boldsymbol{u}) \cdot (\nabla \mu) dV\right) dt\end{aligned} \tag{4.44}$$

The discretization of the momentum equation is presented in several works (Versteeg & Malalasekera, 2007), (Peric, 1985), (Hirsch, 2007) and (Blazek, 2001), therefore the partially discretized form of momentum equation in terms of a cell and its face values will be given without further proof.

The partially discretized form of the momentum equation is:

$$\int_t^{t+\Delta t}\left(\left(\frac{\partial \boldsymbol{\rho u}}{\partial t}\right)_P V_P + \sum_{f=1}^{n} \boldsymbol{\rho}_f F_f \boldsymbol{u}_f - \sum_{f=1}^{n} \mu_f \boldsymbol{A}_f \cdot \left(\nabla \otimes \boldsymbol{u}\right)_f\right) dt = \int_t^{t+\Delta t}\left(\boldsymbol{S}_{u_P} V_P\right) dt \tag{4.45}$$

where $\boldsymbol{S}_{u_P}$ is the source term and defined as:

$$\boldsymbol{S}_{u_P} = -\left(\nabla P\right)_P + g\boldsymbol{\rho}_P + \sigma\kappa_P\left(\nabla\alpha\right)_P + \left(\nabla\otimes\boldsymbol{u}\right)_P\cdot\left(\nabla\mu\right)_P \tag{4.46}$$

The terms of interest in the above equation are the convection, diffusion and κ curvature terms. These terms are discussed in the following sections. The gradients over a cell of different flow properties can be calculated according to equations (4.42) and (4.43).

4.3.2.3.1 Convection term

The finite volume discretization of the convection term yields:

$$\begin{aligned}\int_{V_P}\nabla\cdot(\rho\boldsymbol{u}\boldsymbol{\phi})dV &= \sum_f \boldsymbol{A}_f\cdot(\rho\boldsymbol{u}\boldsymbol{\phi})_f \\ &= \sum_f \boldsymbol{A}_f\cdot(\rho\boldsymbol{u})_f\boldsymbol{\phi}_f \\ &= \sum_f \boldsymbol{F}_f\boldsymbol{\phi}_f\end{aligned} \tag{4.47}$$

where $\boldsymbol{F}_f$ is the face mass flux through the face:

$$\boldsymbol{F}_f = \boldsymbol{A}_f\cdot(\rho\boldsymbol{u})_f \tag{4.48}$$

The cell face flux is calculated by the solution algorithm. The cell face average value (ϕ_f) is determined from the cell nodal values via the differencing scheme. Jasak (Jasak, 1996) analysed a number of differencing schemes in terms of boundedness, stability, accuracy and required computational resource. Considering the advantage and disadvantage of different differencing schemes the upwind (Pantakar, 1980) and Gamma (Jasak, 1996) schemes have been chosen for this study. The Gamma scheme guaranties a bounded solution whilst minimising the numerical diffusion of sharp changes in gradient of the variable. The upwind scheme determines the value of ϕ at the cell face by considering the direction of flow is normal to the cell face. The value at the cell face is equal to the value of the cell node from the upwind direction:

$$\boldsymbol{F}_f\boldsymbol{\phi}_f = \boldsymbol{\phi}_P \max\left[\boldsymbol{F},0\right] - \boldsymbol{\phi}_N \max\left[-\boldsymbol{F},0\right] \tag{4.49}$$

where the subscript P and N indicates the current and neighbouring cell values. The Gamma scheme is a high resolution second order convection-diffusion differencing scheme based on the Normalised Variable Diagram (NVD) (Leonard, 1991), specially developed for unstructured meshes. The magnitude (u) of the velocity vector ($\boldsymbol{u}$) is defined as:

$$u_f = \begin{cases} u_D & \text{for } \tilde{u}_D < 0 \text{ or } \tilde{u}_D > 1 \\ \dfrac{1}{2}(u_D + u_A) & \text{for } k < \tilde{u}_D < 1 \\ \left(1 - \dfrac{\tilde{u}_D}{2k}\right)u_D + \dfrac{\tilde{u}_D}{2k}u_A & \text{for } 0 < \tilde{u}_D < k \end{cases} \tag{4.50}$$

where k is prescribed constant with a value between 0 and 0.5. The recommended value is 0.1. The subscripts D and A are determined by the direction of flow:

$$F_f \geq 0 \Rightarrow D = P \;\&\; A = N \text{ or } F_f < 0 \Rightarrow D = N \;\&\; A = P \tag{4.51}$$

The decision factor $\tilde{u}_D$ is defined as:

$$\tilde{u}_D = 1 - \frac{u_A - u_D}{2(\nabla u)_D \cdot \boldsymbol{d}} \tag{4.52}$$

and calculated according to (4.42):

$$(\nabla u)_D \approx \frac{1}{V_D}\sum_{f=1}^{n} \boldsymbol{A}_f u_f \tag{4.53}$$

4.3.2.3.2 Diffusion term

The diffusion term will be discretised in a similar way. Using the assumption of linear variation of ϕ :

$$\int_{V_P} \nabla \cdot (\mu \nabla \cdot \boldsymbol{u}) dV \approx \sum_{f=1}^{n} \mu_f \boldsymbol{A}_f \cdot (\nabla \cdot \boldsymbol{u})_f \tag{4.54}$$

where the dynamic viscosity at the face (μ_f) is calculated by linear interpolation with L_P calculated from (4.38):

$$\mu_f = L_P \mu_P + (1 - L_P) \mu_N \tag{4.55}$$

For an orthogonal mesh, the calculation of the gradient at the cell face is relatively straightforward using the nodal values straddling the cell face. Considering (4.29) and $\boldsymbol{A}_f = \boldsymbol{D}_f$ then it is possible for an orthogonal mesh to use the following expression for the dot product between the face area vector and the velocity gradient at the face:

$$\boldsymbol{A}_f \cdot (\nabla \cdot \boldsymbol{u})_f = \boldsymbol{D}_f \cdot (\nabla \cdot \boldsymbol{u})_f = \left| \boldsymbol{D}_f \right| \frac{\boldsymbol{u}_N - \boldsymbol{u}_P}{\left| \boldsymbol{d}_f \right|} \tag{4.56}$$

If the mesh is non-orthogonal it is necessary to introduce an additional term to compensate the non-orthogonal contribution. This is done by $\boldsymbol{A}_f = \boldsymbol{D}_f + \boldsymbol{k}_f$, the over relaxed non orthogonal decomposition of the face area vector (Jasak, 1996), (Ubbink, 1997):

$$\boldsymbol{A}_f \cdot (\nabla \cdot \boldsymbol{u})_f = \underbrace{\boldsymbol{D}_f \cdot (\nabla \cdot \boldsymbol{u})_f}_{\text{orthogonal contribution}} + \underbrace{\boldsymbol{k}_f \cdot (\nabla \cdot \boldsymbol{u})_f}_{\text{non-orthogonal correction}} \tag{4.57}$$

In this case the orthogonal correction is treated explicitly.

4.3.2.3.3 Source term

Terms of the general transport equation which cannot be treated as convective or diffusive term are included in the source term. The source term $S_\phi(\phi)$, can be a general function of ϕ. The treatment of these terms follows the work of

Pantakar (Pantakar, 1980), in which the source terms are linearized before the actual discretization:

$$S_\phi(\phi) = Su + Sp\phi \tag{4.58}$$

where Su and Sp can also depend on ϕ. Integration of (4.58) over the control volume yields:

$$\int_{V_P} S_\phi(\phi) dV = Su V_P + Sp V_P \phi_P \tag{4.59}$$

Su is directly added to any existing source term. If Sp is negative, then it can be added to the central coefficient of the solution matrix increasing its diagonal dominance and enhancing the stability of the solution (Brennan, 2001). If it is positive then it is solved explicitly.

4.3.2.4 *Temporal discretization*

Early applications of CFD were mostly focused on steady state solutions. These have a benefit of being easier to solve in terms of complexity and computer requirements. Nowadays the attention is being focused on unsteady simulation. In these cases, in addition to the question of spatial discretization, there is the question of temporal discretization.

In the previous Section we have described the discretization of the volume integrals in the standard transport equation in integral form:

$$\int_t^{t+\Delta t} \left[\frac{\partial}{\partial t} \int_{V_P} \rho\phi dV + \int_{V_P} \nabla \cdot (\rho \mathbf{u}\phi) dV - \int_{V_P} \nabla \cdot (\rho \Gamma_\phi \nabla \phi) dV \right] dt = \int_t^{t+\Delta t} \left(\int_{V_P} S_\phi(\phi) dV \right) dt \tag{4.32}$$

Assuming that the control volume does not change in time, the equation (4.32) can be written as:

$$\int_t^{t+\Delta t}\left[\left(\frac{\partial \rho\phi}{\partial t}\right)_P V_P + \sum_f F\phi_f - \sum_f (\rho\Gamma_\phi)_f \boldsymbol{A}_f (\nabla\phi)_f\right] dt = \int_t^{t+\Delta t} (Su V_P + Sp V_P \phi_P)\ dt \tag{4.60}$$

This expression is usually referred to as a "semi-discretized" form of the transport equation (Hirsch, 2007). The temporal integrals and time derivative can be calculated directly as:

$$\left(\frac{\partial \rho\phi}{\partial t}\right)_P = \frac{\rho_P^n \phi_P^n - \rho_P^o \phi_P^o}{\Delta t} \tag{4.61}$$

$$\int_t^{t+\Delta t} \phi(t)\ dt = \frac{1}{2}(\phi^o + \phi^n)\Delta t \tag{4.62}$$

where

$$\begin{aligned} \phi^n &= \phi(t+\Delta t) \\ \phi^o &= \phi(t) \end{aligned} \tag{4.63}$$

Assuming that the density and diffusivity do not change in time, equations (4.60), (4.61) and (4.62) give:

$$\begin{aligned} \frac{\rho_P \phi_P^n - \rho_P \phi_P^o}{\Delta t} V_P + \frac{1}{2}\sum_f F\phi_f^n - \frac{1}{2}\sum_f (\rho\Gamma_\phi)_f \boldsymbol{A}_f (\nabla\phi)_f^n \\ + \frac{1}{2}\sum_f F\phi_f^o - \frac{1}{2}\sum_f (\rho\Gamma_\phi)_f \boldsymbol{A}_f (\nabla\phi)_f^o \\ = Su V_P + \frac{1}{2} Sp V_P \phi_P^n + \frac{1}{2} Sp V_P \phi_P^o \end{aligned} \tag{4.64}$$

Since ϕ_f and $(\nabla\phi)_f$ also depends on values of ϕ in the surrounding cells (4.64) produces an algebraic equation:

$$a_P \phi_P^n = \sum_N a_N \phi_N^n + Su \tag{4.65}$$

where the subscript N denotes the nearest neighbours.

It is useful to present the discretised momentum equation as:

$$\boldsymbol{u}_P^n = \frac{\boldsymbol{H}(\boldsymbol{u})_P}{a_{P_P}} - \frac{1}{a_{P_P}}(\nabla P)_P \tag{4.66}$$

where $a_{P_P} = a_P$ and:

$$\boldsymbol{H}(\boldsymbol{u})_P = \sum_N a_N \boldsymbol{u}_N^n + Su_P \tag{4.67}$$

This formulation of the discretized momentum equation will be used for the derivation of the pressure equation.

4.3.2.5 Pressure equation

The pressure equation is derived from the incompressibility condition and the discretized momentum equation. The discretized continuity equation has the following form:

$$\int_V \nabla \cdot \boldsymbol{u} dV = \sum_f \boldsymbol{A}_f \cdot \boldsymbol{u}_f = 0 \tag{4.68}$$

The discretized momentum equation (4.66) is used to predict the face value of the velocity. This is done by isolating the contribution of the pressure from (4.66) when interpolating it to the face. The contribution of the pressure gradient at the face is then added explicitly to $\boldsymbol{u}_f$ by calculating it directly from the pressure values at the nodes sharing the face. The face value of velocity is:

$$\boldsymbol{u}_f = \left(\frac{\boldsymbol{H}(\boldsymbol{u})}{a_P}\right)_f - \left(\frac{1}{a_P}\right)(\nabla P)_f \tag{4.69}$$

The face values other than pressure gradient are calculated by using linear interpolation:

$$\left(\frac{\boldsymbol{H}(\boldsymbol{u})}{a_P}\right)_f = L_P\left(\frac{\boldsymbol{H}(\boldsymbol{u})}{a_P}\right)_P + (1 - L_P)\left(\frac{\boldsymbol{H}(\boldsymbol{u})}{a_P}\right)_N \tag{4.70}$$

$$\left(\frac{1}{a_P}\right)_f = L_P\left(\frac{1}{a_P}\right)_P + (1 - L_P)\left(\frac{1}{a_P}\right)_N \tag{4.71}$$

Substitution of $\boldsymbol{u}_f$ from (4.69) into (4.68) gives:

$$\sum_f \left(\frac{1}{a_P}\right)_f \boldsymbol{A}_f \cdot (\nabla P)_f = \sum_f \boldsymbol{A}_f \cdot \left(\frac{\boldsymbol{H}(\boldsymbol{u})}{a_P}\right)_f \tag{4.72}$$

Taking into account the orthogonal and non-orthogonal contribution of neighbours, the pressure gradient over the faces can be calculated similarly to diffusion term. Using the over relaxed non-orthogonal decomposition of the face area vector:

$$\boldsymbol{A}_f \cdot (\nabla P)_f = \underbrace{\boldsymbol{D}_f \cdot (\nabla P)_f}_{\text{orthogonal contribution}} + \underbrace{\boldsymbol{k}_f \cdot (\nabla P)_f}_{\text{non-orthogonal correction}} \tag{4.73}$$

The orthogonal contribution is given by:

$$\boldsymbol{D}_f \cdot (\nabla P)_f = \left|\boldsymbol{D}_f\right| \frac{P_N - P_P}{\left|\boldsymbol{d}_f\right|} \tag{4.74}$$

and the non orthogonal correction is:

$$\boldsymbol{k}_f \cdot (\nabla P)_f = \boldsymbol{k}_f \cdot \left(L_P \left(\frac{1}{V_P} \sum_f \boldsymbol{A}_f P_f \right)_f + (1 - L_P) \left(\frac{1}{V_N} \sum_f \boldsymbol{A}_f P_f \right)_N \right) \tag{4.75}$$

The non-orthogonal correction is treated explicitly by adding it to the source term:

$$\sum_f \left(\frac{1}{a_P}\right)_f \boldsymbol{D}_f \cdot (\nabla P)_f = Sp \tag{4.76}$$

where

$$Sp = \sum_f \boldsymbol{A}_f \cdot \left(\frac{\boldsymbol{H}(\boldsymbol{u})}{a_P}\right)_f - \sum_f \left(\frac{1}{a_P}\right)_f \boldsymbol{k}_f \cdot (\nabla P)_f \tag{4.77}$$

Now it is possible to reformulate the pressure equation:

$$a_P P_P = \sum_N a_N P_N + Sp \tag{4.78}$$

4.3.2.6 Solution algorithm

The fluid in this study assumed to be Newtonian and incompressible. It follows there is no explicit equation for pressure, therefore special care needs to be taken to avoid de-coupling of pressure from velocity. It can be done by deriving the discretized pressure equation from a semi-discretized momentum equation, using the continuity restriction of a divergence free velocity field. The solution procedure applied in this study is based on PISO algorithm.

4.3.2.6.1 Pressure-velocity coupling with PISO

Pressure Implicit with Splitting of Operators (PISO) algorithm is a pressure-velocity treatment for transient flow calculation proposed by Issa (Issa, 1986). PISO is a segregated approach for solving the Navier-Stokes equations, where pressure and velocity are treated sequentially using the predictor-corrector procedure. The summary of the algorithm is presented by Jasak (Jasak, 1996) and Rusche (Rusche, 2002).

The pressure-velocity coupling is applied in three main steps:

1. *Momentum predictor step*: the pressure is used to solve the momentum equation and obtain the first approximation of velocity. The first approximation of velocity is not satisfies the continuity restriction.
2. *Pressure solution step*: the matrix of pressure equation is assembled and solved to get the new estimation for the pressure.
3. *Explicit velocity correction step*: the pressure obtained in previous step is used to calculate the conservative volumetric fluxes and reconstruct the velocities which are consistent with the pressure field.

The velocity depends on the pressure field and the contribution from the updated velocities of neighbouring cells. Therefore the last two steps are repeated until the predefined tolerance condition is satisfied. When the PISO loop is finished the velocity is corrected with the correct pressure gradient.

4.3.2.6.2 Solution of linear equation systems

The discretization procedure converts every partial differential into a system of linear algebraic equation. Each governing equation has its own unique linear equation system; however they all have the same general form:

$$a_P \phi_P^n + \sum_N a_N \phi_N^n = b \tag{4.79}$$

in matrix notation:

$$\boldsymbol{A} \cdot \Phi = \boldsymbol{b} \tag{4.80}$$

The diagonal elements of matrix $\boldsymbol{A}$ contain a_P, while the off diagonal elements of $\boldsymbol{A}$ contain a_N. Φ is the array of unknown ϕ and $\boldsymbol{b}$ is the source array. Equation (4.80) is solved with an iterative procedure. This procedure starts with an initial guess and improves the solution in every iteration until satisfy the prescribed condition, which is the difference between two consecutive solution. The convergence rate can be improved by applying preconditioning matrix. In this study, for symmetric matrixes the Preconditioned Conjugate Gradient (PCG) solver with Diagonal-based Incomplete Cholesky (DIC) preconditioner was used. For asymmetric matrixes the Preconditioned Bi-Conjugate Gradient (PBiCG) with Diagonal-based Incomplete Lower-Upper (DILU) preconditioner was applied.

In order to ensure boundedness of the phase fraction the solution procedure utilizes the MULES (Multidimensional Universal Limiter for Explicit Solutions) algorithm developed by OpenCFD (OpenCFD, 2008). The algorithm calculates the flux correction as a difference between the higher order flux and the first order upwind flux. Since the flux correction is limited, therefore the new solution for phase fraction will be limited by the extrema determined in all neighbouring cells.

4.3.3 Novel nested 2D/3D approach

The full 3D model is a solid tool to model the gully pot and its environment. However, the heavy computational demand makes its application impractical when the time available restricts the total number of runs. Generally the heavy computational demand can be decreased if the number of control volumes or computational cells is decreased. The grate and gully pot are important area of the model where detailed description of flow is necessary. Furthermore significant reduction cannot be achieved around this area due to the given geometry. Nevertheless the road surface offers a good opportunity to cut back the number of control volumes because approximately half of the total cells of 3D model is the road/street area of the domain. The flow on the road surface is free surface flow. The numerical open channel hydraulics can be regarded as a sub-domain of CFD and the general methods of CFD are applicable in open channel flow modelling. Considering that urban surface flows are usually characterised by turbulence and shallowness and turbulence effects tend to

uniform the velocity profile (except in the near bottom region where viscous effects are no longer negligible), it seems logical to replace the road surface with a 2D model. Many assumptions need to be made in order to simplify the 3D model into 2D one. The following assumptions are applied on 2D model:

- The flow is isothermal and incompressible;
- Boundary layer approximation is applicable due to shallow depth:
    - Tangential derivatives are negligible compared to normal ones;
    - Normal velocity components are negligible compared to tangential ones;
    - Total pressure is constant across the depth;
- The motion is caused by spatial variation in the tangential direction in the total pressure (p_L).

In order to derive the shallow water equations the velocity profile across 2D flow depth must be prescribed (see Figure 4.4):

$$v_i = \left(v_{fs}\right)_i f\left(\eta\right) \tag{4.81}$$

where $f_i(\eta)$ is a velocity profile described by:

$$f_i(\eta) = a_i\eta + b_i\eta^2 + c_i\eta^3 \tag{4.82}$$

$$\eta = \frac{n}{h} \qquad 0 \le n \le h \tag{4.83}$$

The three coefficients for (4.82) are calculated by the following equations:

$$a_i + b_i + c_i = 1 \tag{4.84}$$

$$a_i + 2b_i + 3c_i = p_i \frac{(\tau_{fs})_i h}{\mu_L \overline{v}_i} \tag{4.85}$$

$$2b_i = \frac{p_i h^2}{\mu_L \overline{v}_i}\left[\left(\nabla_s p_L\right)_i - \rho_L\left(g_t\right)_i\right] \tag{4.86}$$

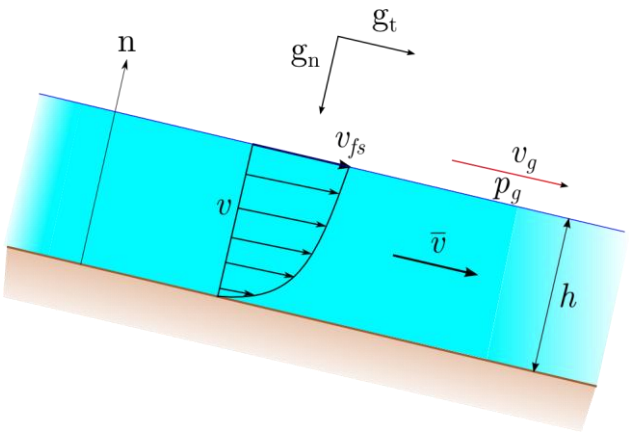

Figure 4.4 – Velocity calculation on 2D domain

4.3.3.1 Spatial discretization

Discretization of the spatial domain results in a two-dimensional computational grid, which consists of a finite number of non-overlapping control surfaces.

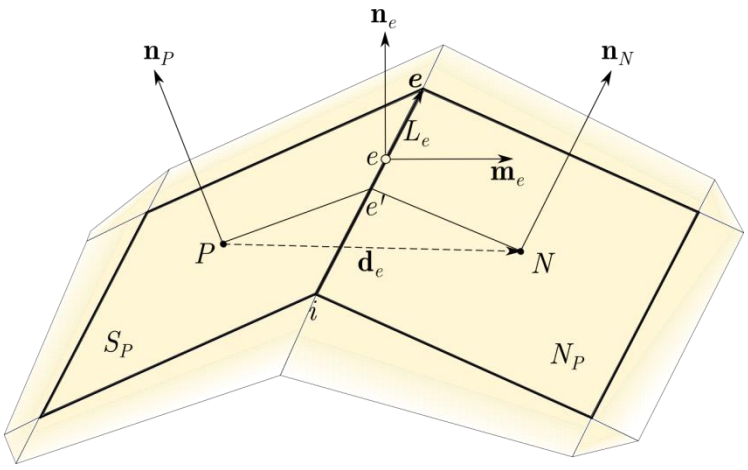

Figure 4.5 – Control surface

Figure 4.5 shows the control surfaces P and N and their common edge e. The sizes of the surfaces are denoted by S_P and N_P. L_e is the length of edge e. The unit normal is calculated by:

$$\boldsymbol{n}_e = \frac{\boldsymbol{n}_i + \boldsymbol{n}_j}{\left|\boldsymbol{n}_i + \boldsymbol{n}_j\right|} \tag{4.87}$$

The bi-normal $\mathbf{m}_e$ is perpendicular to the edge normal ($\mathbf{n}_e$) and to the edge vector ($\boldsymbol{e}$):

$$\boldsymbol{m}_e = \hat{\boldsymbol{e}} \times \boldsymbol{n}_e \tag{4.88}$$

where $\hat{\boldsymbol{e}}$ is a unit vector parallel to the edge. The $Pe'N$ line is a geodesic line connecting the centre of gravity of neighbouring control surfaces. The position of e' is determined by following expression:

$$\boldsymbol{r}'_e = \boldsymbol{r}_i + \beta_e \boldsymbol{e} \tag{4.89}$$

Where $\boldsymbol{r}_i$ and $\boldsymbol{r}_j$ are the position vectors of start and end points of edge e. The β_e coefficient calculated by the following equation:

$$\beta_e = \frac{[\boldsymbol{d}_e \times (\boldsymbol{r}_i - \boldsymbol{r}_P)] \cdot (\boldsymbol{d}_e \times \boldsymbol{e})}{\left|\boldsymbol{d}_e \times \boldsymbol{e}\right|^2} \tag{4.90}$$

where $\boldsymbol{d}_e = \overline{PN}$ and $\boldsymbol{r}_p$ is a vector at centre of gravity of the control surface S.

4.3.3.2 Discretization of transport equation

Transport of surface scalar properties can be described by the following integral equation:

$$\frac{d}{dt}\int_S \psi dS + \oint_{\partial S} \boldsymbol{m} \cdot (\boldsymbol{v}_t - \boldsymbol{b}_t)\psi dL = \oint_{\partial S} \boldsymbol{m} \cdot (\Gamma_\psi \nabla_S \psi) dL + \int_S s_\psi dS \tag{4.91}$$

Similarly to the volume 3D method, the transport equation must be satisfied for each control surface element. Accordingly, the spatial integrals in equation (4.91) should be integrated in the control surface S_P.

$$\frac{d}{dt}\int_{S_P}\psi dS + \oint_{\partial S_P}\boldsymbol{m}\cdot\boldsymbol{v}_t\psi dL = \oint_{\partial S_P}\boldsymbol{m}\cdot(\Gamma_\psi\nabla_S\psi)dL + \int_{S_P}s_\psi dS \tag{4.92}$$

Spatial discretization of (4.92) was carried out assuming linear distribution of the variables on the control surface P:

$$\psi(\boldsymbol{r}) = \psi_P + (\boldsymbol{r}-\boldsymbol{r}_P)\cdot(\nabla_S\psi)_P \tag{4.93}$$

Assuming linear distribution of ψ in time and space is sufficient to achieve a second order accuracy of the discretization method.

4.3.3.3 Discretization of spatial integrals

Taking into account that the control area is limited by straight edges, the line integral over the boundary of control surface can be written as the sum of edges line integrals:

$$\oint_{S_P}\psi(\boldsymbol{r})dL = \sum_e\int_{L_e}\psi(\boldsymbol{r})dL \tag{4.94}$$

Applying the rules of central point:

$$\int_{L_e}\psi(\boldsymbol{r})dL = \psi_e L_e \tag{4.95}$$

where $\psi_e = \psi(\boldsymbol{r}_e)$

4.3.3.3.1 Convection term

Discretization of convective term is carried out using (4.94) and (4.95):

$$\oint_{\partial S_P} \boldsymbol{m} \cdot \boldsymbol{v}_t \psi dL = \sum_e \boldsymbol{m}_e \cdot (\boldsymbol{v}_t)_e L_e \psi_e = \sum_e \dot{s}_e \psi_e \tag{4.96}$$

where $\dot{s}_e = \boldsymbol{m}_e (\boldsymbol{v}_t)_e L_e$

The value of ψ on edge e is calculated from the values of the centre points of adjacent control surface. Using central discretization scheme the value of ψ on the edge is calculated as follows:

$$\psi_e = e_x \psi_P + (1 - e_x)\psi_N \tag{4.97}$$

where the interpolation factor e_x defined as the ratio of $\overline{eN}$ and $\overline{PN}$:

$$e_x = \frac{\overline{eN}}{\overline{PN}} \tag{4.98}$$

4.3.3.3.2 Diffusion term

Using (4.94) and (4.95) the discretised diffusion term can be expressed as follows:

$$\oint_{\partial S} \boldsymbol{m} \cdot (\Gamma_\psi \nabla_S \psi) dL = \sum_e \boldsymbol{m}_e \cdot (\Gamma_\psi \nabla_S \psi)_e L_e = \sum_e (\Gamma_\psi)_e L_e \boldsymbol{m}_e \cdot (\nabla_S \psi)_e \tag{4.99}$$

where $\boldsymbol{m}_e \cdot (\nabla_S \psi)_e$ is a normal surface gradient of ψ on edge e.

Discretization of the surface normal gradient depends on the othogonality of the grid. In this study an orthogonal grid has been used for the 2D domain; therefore there is no need to go into the details of the non-orthogonality issue. In the case of an orthogonal grid the normal surface gradient of ψ on edge e is:

$$\boldsymbol{m}_e \cdot (\nabla_S \psi)_e = \frac{\psi_N - \psi_P}{L_{PN}} \tag{4.100}$$

and

$$(\nabla_S \psi)_P = \frac{1}{S_P}(\boldsymbol{I} - \boldsymbol{n}_P \boldsymbol{n}_P) \cdot \sum_e \boldsymbol{m}_e \psi_e L_e \tag{4.101}$$

where ψ_e is value of ψ on the edge of control surface from the previous iteration.

4.3.3.4 Temporal discretization

After spatial discretization the transport equation has the following form:

$$\frac{d}{dt}(\psi_P S_P) = -\sum_e \dot{s}_e \psi_e + \sum_e (\Gamma_\psi)_e L_e \boldsymbol{m}_e \cdot (\nabla_s \psi)_e + s_{\psi u} S_P + s_{\psi p} S_P \psi_P \tag{4.102}$$

Using the implicit Gear method for time discretization a fully discretised transport equation has the following form:

$$\begin{aligned} &\frac{3\psi_P^n S_p^n - 4\psi_P^o S_P^o + \psi_P^{oo} S_P^{oo}}{\Delta t} + \sum_e \dot{s}_e^n \psi_e^n \\ &= \sum_e (\Gamma_\psi)_e^n L_e^n \boldsymbol{m}_e^n \cdot (\nabla_s \psi)_e^n + s_{\psi u}^n S_P^n + s_{\psi p}^n S_P^n \psi_P^n \end{aligned} \tag{4.103}$$

4.3.3.5 Solution of linear equation systems

Taking into account that ψ_e^n, $\boldsymbol{m}_e^n$ and $(\nabla_s \psi)_e^n$ do not depend on the value of ψ at the centre of adjacent control surface at the time t^n, similarly to 3D model the linear equations has the following from:

$$a_P \psi_P^n + \sum_N a_N \psi_N^n = r_P \tag{4.104}$$

In case of combined convection discretization and the Gear time discretization method the coefficients and the right side of the equation are defined by the following expression:

$$\begin{aligned} a_P = \frac{3S_P^n}{2\Delta t} &+ \sum_e \dot{s}_e^n \left[\left(1 - \gamma_f^n\right) \max\left(\operatorname{sgn}\left(\dot{s}_e^n\right), 0\right) + \gamma_e^n e_x^n \right] \\ &+ \sum_e (\Gamma_\psi)_e^n L_e^n \frac{\left|\Delta_e^n\right|}{\left|\boldsymbol{d}_e^n\right|} - s_{\psi p}^n S_P^n \end{aligned} \tag{4.105}$$

$$a_N = \dot{s}_e^n \left[\left(1-\gamma_e^n\right) \min\left(\mathrm{sgn}\left(\dot{s}_e^n\right),0\right) + \gamma_e^n \left(1-e_x^n\right) \right] - \left(\Gamma_\psi\right)_e^n L_e^n \frac{\left|\Delta_e^n\right|}{\left|\boldsymbol{d}_e^n\right|} \tag{4.106}$$

$$r_P = \frac{4S_P^o \psi_P^o - S_P^{oo} \psi_P^{oo}}{2\Delta t} + \sum_e \left(\Gamma_\psi\right)_e^n L_e^n \boldsymbol{k}_e^n \cdot \left(\nabla \psi\right)_e^n + s_{\psi u}^n S_P^n \tag{4.107}$$

where γ_e^n is the combination factor of central and upwind discretization of the convective term.

4.3.3.6 2D/3D Link

A special type of boundary has been used to connect the 2D domain to the 3D mesh. This switches velocity and pressure between fixed value and zero gradient type boundaries, depending on direction of velocity. The fixed value boundary is when the value of ψ is specified. The zero gradient boundary means the normal gradient of ψ is equal to zero.

4.3.3.6.1 Edge-face mapping

The CFD model defines a mesh of arbitrary polyhedral cells in three dimensions, bounded by arbitrary polygonal faces. The cell faces can be divided into two groups: internal faces and boundary faces, which coincide with the boundaries of the domain. Faces are formed by edges and edges defined by points in 3D space. The highest rank common element of two-dimensional grid and three-dimensional mesh is the edge. Figure 4.6 shows the common edges of 2D grid and 3D mesh marked with different colours (red, yellow, blue, etc.). The edge is part of a face on the 3D domain and there is a series of faces above it. The first step in the 2D/3D link is to create the edge-face array or database which serves the basis for further calculation.

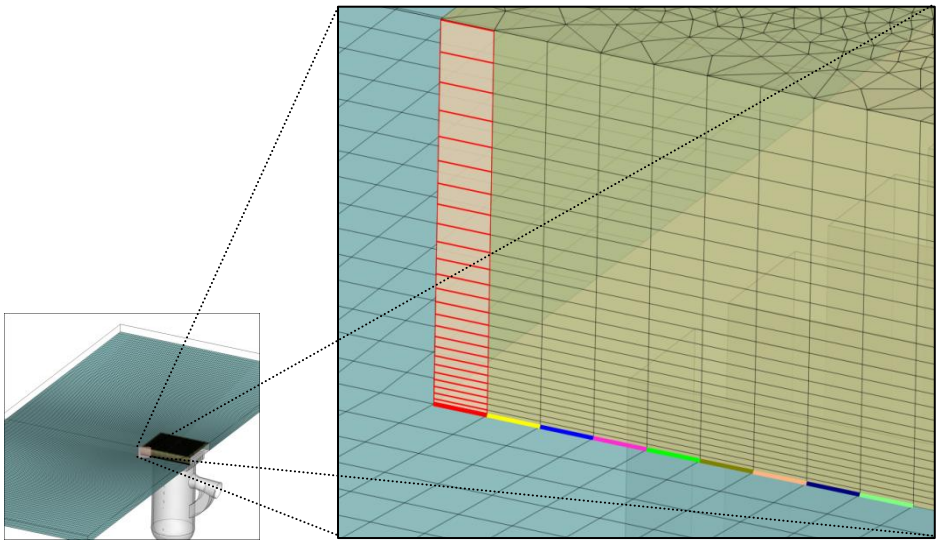

Figure 4.6 – Edge-face mapping

The edge-face database contains the ID of element, length, area, and its coordinates and ID of neighbouring elements.

4.3.3.6.2 From 2D to 3D

Two flow directions can be distinguished in the model: flow from 2D to 3D and flow from 3D to 2D domain. The 3D and 2D domains are dynamically linked, therefore both models are able to receive and send the necessary parameters to the other one. As mentioned earlier, p, h and v are the working parameters in the 2D domain. The details of the 3D model have been discussed in the previous chapter. If we compare these parameters it can be seen that pressure and the velocity are calculated by both models, but the water depth is not. On the 3D side the free surface is captured by the VOF method, where an indicator function gives a value of 1 if the cell is filled by water and 0 if it is empty. The Figure 4.7 and equation (4.108) shows how the water level from the 2D model is converted to a γ value on the 3D domain.

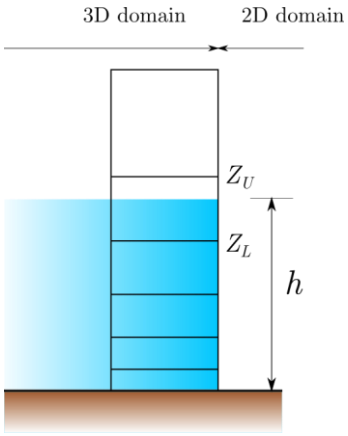

Figure 4.7 – Transfer the water level from 2D to 3D

$$\begin{aligned} h \geq Z_U \quad & \rightarrow \gamma = 1 \\ Z_L < h < Z_U \quad & \rightarrow \text{interpolate } \gamma \\ Z_L < h \quad & \rightarrow \gamma = 0 \end{aligned} \tag{4.108}$$

In the first step the water level from 2D is compared to the upper edge (Z_U) of a face. If the water level is higher or equal to the elevation of the upper edge, then a value of 1 is assigned to the cell. In second step the water level is compared to the lower edge (Z_L) of a face. If the water level is lower than the elevation of the lower edge, then a value of 0 is assigned to the cell. If the first two assumptions are false then the water level is between the upper and lower edge of a face. In this case linear interpolation is used to calculate the γ value.

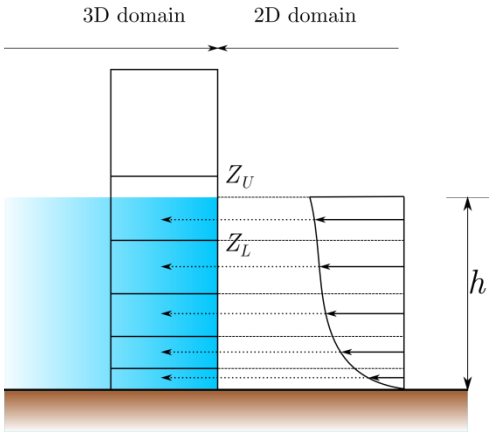

Figure 4.8 – Velocity transmission from 2D to 3D

As mentioned above the velocity in the 2D domain is calculated by a prescribed velocity profile. The velocity profile is defined by equation (4.81) - (4.86). This velocity distribution is sliced by the upper and lower edge of a face and assigned to the appropriate cell on 3D domain (Figure 4.8). Inasmuch as the velocity is a vector both magnitude and direction is transmitted to the 3D domain.

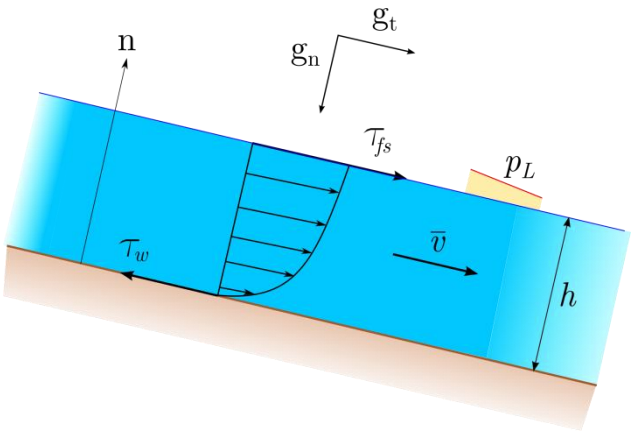

Figure 4.9 – Schematic for momentum calculation on 2D domain

The momentum equation on 2D domain described by the following equation:

$$\begin{aligned}&\int_{S_w} \frac{\partial h\bar{\boldsymbol{v}}}{\partial t} dS + \oint_{\partial S_w} m \cdot (h\bar{\boldsymbol{v}}\bar{\boldsymbol{v}} + \boldsymbol{C}) dL \\ &= \frac{1}{\rho_L} \int_{S_w} (\tau_{fs} - \tau_w) dS + \int_{S_w} h g_t dS - \frac{1}{\rho_L} \int_{S_w} h \nabla_s p_L dS + \frac{1}{\rho_L} \int_{S_w} \bar{\boldsymbol{S}}_v dS\end{aligned} \tag{4.109}$$

where $\bar{\boldsymbol{S}}_v$ is given by:

$$\bar{\boldsymbol{S}}_v = \frac{\sum_i m_{d,i} (v_{d,i})_t}{dt \; dS} \tag{4.110}$$

The shear stress terms and the convection term correction tensor C are calculated from the prescribed velocity profile. p_L is the liquid pressure described by the following equation:

$$p_L = p_g + p_d + p_\sigma + p_h \tag{4.111}$$

where p_g is the air pressure, p_d the droplet impact pressure, p_σ capillary pressure and p_h the hydrostatic pressure. The components of the total pressure equation are calculated by following equations:

$$p_{d,i} = \frac{\rho(v_{d,i})_n^2}{2} \tag{4.112}$$

$$p_\sigma = -\sigma \nabla_s \cdot (\nabla_s h) \tag{4.113}$$

$$p_h = -\rho_L n \cdot gh \tag{4.114}$$

The pressure assigned to the 3D cell in a similar way as described for flow velocity.

4.3.3.6.3 From 3D to 2D

When the flow direction is from 3D to 2D domain the same parameters need to be transmitted to the 2D model as above. First step is converting the interface on 3D into water depth using the area of a face (A_i), the γ parameter from VOF and the edge length (L_E) (see Figure 4.10):

$$h = \frac{\sum_i \gamma_i A_i}{L_E} \tag{4.115}$$

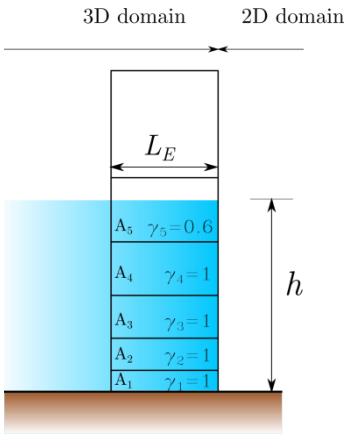

Figure 4.10 – Transfer water level from 3D to 2D

In the case of the velocity, the necessary parameters for equation (4.81) - (4.86) are calculated by 3D model except $\overline{v}$. The following equation is used to calculate the average velocity:

$$\overline{v} = \frac{1}{h}\int_0^h v dh \tag{4.116}$$

4.4 Mesh Creation

Once the problem has been specified an appropriate set of governing equations and boundary conditions have been selected. Next step is dividing the flow domain into cells. The design and construction of a quality mesh is crucial to the success of CFD analysis. The mesh has a significant impact on the rate of convergence, solution accuracy and CPU time required. Many different meshing strategies exist, including structured, unstructured, hybrid, composite and overlapping grids. The choices of numerical method and gridding strategy are strongly interdependent.

Traditionally, grids have been divided into structured and unstructured grids. The structured grids are built up from quadrilateral elements. Therefore the structured grids have a well defined structure, from which the neighbours of a particular volume can be readily deduced on the basis of the location of the volume in the structure. Usually, a structured grid requires less memory and has better numerical properties. However it is difficult to mesh complex geometries using structured meshes.

The structured meshes have the following characteristics in common:

- A simple data structure is used to describe the mesh;

- All cells have a similar shape;
- Cell faces and edges can be mapped to lie parallel to coordinate axes;
- Mesh quality deteriorates with increasing complexity of the domain

One characteristic used to distinguish between structured and unstructured meshes is the existence of an obvious mapping between logical space and physical space for the mesh (Hansen, et al., 2005). Unstructured grids are built from different elements, mainly from triangular ones. In case of unstructured grids the volumes can be ordered arbitrarily. The connections between the neighbours have to be defined explicitly.

The unstructured meshes have the following properties in common:

- The data structures is more complex;
- Cells have variable local topology and size;
- Cell faces and edges do not have an implied orientation;
- Mesh quality remains high as the domain complexity increase.

The meshing process can be divided into the following steps:

1. Geometry definition
2. Geometry decomposition
3. Mesh generation
4. Checking mesh quality, refining
5. Definition of boundary conditions

In the phase of defining the mesh we need to take into account whether the solver is uses a cell centred or a node centred algorithm. A cell centred solver creates control volumes that are completely identical to the grid. A node

centred solver creates its control volumes around the grid nodes instead (Andersson, et al., 2012). In this study the cell centred solver was used. Two different meshes have been built for the CFD simulation. Firstly an unstructured tetrahedral mesh, secondly a hybrid (mixture of tetra- and hexahedral) one was built. The hybrid mesh offers greater flexibility. The curved surfaces, the gully pot and grate are described by tetrahedral cells, while the road surface is described by hexahedral elements. The colour coded Figure 4.11 shows the different parts of hybrid mesh: brown for hexahedral part and grey for the tetrahedral region. The reason why hexahedral element are chosen for the road surface is that the analysis of the free surface interface shows the VOF method is working better with hexahedral cells. The tetrahedral domain makes the water surface artificially bumpy.

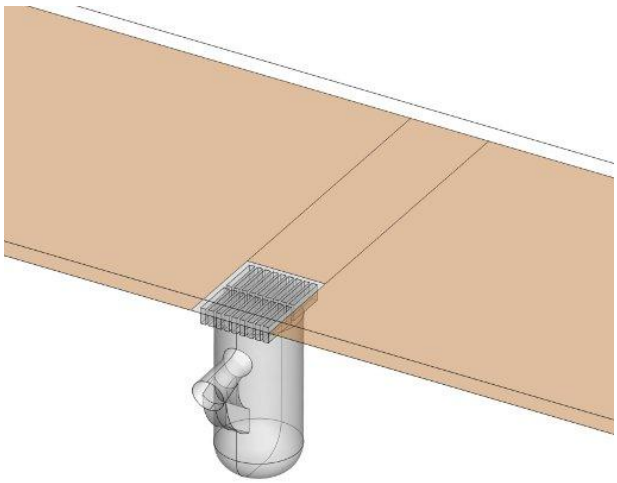

Figure 4.11 – Parts of hybrid mesh: brown area hexahedral, grey area tetrahedral

Pointwise software system was used for mesh and grid generation. Pointwise generates structured, unstructured and hybrid grids. The element types it makes include triangles, quadrilateral, tetrahedral, pyramids, prisms and hexahedra. Pointwise divides the overall region to be gridded into one or more sub-regions called blocks. It can be used to generate both 2D and 3D blocks. 2D block consists entirely of surface cells while a 3D block contains entirely volumetric cells. All blocks in the same grid must either be 2D or 3D; blocks of differing dimensionality cannot be combined (Pointwise, 2008).

4.4.1 Tetrahedral mesh

The mesh consists of 954,551 tetrahedral cells or control volumes. The tetrahedral mesh is formed by 199,394 nodes. Some grid refinement is used in the lower part of the region. The resolution varies between 2 mm and 0.07 m. Using a pure tetrahedral mesh does not allow describing the boundary layers with very much detail compared to a hybrid mesh. (Wilkening, et al., 2006)

4.4.2 Hybrid mesh

As a second grid, a hybrid grid was generated. This mesh was used with three different grates. Figure 4.12 shows the mesh of grates and Table 4.1 their hydraulic properties.

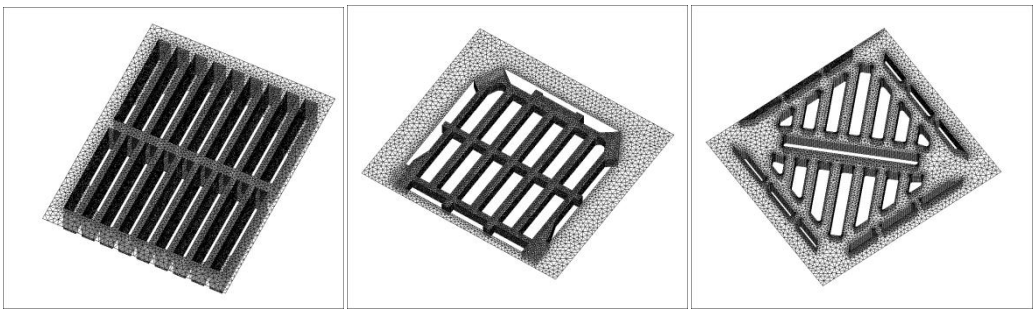

a) Waterflow b) Watershed c) Briflo

Figure 4.12 – Mesh of grates used in numerical simulation (Waterflow used in laboratory experiment)

Table 4.1 – Physical properties of modelled grates **(Sain-Gobain Pipelines, 2007)**

Loading class	Clear opening AxB [mm]	Over base CxD [mm]	Depth E [mm]	Waterway area [cm^2]	HA102 reference
Waterflow	325 x 437	475 x 524	75	933	S
Watershed	380 x 400	525 x 490	75	940	S
Briflo	465 x 465	620 x 570	140	880	-

The grid with the grate used in physical experiment (Waterflow) is composed of 951,892 nodes and 1,546,726 elements (581,176 tetrahedrons, 628,100 hexahedrons and 337,450 prisms). Starting from a structured surface grid, quadrilateral elements are extruded into the volume for a few layers to allow a fine resolution of the boundary layer developing on the road surface. Starting from an unstructured grid, a tetrahedral mesh is filling the gully pot and grate. Additional mesh refinement is used in the grate holes, water seal and rodding eye. The mesh resolution goes from 1 mm in the regions close to the wall, to 0.08 m in regions far from the walls. Table 4.2 summarize the properties for different meshes used in numerical simulation.

Table 4.2 – Mesh properties with different grates

Cell type	**Grate**			
	Briflow	Watershed	Waterflow	Waterflow
Tetrahedral	699,548	632,279	581,176	954,551
Hexahedral	589,275	589,275	628,100	0
Pyramid	0	0	0	0
Prism	602,050	477,525	337,450	0
Total Cells	1,890,873	1,699,079	1,546,726	954,551
Total Nodes	1,068,891	985,507	951,892	199,394

Elements at the walls need to be handled carefully. It is recommended for flows with attached boundary layer that the mesh includes a few layers of thin cells adjacent to the wall (Zikanov, 2010). In this study the flow approximated on a stretched grid adapted to solution gradients. Near wall treatment depends on y^+ a dimensionless distance of the first grid point from the wall (Wilkening, et al., 2006). For y^+ the following relations are valid:

$$u^+ = \frac{u_t}{u_\tau} = \frac{1}{\kappa}\ln(y^+) \tag{4.117}$$

where

$$y^+ = \frac{\rho \Delta y u_\tau}{\mu} \tag{4.118}$$

$$u_\tau = \left(\frac{\tau_\omega}{\rho}\right)^{\frac{1}{2}} \tag{4.119}$$

u^+ is the near wall velocity, u_τ is the friction velocity u_t is the known velocity tangent to the wall at a distance of Δy from the wall, κ is the Von Karman constant. The optimal value of y^+ is lies between 5 and 10 (Andersson, et al., 2012). As the k-ω SST turbulence model is used at walls an automatic near wall treatment is enforced. If y^+ is outside the desired range a special treatment is applied. This has the advantage that it prevents the regeneration and adjustment of mesh to y^+ according to the geometrical and flow conditions.

4.4.3 Mesh quality

Appropriate choice of mesh type depends on the geometric complexity of computational domain, the flow field and cell element types supported by solver. Preparing a good initial mesh usually requires the pre-knowledge or insight to the expected properties of the flow. The general way to eliminate the errors is to embrace the procedure of successive refinement of an initial mesh until certain key results shows no appreciable changes. An important aspect of the mesh generation is choosing the appropriate size of the mesh element. The general rule is that no fluid particle should advance through multiple mesh elements in one time step.

In addition to mesh density the quality of a mesh depends on various criteria such as the shape of the cells (aspect ratio, skewness, included angle of adjacent faces), distance of cell faces from boundaries or spatial distribution of cell sizes. The most common sources of errors are:

- Mesh too coarse;
- High skewness;

- Large jumps in volume between adjacent cells;
- Large aspect ratios;
- Interpolation errors at non-conformal interfaces;
- Inappropriate boundary layer meshes.

Numerous quality functions can be used to determine the quality of a mesh. Here the quality of mesh was analysed using commonly used mesh quality parameters: equiangle skewness, equivolume skewness, aspect ratio and volume ratio.

The equiangle skewness (Q_{EAS}) is a normalized measure of skewness that is defined as:

$$Q_{EAS} = \max\left\{\frac{\theta_{\max} - \theta_{eq}}{180 - \theta_{eq}}, \frac{\theta_{eq} - \theta_{\min}}{\theta_{eq}}\right\} \tag{4.120}$$

where $\theta_{\max}$ and $\theta_{\min}$ are the maximum and minimum angles between of the edges of the element, θ_{eq} is 60 for tetrahedral element and 90 for hexahedral one.

The value of θ_{EAS} lies between 0 and 1, where 0 describes an equilateral element and 1 describes poorly shaped element. In general, high quality meshes contain elements that possess average Q_{EAS} values of 0.4 (ERCOFTAC, 2000), (Menter, 2002), (MARNET-CFD, 1999), (ANSYS, 2006)

Equivolume skewness is defined as:

$$Q_{EVS} = \frac{S_{eq} - S}{S_{eq}} \tag{4.121}$$

where S is the volume of the mesh element and S_{eq} is the maximum volume of an equilateral cell the circumscribing radius of which is identical to that of the mesh element.

Aspect ratio is defined as:

$$Q_{AR} = f\frac{R}{r} \tag{4.122}$$

where f is a scaling factor equal to 1/3 for tetrahedral elements, r and R represent the radii of the spheres that describe and circumscribe the mesh element. Whenever possible, it is recommended to keep Q_{AR} within the range of $0.2 < Q_{AR} < 5$.

The volume ratio analogue to aspect ratio, represents the maximum volume ratio of any given control volume relative to its neighbouring elements:

$$r_j = \frac{V_i}{V_j} \tag{4.123}$$

and

$$Q_{VR} = \max[r_1, r_2, ..., r_n] \tag{4.124}$$

Where V_i is the volume of the cell i, V_j is the volume of neighbouring element j and n is the total number of elements adjacent to element i.

Figure 4.13 shows the minimum, maximum, average and distribution of above mentioned mesh quality parameters for a hybrid mesh. Comparing the average values to guidelines (ERCOFTAC, 2000) (Andersson, et al., 2012) (ANSYS, 2006) (MARNET-CFD, 1999) it can be stated that the mesh satisfies the requirements of high quality mesh.

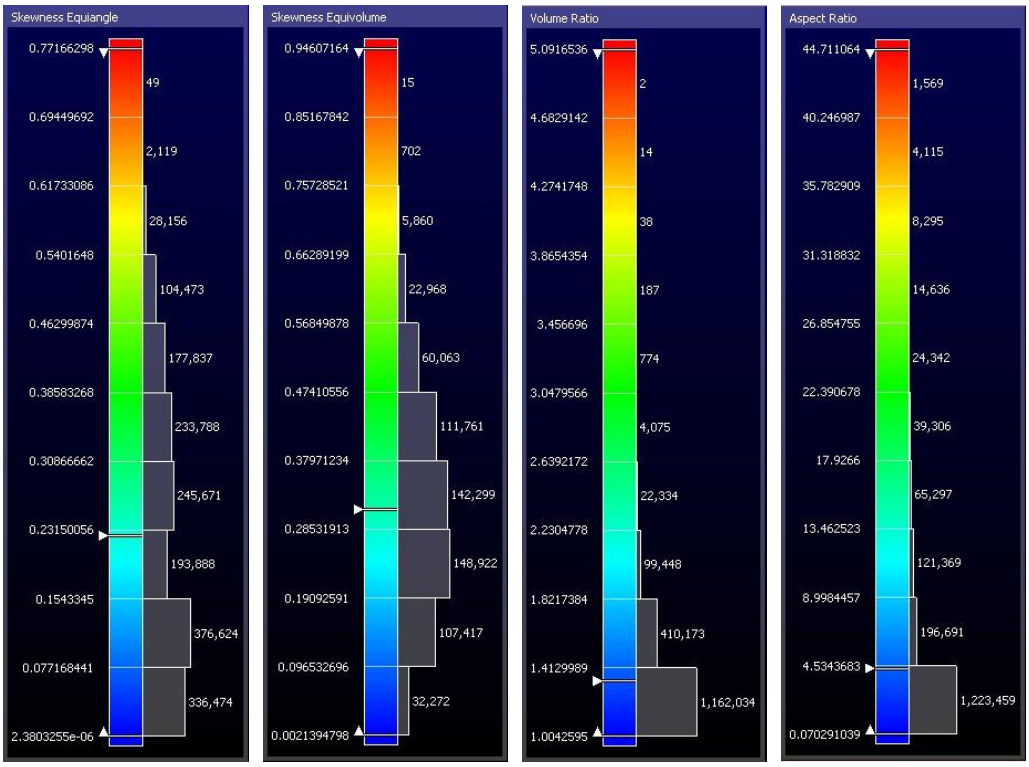

Figure 4.13 – Mesh quality parameters: a) skewness equiangle b) skewness equivolume c) volume ratio d) aspect ratio

Chapter 5

Results

5.1 CFD Model validation

The CFD model is, like any other mathematical model, a simplified representation of a complex physical process. The results obtained are therefore based on many assumptions and are dependent upon the ability of the program to successfully and accurately assimilate vast quantities of data and solve highly complex mathematical problems. Model validation is a necessary requirement for model application.

The effect of grid density was conducted by comparing the fine mesh results to the ones obtained on a coarser mesh. There results were found to be close at most locations, thought the finer mesh results gave better agreement in some areas.

5.1.1 Flow into gully

Two different set ups have been used for depth measurement. The first set up (preliminary test) used the point-gauge equipment to monitor the flow depth at 51 locations. Figure 5.1 (a) shows the location of depth measurement points marked with pink dots. The monitoring points comprise a 2.40 m long and 0.75 m wide grid. The distance between the points is 0.30 m in the longitudinal direction and 0.15 m in the transversal direction. The depth was measured at each point after the flow reached a steady state condition. This set up has also been used to calibrate the pressure transducers.

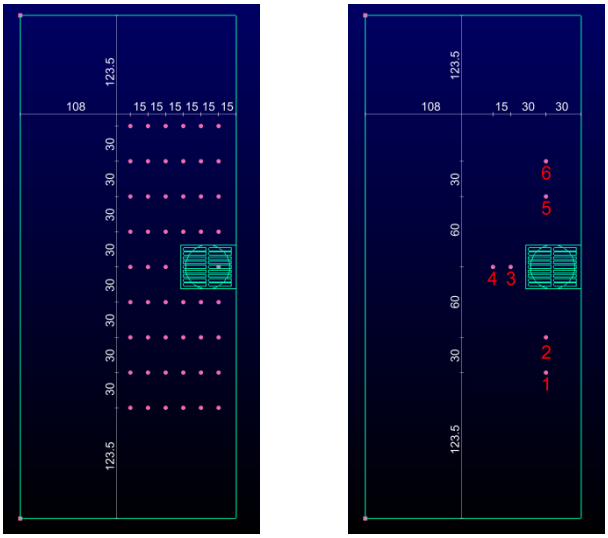

(a) (b)

Figure 5.1 – Monitoring location: (a) preliminary test and (b) final test

The second set up (final test) used the GEMS 5000 sensors to measure the flow depth at seven locations. Six pressure transducers have been set up in the rig platform and one at the bottom of the gully pot. Figure 5.1 (b) shows the position of transducers in the rig platform. The positions are 30 cm equally from the centre of the grates and consecutively in order to give an average hydraulic

depth of the flow going into the gully gratings on all sides (Sabtu, 2012). The big advantage of pressure transducers, opposite to point-gauge, is that they allow continuous measurement of flow depth without disturbing the flow on the rig platform.

5.1.1.1 Preliminary test

The preliminary test was used to calibrate the pressure transducers using the point-gauge. Only the intermediate configuration (Figure 3.8) was tested with the following parameters:

- inflow: 6.0 l/s, 10.5 l/s, 19.9 l/s, 23.8 l/s, 26.9 l/s, 29.6 l/s;
- longitudinal slope: 0%;
- cross-slope: 0%;
- grate: Waterflow and without grate.

The full 3D numerical model used tetrahedral mesh for preliminary validation. The details of mesh have been discussed earlier and can be found under section 4.4.1. The results presented below are based on the 26.9 l/s inflow.

Visual examination of flow features has been accomplished before the numerical comparison of observed and modelled depth. Figure 5.2 shows the progress of flood wave. The member of University of Sheffield research team experimented with similar wave progress and flow outline during the rig test. The shape of tail water (at outflow) was very similar to the observed one. Figure 5.3 and Figure 5.4 shows the shape of modelled and observed tail water.

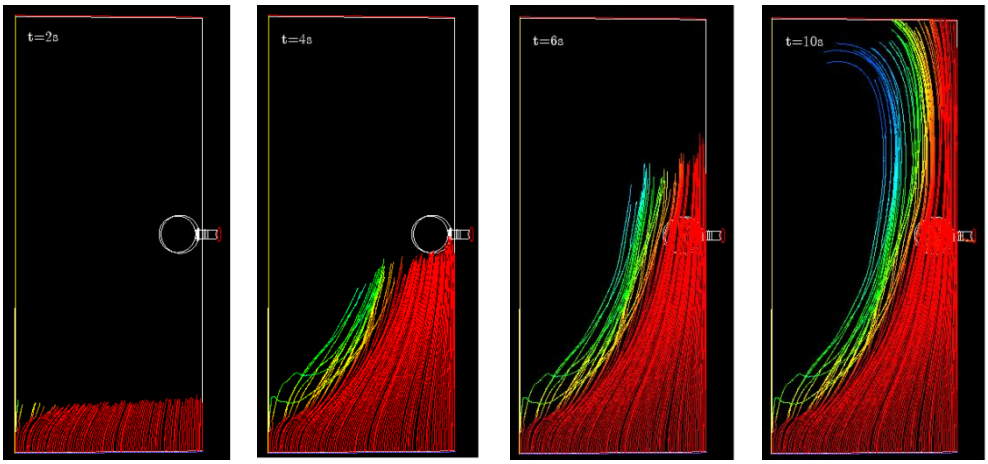

Figure 5.2 – Progress of flow in time (full 3D model)

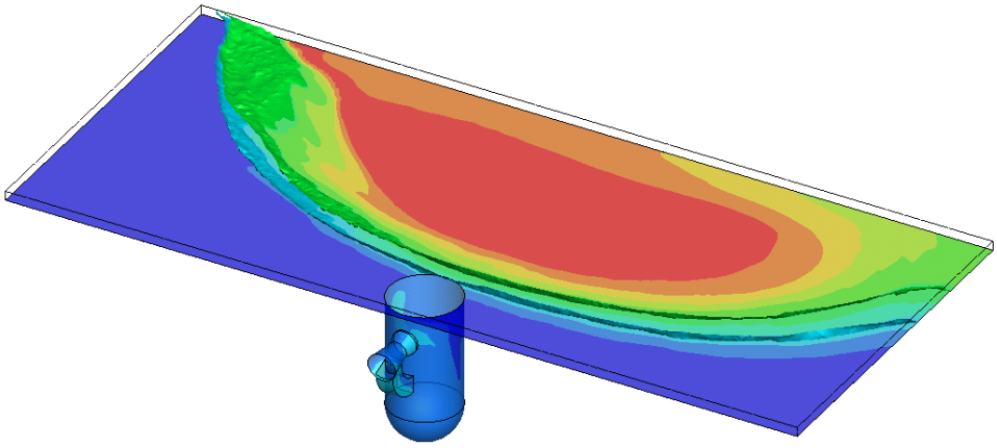

Figure 5.3 – Modelled tail water (flow direction from left to right), full 3D model

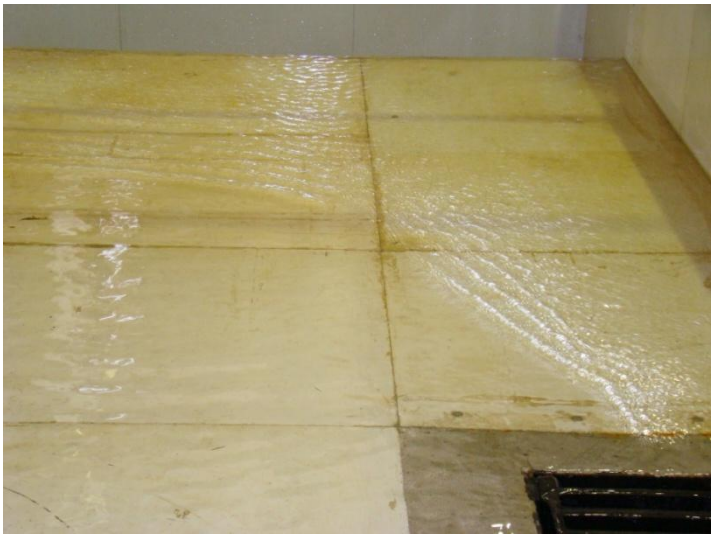

Figure 5.4 – Observed tail water (looking downstream)

Other valuable observations are the flow circulation at the gully inlet and ridge formation. When the opening is fully covered the water front produces undulant ridges. The ridge occurs above the inlet itself (Figure 5.5).

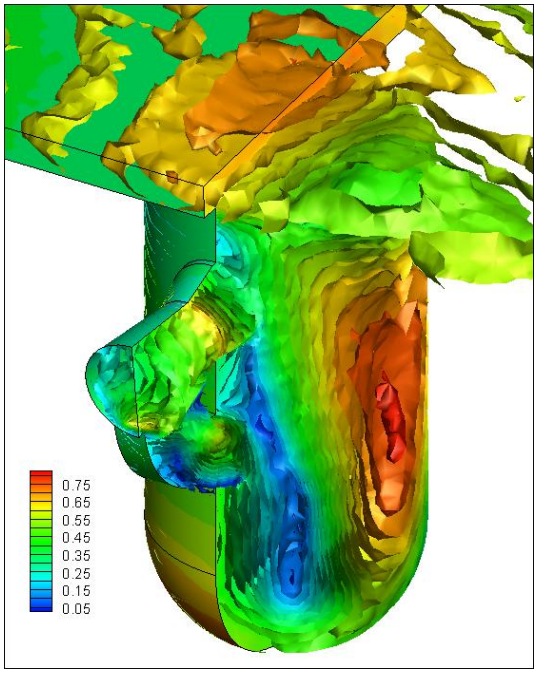

Figure 5.5 – Velocity distribution and ridge formation above gully inlet (the unit of velocity is m/s), full 3D model

As the discharge gets higher, the ridge moves downstream. The pattern of water circulation occurs at the same place. According to these observations, the model was behaving well and was able to describe the mechanism of flow.

The comparison of measured and observed depth values resulted in similar conclusions. The simulated depth was very close to the observed one.

During the analysis of the water surface at monitoring sections the "bumpiness" of the interface has been detected. Figure 5.6 shows the observed and modelled water levels at three sections (0.9 m, 0.6 m and 0.3 m) upstream of the gully pot. The water is marked with red and the air is with blue, the white dots are the observed water levels.

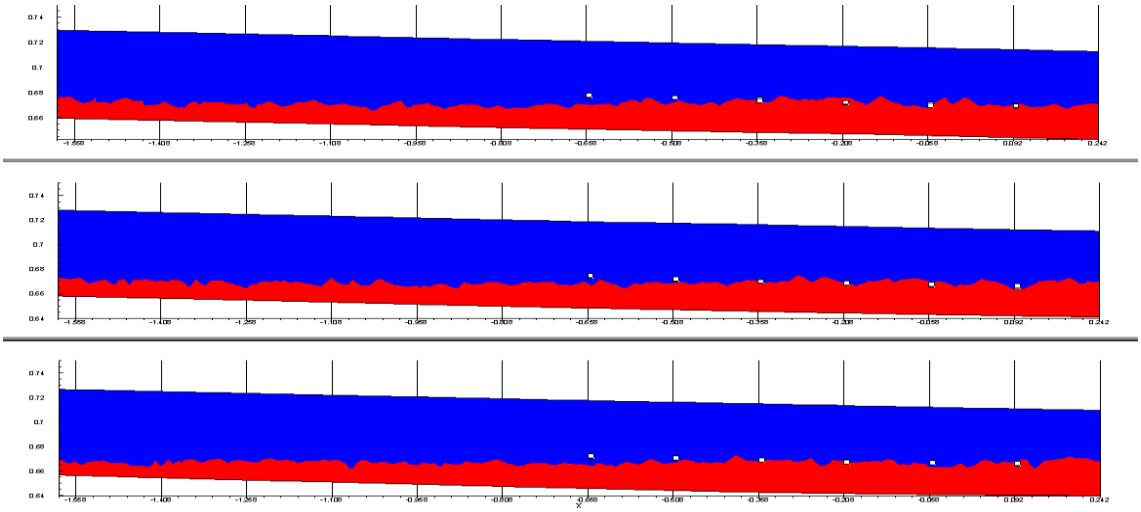

Figure 5.6 – Observed and modelled water levels upstream of gully (from up to down: 0.9 m, 0.6 m and 0.3 m upstream from gully), full 3D model

Investigation of possible causes revealed that the tetrahedral mesh is not adequate for the VOF method. It became obvious that the geometric construction of the interface is working better with hexahedral cells. Therefore the platform or road surface has been replaced by hexahedral elements and later with 2D cells.

5.1.1.2 Final test

The final experimental test involves two type of grates, namely Waterflow 250 "S" and Waterflow 250 "R". These inlets and their physical parameters are presented in Figure 3.4 and Table 3.1. The gratings were investigated under terminal, intermediate and surcharged conditions. The details of the numerical model have been discussed in previous chapter. Constant inflow simulations were run until the depth and velocity magnitude were found to be practically invariant at the monitoring locations. Typically 40,000-60,000 iterations were needed to obtain fully converged solutions. Most of the simulations employing

hybrid meshes with 1.5 million cells were running on 4 processors. The average time to get a solution starting from scratch was about 3-5 days.

The analysis and interpretation of measured depth data requires specific data representation and description. Descriptive statistics provides simple summaries about the observation. These summaries formed the basis of initial description of the observed data and its statistical investigation. The descriptive statistics were calculated for each monitoring location and each scenario. They provide basic information such as mean, minimum and maximum values, different measures of variation, as well as data about the shape of the distribution of the measured depth. These statistical functions were sufficient for the investigation in most cases. However when it was necessary more extensive statistical analysis was performed. An example of statistical analysis for intermediate condition with 26.9 l/s inflow is shown below. Figure 5.7 shows the graphical representation of a water depth time series. The D1, D2, D3, D4 and D6 time series have a similar range, while D5's range is wider by 50%.

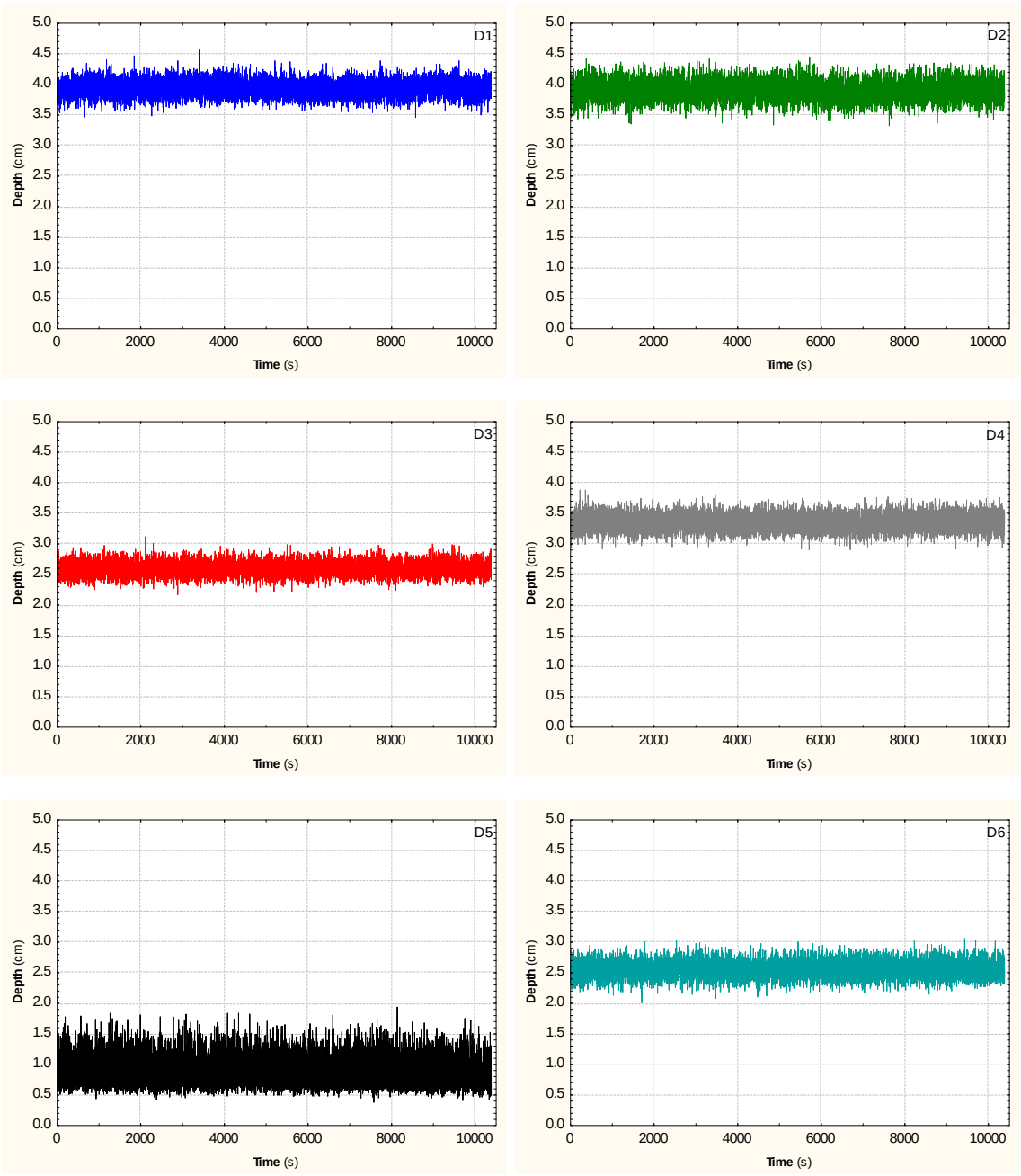

Figure 5.7 – Measured depth time series at monitoring locations D1-D6

(intermediate conditions, inflow = 26.9 l/s)

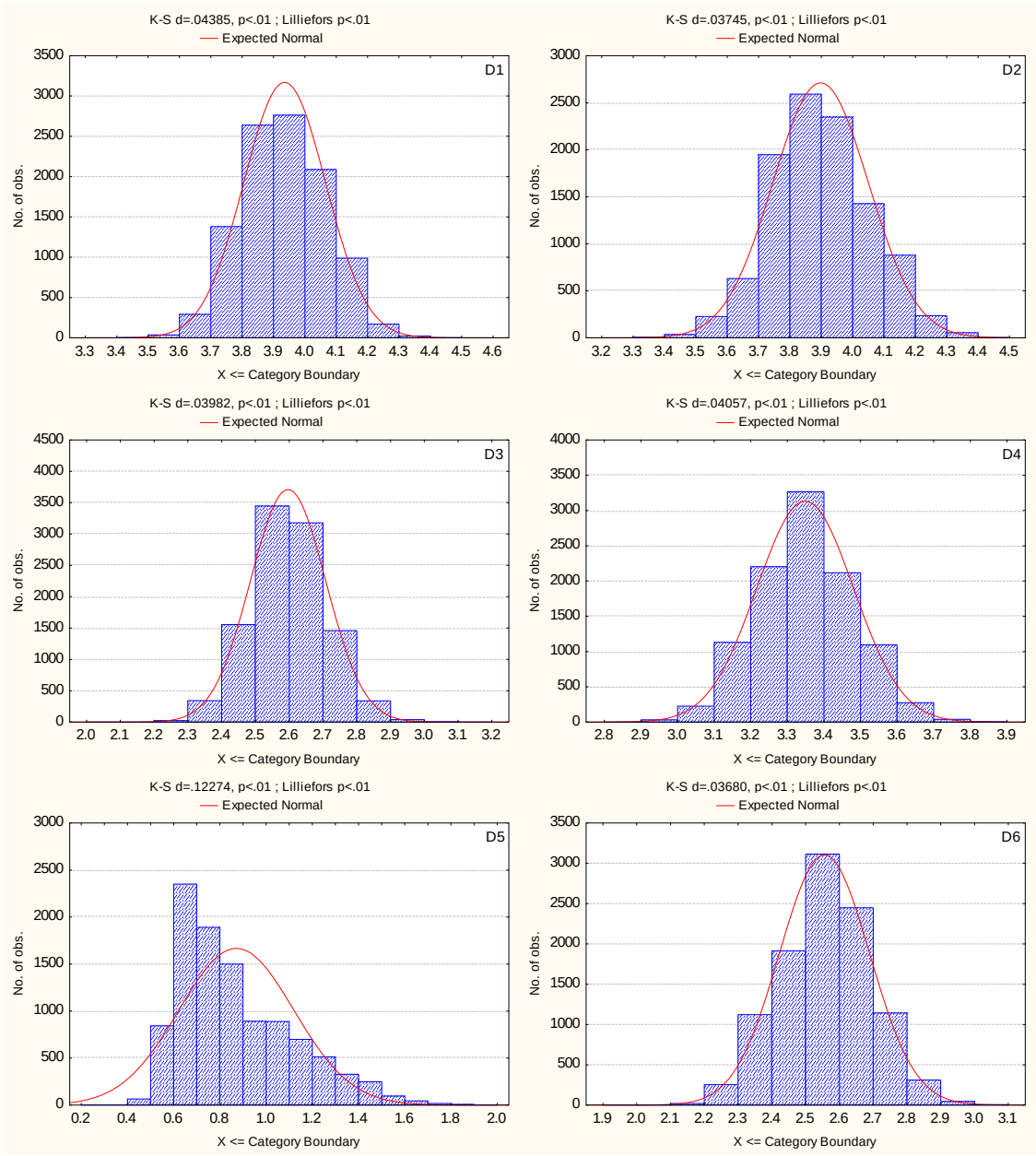

Figure 5.8 – Histograms of depth for six monitoring locations (D1-D6) (intermediate condition, inflow = 26.9 l/s)

These ranges are (0.953 cm-1.553 cm) unusually high if we consider that steady state or nearly steady state conditions were achieved during the test.

Figure 5.8 shows the distribution histograms for six monitoring locations. The plot indicates the normal distribution curve and the result of goodness of fit tests, namely the Kolmogorov-Smirnov and Liliefors statistics. The Kolmogorov-

Smirnov test is designed to assess the goodness of fit of a data sample to a hypothesised continuous distribution. The Liliefors test for normality resembles the Kolmogorov-Smirnov test but it is especially tailored to assess the normality of a distribution. The skewness, kurtosis and goodness of fit tests show that the distribution is normal at location D1, D2, D3, D4 and D6. The only exception is D5.

Table 5.1 – Descriptive statistics of depth measurement (intermediate condition, inflow = 26.9 l/s)

Statistical function	**Monitoring location**					
	D1	**D2**	**D3**	**D4**	**D5**	**D6**
Sample size	10384	10384	10384	10384	10384	10384
Mean	3.935	3.898	2.597	3.349	0.871	2.556
Confidence -95%	3.933	3.895	2.594	3.346	0.867	2.553
Confidence +95%	3.938	3.901	2.599	3.351	0.876	2.558
Geometric mean	3.933	3.895	2.594	3.346	0.839	2.552
Harmonic mean	3.931	3.892	2.592	3.344	0.810	2.549
Median	3.938	3.893	2.597	3.343	0.810	2.563
Mode	3.963	3.879	2.584	3.333	0.651	2.549
Frequency of mode	486	462	490	437	397	507
Minimum	3.459	3.323	2.168	2.904	0.381	2.007
Maximum	4.566	4.451	3.121	3.884	1.938	3.062
Lower quartile	3.842	3.798	2.513	3.256	0.681	2.466
Upper quartile	4.019	4.006	2.668	3.431	1.024	2.646
Percentile 10	3.772	3.703	2.454	3.181	0.610	2.384
Percentile 90	4.101	4.101	2.739	3.519	1.236	2.729
Range	1.107	1.128	0.953	0.980	1.557	1.055
Quartile range	0.177	0.209	0.154	0.176	0.344	0.180
Variance	0.017	0.023	0.012	0.018	0.062	0.018
Standard deviation	0.131	0.153	0.112	0.132	0.249	0.133
Standard error	0.001	0.001	0.001	0.001	0.002	0.001
Skewness	0.052	0.098	0.106	0.081	0.917	0.045
Kurtosis	-0.115	0.090	-0.008	-0.124	0.284	-0.022

Comparing the values of statistical functions for six monitoring locations (see Table 5.1) it became obvious that the behaviour of water depth at D5 is different from the other locations. The issue was investigated by checking the CFD results around the location of D5 probe. Later the result of CFD analysis was supported by photos from the Sheffield Laboratory. The CFD analysis shows that under certain conditions, flow bypassing outside of the grating meeting flow bypassing inside of the grating produced a jump in the water surface, resulting in flow back into the gully. The water surface variation looks like a hydraulic jump although it is not the classical hydraulic jump in all cases. Inasmuch as sufficient total head difference was maintained between the inside and outside bypassing water the water surface variation was maintained. Figure 5.9 shows the water surface and the position of water surface variation based on CFD simulation.

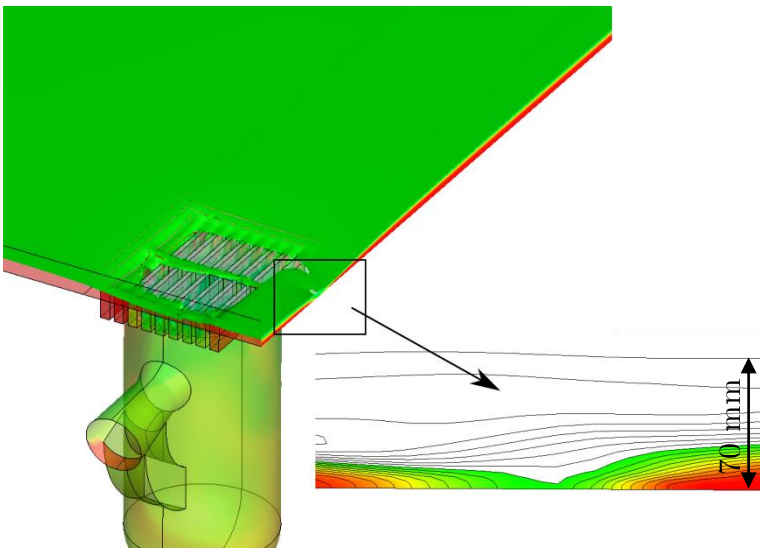

Figure 5.9 – Location of water surface variation, full 3D model

The position of water surface variation is changing in time due to the changing hydraulic conditions behind the grating.

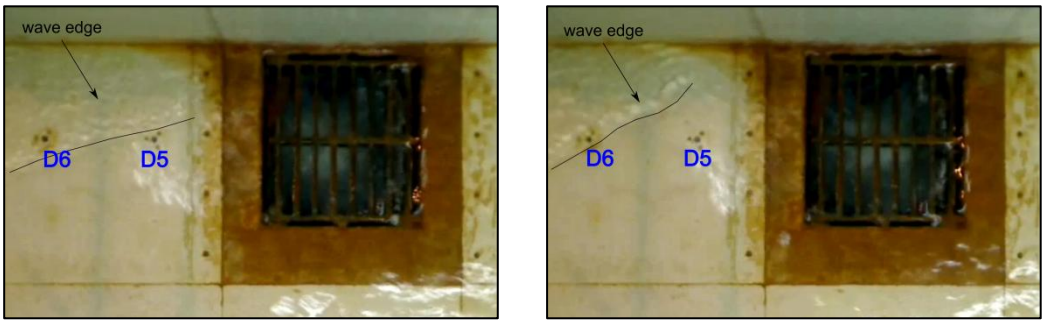

Figure 5.10 – Location of water surface variation from University of Sheffield Laboratory's photo

Figure 5.10 shows the position of the jump in the water surface at different times from the video recording of experimental test. As can be seen on the pictures the position shifting is mainly affecting the water depth at the D5 transducer.

In order to validate the CFD model the result of experimental tests were compared to simulated depth values. An informative way to compare observed and modelled data for six monitoring locations is the so called box-and-whisker plot. The box plot uses a distinct rectangular box for each location, where each box corresponds to the central 50% of the cases, the so called inter-quartile range. The central mark inside the box indicates the median. The median satisfies the same linear property as the mean. Compared to the mean, the median has the advantage of being insensitive to outliers and extreme cases. The boxes are prolonged with lines covering the range of the non-outlier cases (which do not exceed by 1.5 times of the inter-quartile range the above or below box limits). The plot also indicates the extreme cases. This is similarly defined

as the outliers but using a larger inter-quartile range, namely 3 times of the inter-quartile range. If the dataset exhibits outliers and extreme cases then it can be suspected that this is the result of rough measurement errors.

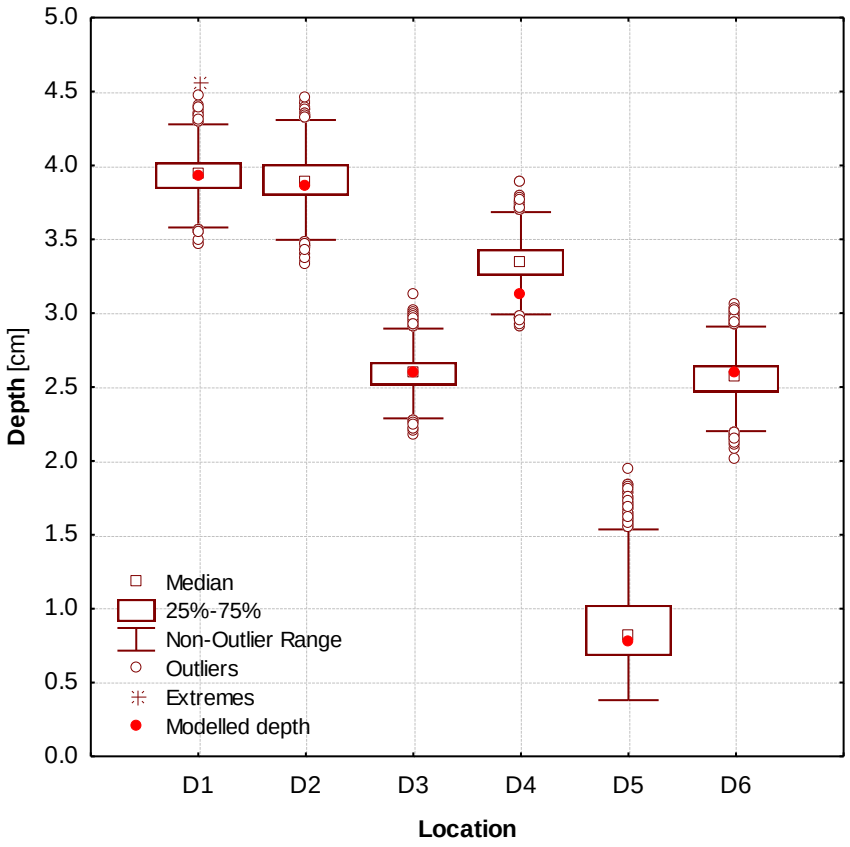

Figure 5.11 – Comparison of observed and modelled depth (intermediate condition, inflow = 26.9 l/s), 2D/3D model

Figure 5.11 shows the box-and-whisker plot for intermediate conditions for 26.9 l/s inflow rate. The modelled depth matches well the observed depth at almost all locations. The only exception is at D4, where the difference between the median of observed depth and the modelled one is 0.22 cm. However this is still within the generally excepted error range in numerical modelling.

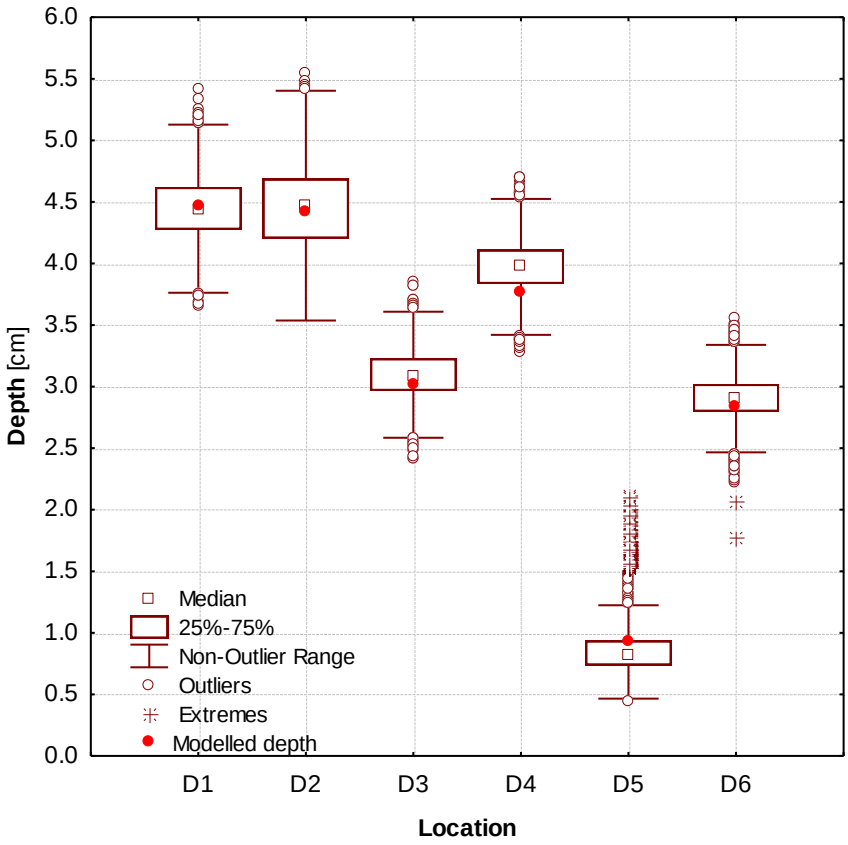

Figure 5.12 – Comparison of observed and modelled depth (intermediate condition, inflow = 36.71 l/s), 2D/3D model

Figure 5.12 shows the comparison of observed and modelled depth for the highest tested inflow. The modelled depth values are very close to the observed ones. The tendency is similar to the previously discussed scenario. The inter-quartile range is significantly wider for almost all locations. It can be explained by the disturbance of inflow. It was discovered through experimentation that for high flows, which are pushing the envelope of the rig setup, the inflow became highly turbulent (see Figure 5.13). The turbulent, wavy water is travelling in the downstream direction and introducing an undesirable variance in water level. Another conspicuous feature is that the number of extremes is strikingly high at the D5 location. This is probably due to the superposition of the above

mentioned hydraulic features, namely the tail water effect and highly turbulent inflow.

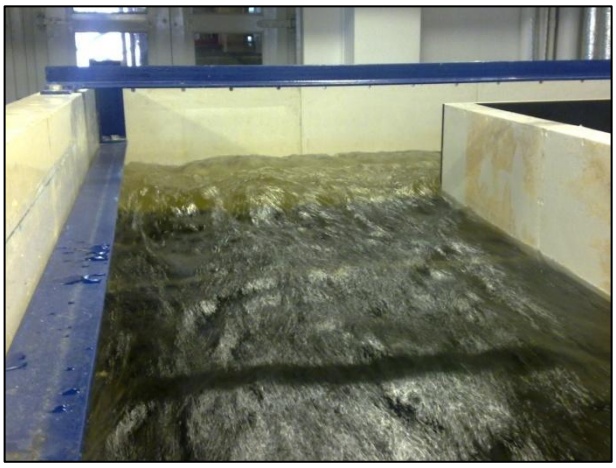

Figure 5.13 – Highly turbulent inflow

As the flow rate decreases below a certain level, this unsettling effect disappears. Table 5.2 shows the numerical comparison of simulated and observed depth at six monitoring locations.

Table 5.2 – Results of model validation, 2D/3D model

	Depth at location [cm]					
	D1	**D2**	**D3**	**D4**	**D5**	**D6**
	Intermediate conditions, inflow=36.71 l/s					
Modelled	4.46	4.42	3.02	3.76	0.93	2.84
Observed	4.44	4.46	3.08	3.98	0.82	2.90
Difference	+0.02	-0.04	-0.06	-0.22	+0.11	-0.06
	Intermediate conditions, inflow=26.9 l/s					
Modelled	3.93	3.86	2.59	3.12	0.77	2.59
Observed	3.94	3.89	2.59	3.34	0.80	2.56
Difference	-0.01	-0.03	0.00	-0.22	-0.03	-0.03
	Intermediate conditions, inflow=6.0 l/s					
Modelled	1.79	1.58	1.26	1.56	1.06	1.28
Observed	1.79	1.60	1.26	1.67	1.05	1.26
Difference	0.00	-0.02	0.00	-0.11	+0.01	+0.02

Considering the differences between observed and modelled depth and the experimental conditions, it can be stated that the flow depth was predicted satisfactorally by the model. Figure 5.14 - Figure 5.18 show the comparison of observed and modelled depth for full 3D and 2D/3D model for different inflow rates.

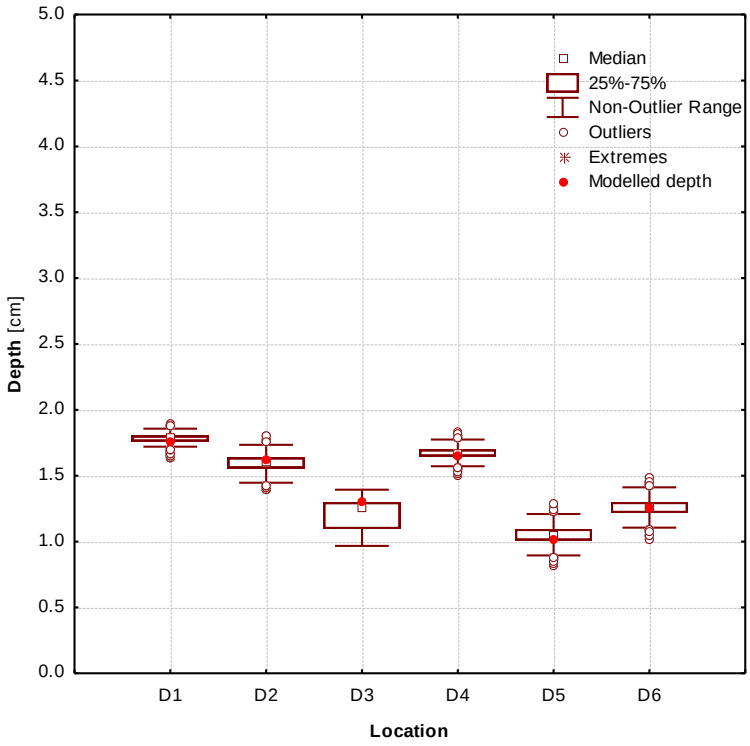

Figure 5.14 – Comparison of observed and modelled depth (intermediate condition, inflow = 6 l/s), full 3D model

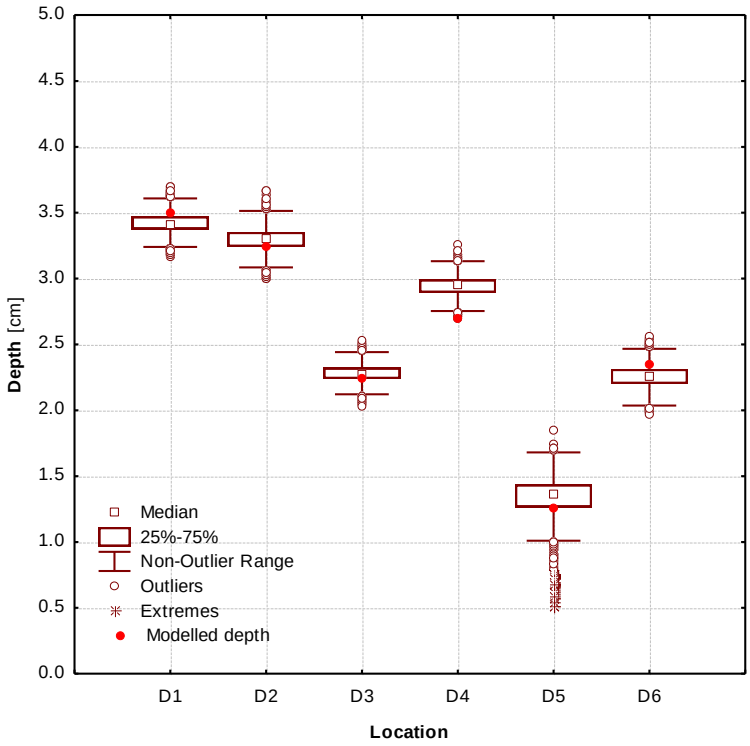

Figure 5.15 – Comparison of observed and modelled depth (intermediate condition, inflow = 19.9 l/s), full 3D model

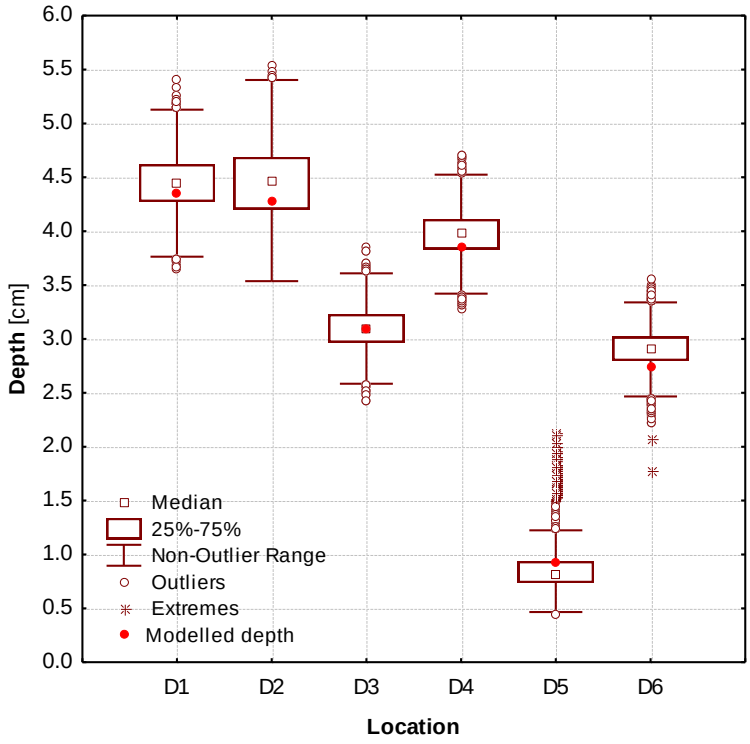

Figure 5.16 – Comparison of observed and modelled depth (intermediate condition, inflow = 36.71 l/s), full 3D model

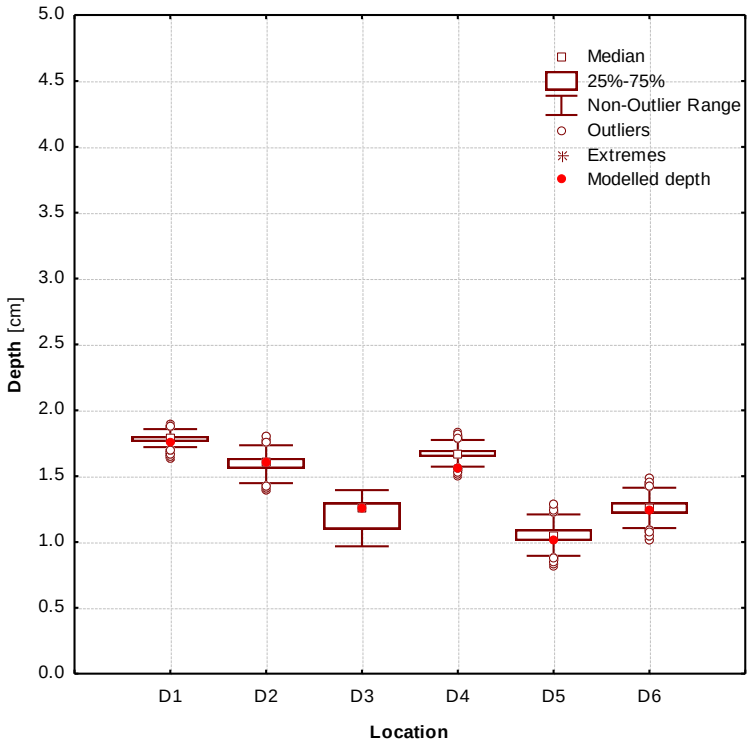

Figure 5.17 – Comparison of observed and modelled depth (intermediate condition, inflow = 6 l/s), 2D/3D model

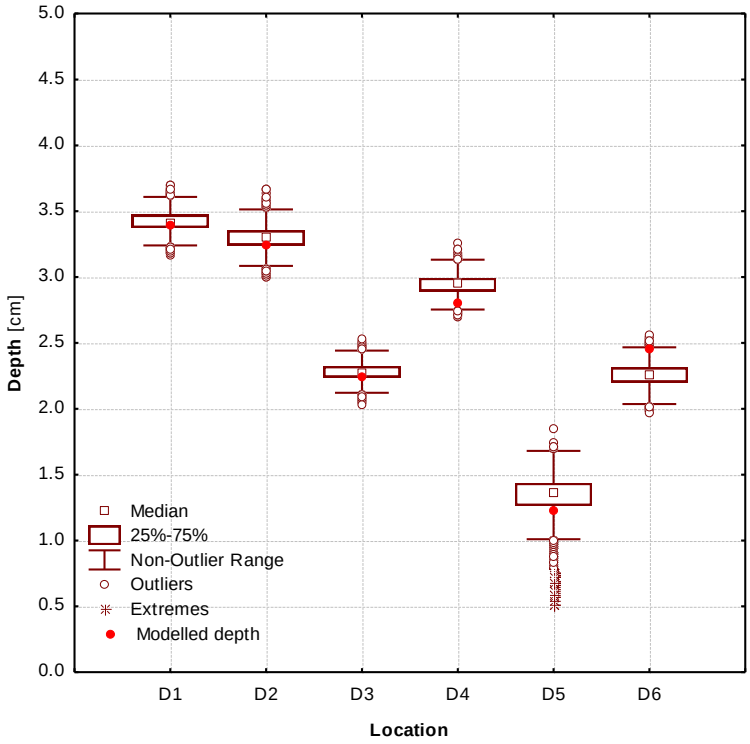

Figure 5.18 – Comparison of observed and modelled depth (intermediate condition, inflow = 19.9 l/s), 2D/3D model

5.1.2 Surcharged gully

According to EN 752 “flooding” describes a “condition where wastewater and/or surface water escapes from or cannot enter a drain or sewer system and either remains on the surface or enters buildings”. The term “surcharge” is defined as a “condition in which wastewater and/or surface water is held under pressure within a gravity drain or sewer systems, but does not escape to the surface to cause flooding”. Eventually surcharge conditions may lead to a rise of water level above the surface. In this case the water escapes from the drain system or prevents surface water from entering into the drain system (Schmitt, et al., 2004). The surcharging condition has occurred more frequently in the last decade causing severe disruption of urban transport. However, to the author's knowledge no studies have been carried out to quantify this effect.

The details of surcharging conditions were discussed in Chapter 3. Figure 3.9 shows the schematic of surcharged system. The validation started with visual comparison of water surface obtained from physical experiment and CFD modelling. Figure 5.19 shows the modelled and observed surcharging water levels. The visual comparison of water surface features is challenging due to the transparency of the water. However it can be stated that the modelled water surface is similar to the observed one.

Figure 5.19 – Visual comparison of simulated and observed water surface features, surcharged conditions, flow rate = 13.89 l/s

The visual comparison has been followed by numerical evaluation of simulated water depths. Figure 5.20 shows the comparison of observed and modelled depth for surcharged condition. The D7 monitoring location represents the transducer at the bottom of the gully pot, measuring the water level above the grate surface. As it was expected from the visualization of CFD results the non-outlier range of measured depth is very wide. This is caused by the highly turbulent conditions around the gully inlet. The CFD model simulation shows that a steady water surface above the grate cannot be achieved even at low flow conditions. The water depth above the grate obtained from physical experiment represents a flat water surface above the grate. In contrast, the result of the CFD simulation is a wavy water surface at γ=0.5. Therefore the modelled surface needs to be converted to an average water surface which can be compared to the observed elevation. Figure 5.13 shows that CFD model is satisfactorally able to predict the water depth above the grate despite its

uneven surface. The simulated depths at D1, D2, D5 and D6 are also very close to the observed ones.

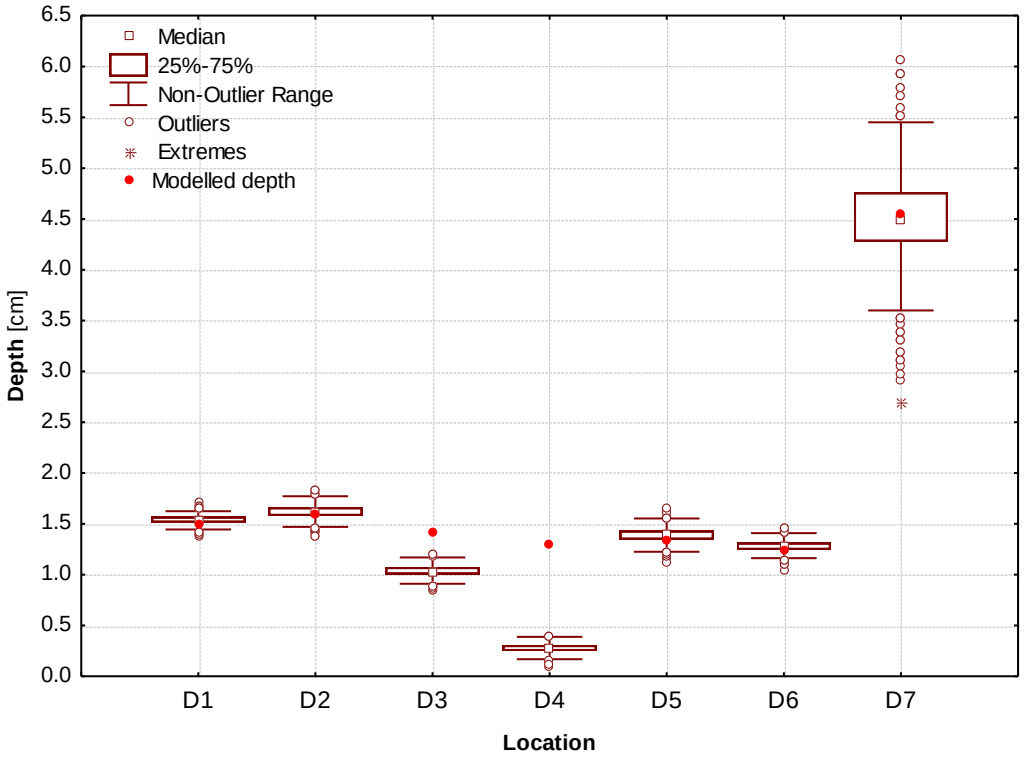

Figure 5.20 – Comparison of observed and modelled depth (surcharge condition, inflow=13.89 l/s)

The difference between modelled and observed depth is 0.02 cm - 0.07 cm. These points are part of a long section 30 cm from the kerb. The water surface is more tranquil at these locations compared to that above the grate. The water depth at D3 and D4 is overestimated by the model (+0.48 cm and +1.02 cm). In contrast to the physical experiment the CFD model is spreading the water more evenly around the inlet. The observed depth is suspiciously low at D4; however detailed investigation has not been undertaken to reveal the possible cause of this anomaly.

Overall, the validation of CFD model against surcharge condition was successful. The agreement with the depth obtained from the experimental test can be considered satisfactory.

5.2 CFD model application for flow into and from gully

The numerical simulations were performed using OpenFOAM (Open Field Operation And Manipulation), a free-source CFD-toolbox produced by OpenCFD Ltd. The software is based on the finite volume numerical method with the co-located variable arrangement for solving system of transient transport equations on arbitrary unstructured meshes in three dimensional space. It is consists a number of precompiled library and solvers, accompanied by the corresponding codes written in C++ programming language in an object-oriented manner suitable for solving problems in Computational Continuum Mechanics. Using the object oriented programming approach creation of data types closely mimicking those of mathematical field theory is enabled, and the feature of overloading in C++ allows mathematical symbols to be applied on scalar, vector and tensor fields very similar to those in ordinary mathematics. It is utilized by the OpenFOAM programming language which is generic, making extensive use of C++ class and function templates and the principle of class inheritance (Weller, et al., 1998)

The validated model is used to investigate several parameters which are affecting the inlet efficiency. The testing protocol established the following conditions:

- Total discharge approaching to inlet: 6.0 l/s - 46 l/s;

- Surcharging discharge: 18 l/s - 88 l/s;
- Longitudinal slope: flat and 1:100, 1:200;
- Cross-slope: flat and 1:20, 1:60, 1:200;
- Gratings: Waterflow "S" (Figure 5.21), Watershed "S" (Figure 5.22) and Briflo (Figure 5.23).

Unsteady simulations with a fixed inflow boundary were run until the water level and velocity magnitude field were found to be practically invariant at the monitoring locations. Typically 30000-50000 iterations were needed to achieve fully converged solutions. The full 3D simulations employing hybrid meshes with 1.6 million cells were run on 4 processors. The average time to get a solution starting from scratch was about 3-5 days. The nested 3D/2D simulations employing a hybrid mesh on the 3D domain with 0.7 million cells and 65000 cells on 2D domain were running on 4 processors (3 cores for 3D domain and 1 core for 2D domain). The average time to get a solution was almost half of the full 3D case. The developed 3D/2D model lived up to expectations, decreased the running time significantly and provided the necessary information with accuracy at the same time.

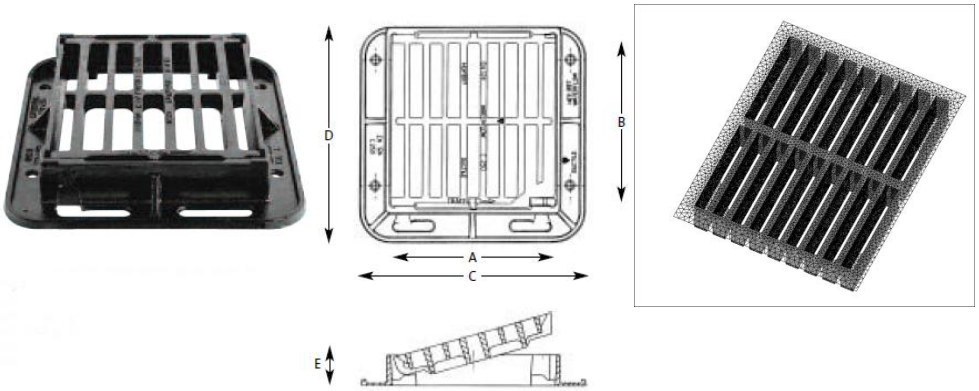

Figure 5.21 – Waterflow "S" grate and its mesh

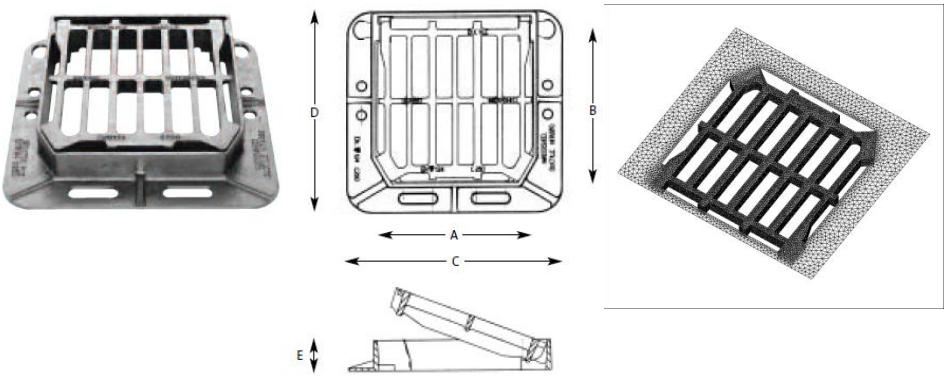

Figure 5.22 – Watershed grate and its mesh

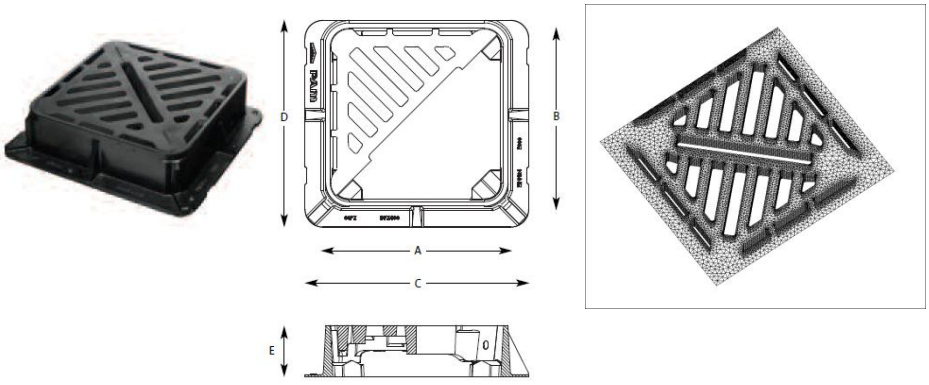

Figure 5.23 – Briflow grate and its mesh

At the initial time, the distribution of phase fraction is prescribed in the cells of the mesh, defining the position and the shape of the interface at the beginning of the calculation. Most of the low flow simulations were started with the domain filled with air only, the high flow runs used the result of the low flow one as an initial condition in order to decrease the running time. Figure 5.24 shows six snapshots of the unsteady flow simulation of intermediate conditions. It can be seen that initially the domain is filled with air, except the gully pot, which is partly filled with water.

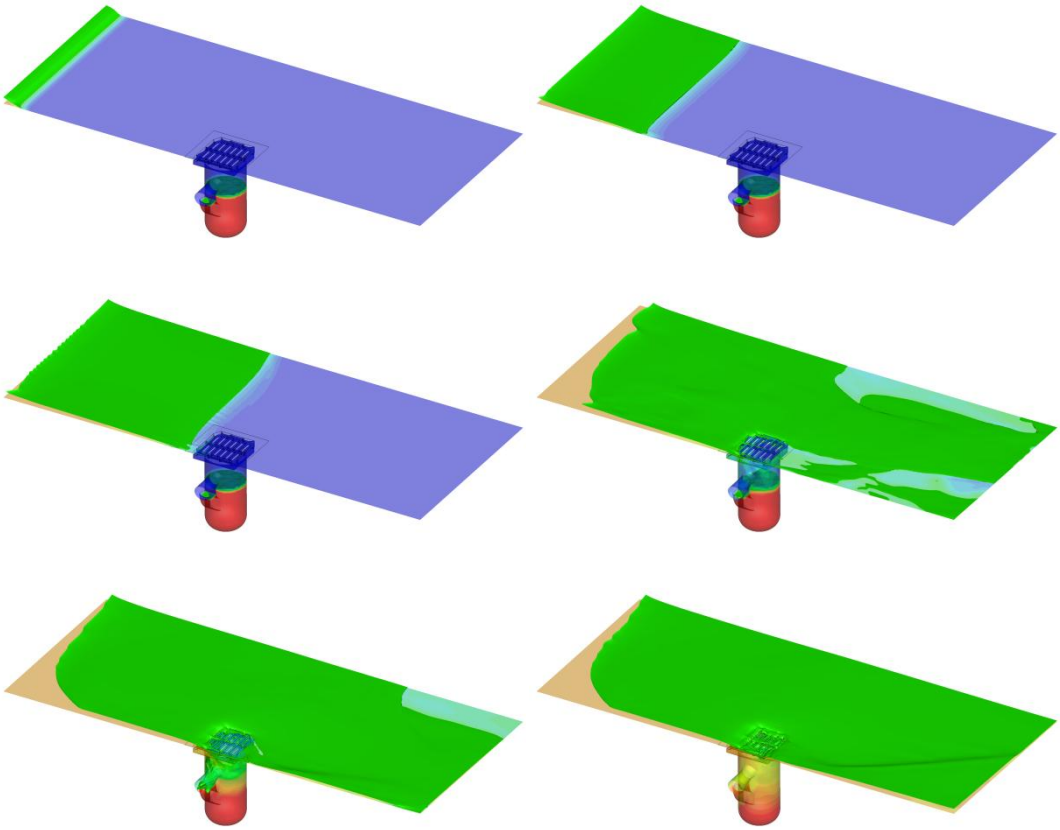

Figure 5.24 – Snapshots of the simulation of intermediate condition (not at same time intervals), full 3D model

The aim of this initial condition for the gully was to reduce the filling time of gully pot hereby decreasing the running time.

The water is entering the plate at the left edge and flowing to right. The front wave remains almost perpendicular to the curb due to the flat long slope and cross slope (first row picture one and picture two, second row picture one). One part of the approaching front is captured by the gully; the other part passes the outside edge of the grating and between the grating and the kerb (second row, second picture). The captured water increases the water level in the gully and starts to flow out through the connected pipe (row three picture one). The last picture shows the final state of the simulation.

5.3 Interception capacity

Inlet interception capacity (Q_i) is the flow intercepted by an inlet under given conditions. The efficiency of an inlet (E) is the percent of total flow that the inlet intercepts for those conditions. The efficiency of an inlet changes with changes in cross slope, longitudinal slope, approaching flow and road roughness. The interception capacity of an inlet increases with increasing flow rates, however the efficiency decreases with increasing flow rates (Brown, et al., 2001). The efficiency is defined by the following equation:

$$E = \frac{Q_i}{Q} \tag{5.1}$$

where E is the inlet efficiency, Q is the approaching flow and Q_i is the intercepted flow. The non intercepted flow is termed bypass flow and defined

$$Q_b = Q - Q_i \tag{5.2}$$

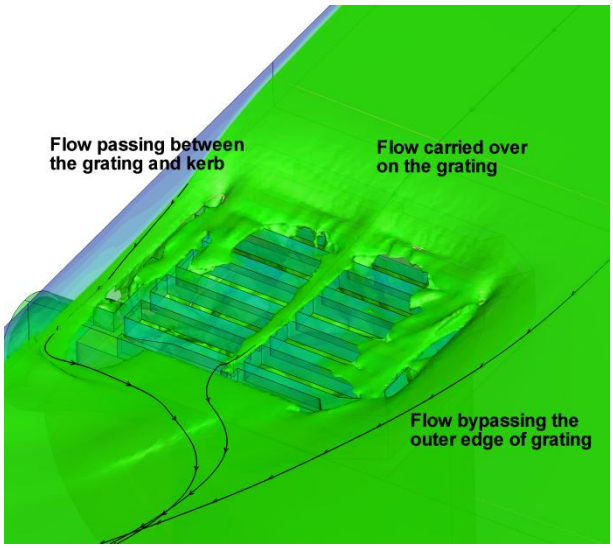

Figure 5.25 – Components of bypassing flow

Figure 5.25 shows the streamlines gained from CFD simulation, which can help to analyse the flow around and over the gratings. For the analysis of gratings, the flow bypassing the grating can be divided into three separate components (see Figure 5.25): (1) the flow passing between the grating and kerb, (2) the flow bypassing the outer edge of the grating and (3) flow carried over on the grating itself. The total flow bypassing the gratings is:

$$Q_b = q_1 + q_2 + q_3 \tag{5.3}$$

where q_1 is the flow passing between the grating and kerb, q_2 is the flow bypassing the outer edge of the grating and q_3 is the flow carried over on the grating itself.

Li (Li, et al., 1951) suggested the following equation to calculate the flow bypassing the outer edge of the grating

$$q_2 = K_1(L' - L)y'\sqrt{gy'} \tag{5.4}$$

where $K_1 = 0.25$, L' is the length of grating required to capture the outer portion of flow, L is the length of grating at outer edge, y' is the depth at the outer edge of grating. L' is given by:

$$\frac{L'}{v_0}\sqrt{\frac{g}{y'}} = K_2 \tan\theta_0 \tag{5.5}$$

$K_2 = 1.2$, $\tan\ \theta_0$ is the cross-slope of road surface, v_0 is the average velocity at the outer edge of grating.

These equations have been compared with CFD modelling results for intermediate conditions. In the case of terminal and surcharging conditions the term bypassing flow is difficult to interpret; therefore the results from these were not included in the investigation. The investigation focussed on the applicability and validity of the above equation. Different sloping conditions and inflows were tested and it was found that the included parameters give sufficient information to calculate the bypassing flow rate at the outer edge of the gully. The evaluation of two constants K_1 and K_2 revealed that neither of them can be considered as constant. The K_1 parameter is a function of cross-slope described by the following equation:

$$K_1 = 1.891\exp\left(0.0067\frac{1}{\tan\theta_0}\right) \tag{5.6}$$

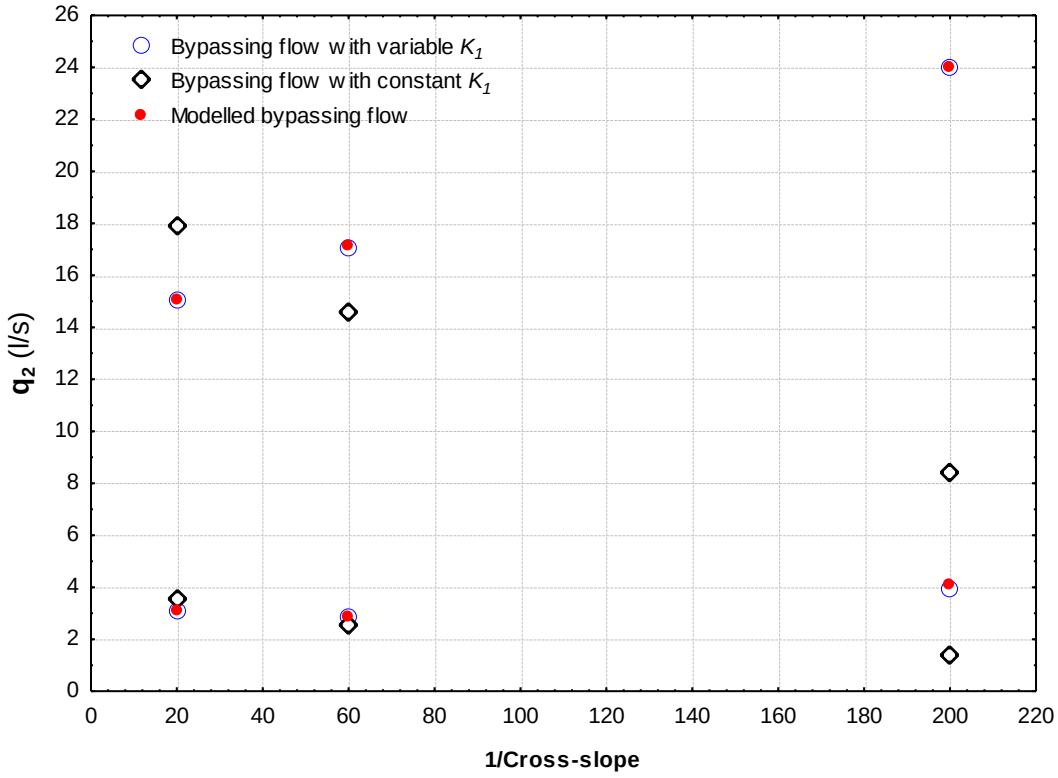

Figure 5.26 – Bypassing flow rate with constant and variable K_1 parameter

Figure 5.26 shows the flow rate calculated by constant K_1 and variable K_1 parameters compared to the observed bypassing flow rate. High and low flow rates combined with deep and low slopes are presented in the graph in order to shows the applicability of variable K_1 on wide range of hydraulic environment. The originally suggested 0.25 value for K_1 does not give a reliable result, especially when the flow rate is high on a low cross-slope (1:200). The original equation gives only 30% of the actual bypassing flow. In contrast, the 0.25 value is working well for low flow and deep cross-slope, the calculated flow rate is very close to the observed one.

The flow travelling over the grating can be calculated by:

$$q_3 = Q_0\left(1 - \frac{L^2}{L_0^2}\right)^2 \tag{5.7}$$

where L_0 is the length required to capture all the flow over it given by:

$$\frac{L_0}{v_0}\sqrt{\frac{g}{y_0}} = K_3 \tag{5.8}$$

The value of K_3 depends on the ratio of opening width to bar width. The constant can have three different values:

- K_3=2 if the width of bar less than the width of opening;
- K_3=4 if the width of bar equal to the width of opening;
- K_3=8 if three transverse bars placed on the grating as well as longitudinal bars.

The equations for flow travelling over the grating was tested using CFD model results and was found to predict the flow rate with ±5% error. Considering that the flow travelling over the bars is very small compared to the bypassing flow this error band is more than acceptable.

Different methods have been used by model developers to calculate the intercepted flow rate. The most commonly used method is the Flow-Head curve, where the flow depth is used to calculate the intercepted flow rate. The location of the depth used in the calculation has a significant importance, however many researchers have applied different locations (above the grating, at the upstream edge, at outer edge, etc.). In this study the depth was measured 0.6 m upstream of the centre of the grating. Figure 5.27, Figure 5.28 and Figure 5.29 show the relationship between flow depth and intercepted flow rate for different gratings.

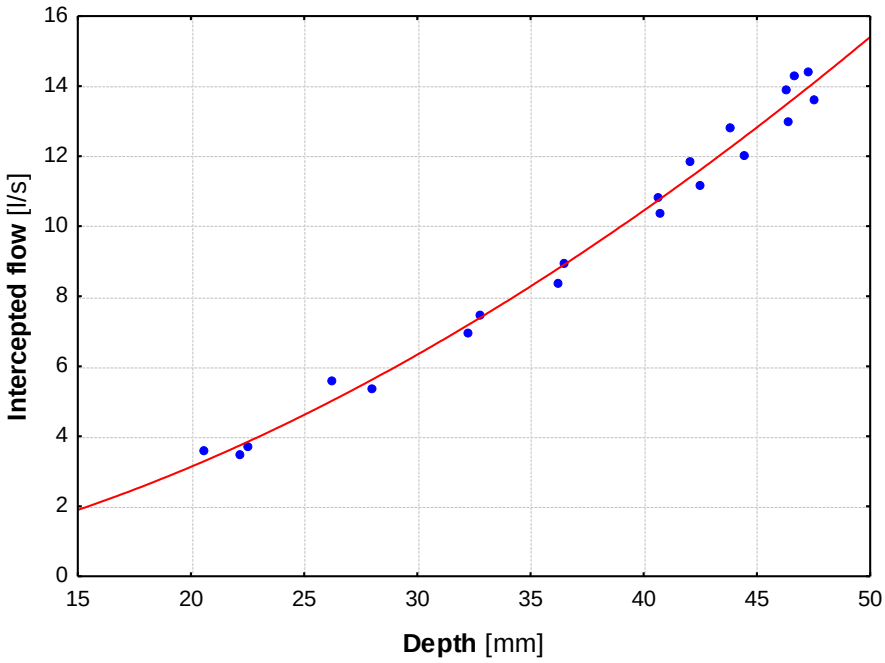

Figure 5.27 – Intercepted flow rate vs. depth Briflow grating

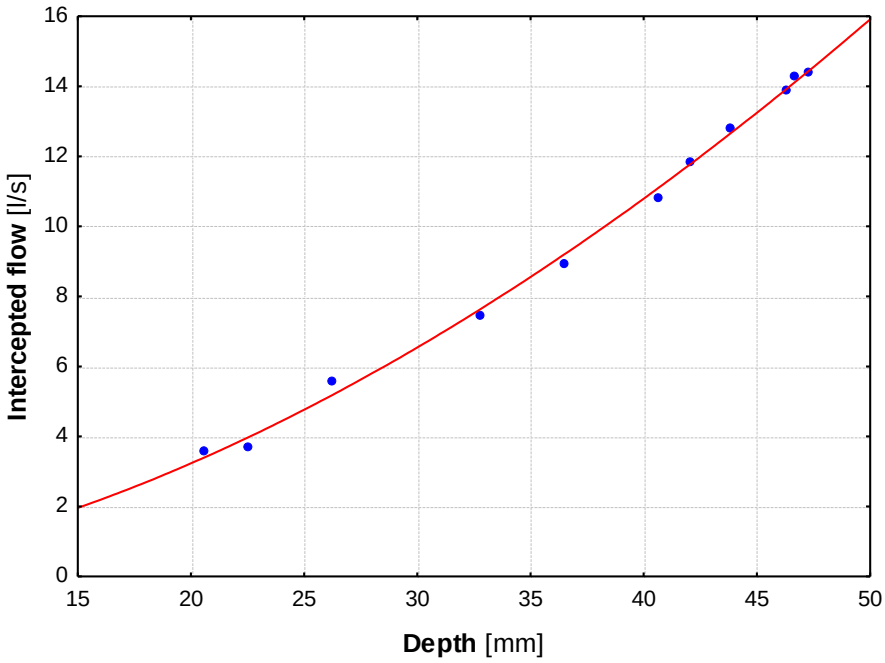

Figure 5.28 – Intercepted flow vs. depth Watershed grating

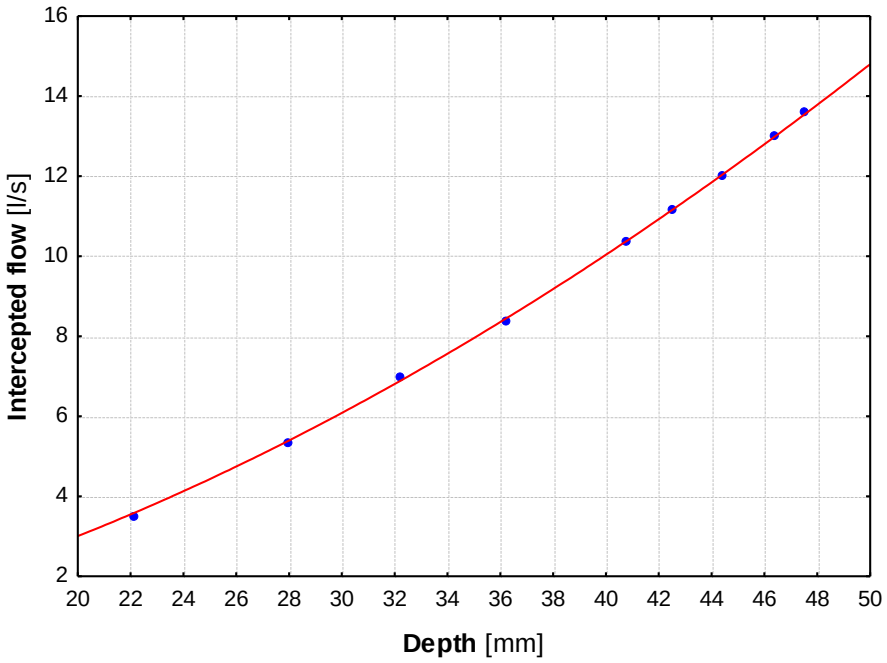

Figure 5.29 – Intercepted flow vs. depth for Waterflow grating

The blue dots are simulated values; the red line represents a power function fitted to simulated values. The function has a form of $Q_i = a*d^b$. The exponent has same value for each functions, however the constant is different for each gratings.

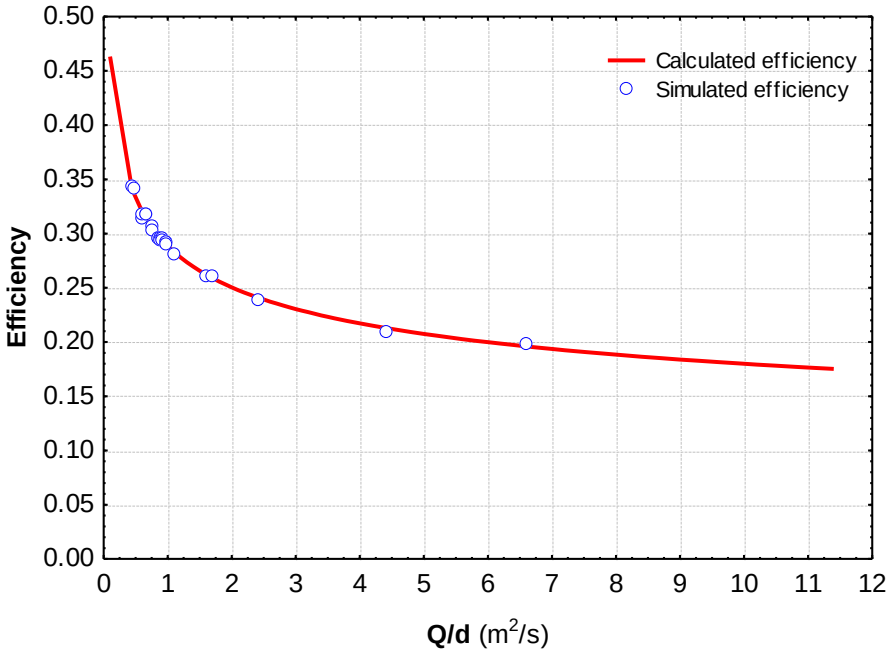

Figure 5.30 – Simulated and calculated efficiency for Waterflow grating

Similarly to the Q-H curve the efficiency is frequently represented in the form of an E-Q/d curve. In this investigation the Q/d parameter showed the best result for all three gratings as well. Spaliviero and May (Spaliviero & May, 1998) also used the Q/d parameter to represent efficiency data and found a linear relationship between these two parameters. In contrast to a linear function of the two variables Gomez and Russo's (Gomez & Russo, 2011) research showed that the relationship is more like a power function rather than linear one. The investigation in this study has produced a similar result and found a strong correlation between simulated data and a power type function (see Figure 5.30):

$$E = A\left(\frac{Q}{d}\right)^{B} \tag{5.9}$$

where Q is the discharge approaching the inlet, d is the depth 0.6 m upstream from grating centre, A and B are empirical coefficients. High correlation coefficients (R^2 is between 0.97 and 0.99) were obtained for all three gratings. The exponent (B) has a value between -0.20 and -0.31, while the constant (A) is between 0.28 and 0.30.

5.3.1 Factors affecting grating efficiency

5.3.1.1 Longitudinal slope and cross-fall

Increasing the longitudinal slope causes an increase in flow velocity. The increased velocity results in less time for the water to enter the grating and increases the amount of splashing over water. As the non-intercepted flow increases the efficiency of the grating decreases.

Increasing the cross-fall, at a given long slope, results in an increase in water depth of the approaching water due to the decreased flow width. Changing the cross-fall also results in a change in flow pattern or streamlines. Figure 5.31 shows the effect of a change in cross-fall to the flow pattern.

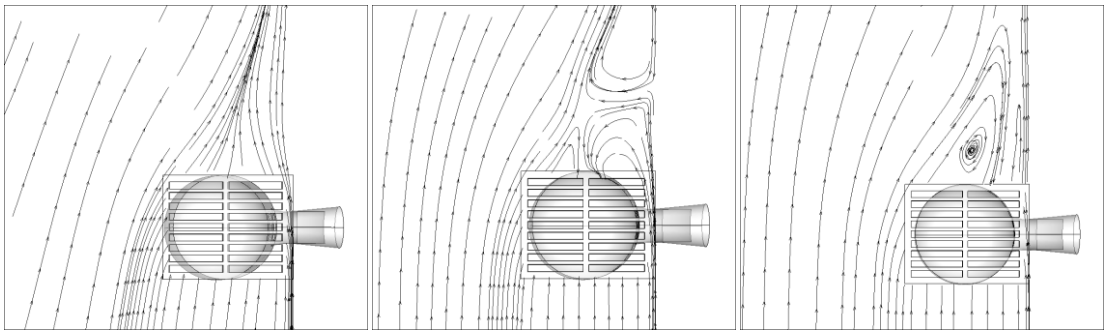

(a) (b) (c)

Figure 5.31 – Flow pattern at different cross-falls: (a) 1:20, (b) 1:60 and (c) 1:200

It can be seen as that the cross-fall increases the streamlines are closer to the kerb. In the case of steep cross-fall (Figure 5.31a) the intercepted flow is arriving from the upstream edge and outer edge of grating. As the cross-fall decreases the interception role of the downstream edge of the grating increases (Figure 5.31b and Figure 5.31c). The cross-fall is proportional to the amount of bypassing flow and it follows that the amount of back flow is inversely proportional to cross-fall.

The distribution of intercepted flow among the edges of the grating is less known. The existing knowledge is mostly theoretical, experimental investigation has not been done yet, although it could be useful in the design and optimization of grating. One of the most comprehensive investigations (NEENAH & Engineering, 1987) on the hydraulic characteristics of inlet grates

conducted by the NEENAH Foundry Company and Engineering Laboratory Design stated: "Minor addition to the grate flow will occur due to inflow from the side of the grate. No attempt was made to include a factor measuring side flow since this would unnecessarily complicate the equation." Despite the fact that the side flow was not measured directly during the experiment this statement has been accepted and applied by engineers and researchers.

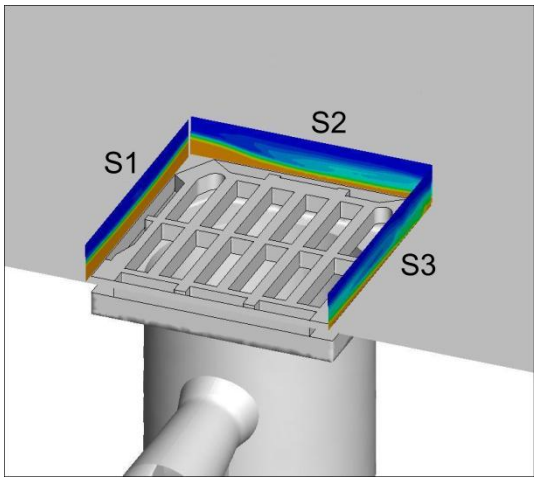

Figure 5.32 – Notation for investigation the effect of cross-fall on intercepted flow

Nowadays, with the help of CFD modelling the distribution of intercepted flow among the edges of the grating can be calculated. Figure 5.32 shows the notation used in this investigation: Section1 (S1) is the upstream edge of the inlet, Section2 (S2) is the outer edge of the inlet and Section3 (S3) is the downstream edge of the inlet. Figure 5.33 shows the distribution of intercepted flow for 1:20, 1:60 and 1:200 cross-fall with 1:200 longitudinal slope. If the cross-fall is low (first graph of Figure 5.33) the dominant section is S1, the upstream

section of the grating. 80% of the intercepted flow is coming from the upstream edge, 18% from outer edge and 2% from the downstream edge.

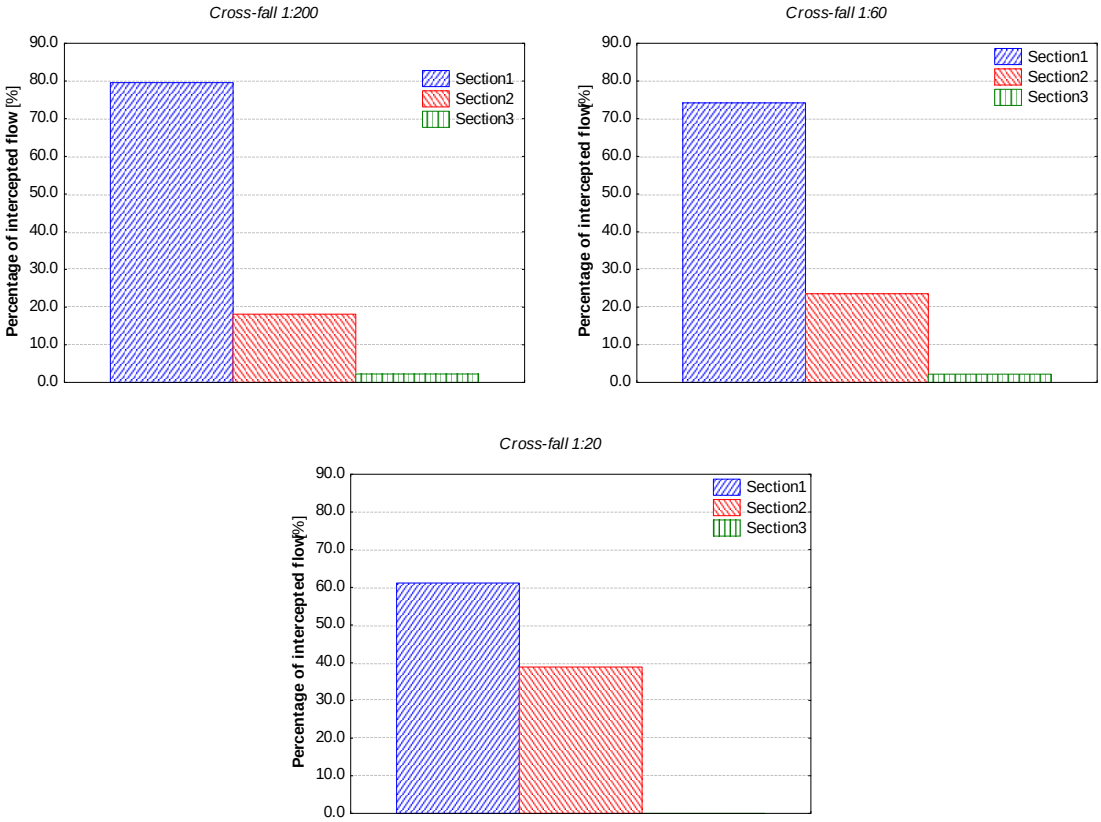

Figure 5.33 – Distribution of intercepted flow with different cross-falls

If the cross-fall is medium (second graph of Figure 5.33) the distribution is similar to the low cross-fall. The contribution from the upstream edge is more than 70%. The flow crossing the outer edge is increased by 4-5%, exactly the same amount as the decline at upstream edge. The downstream edge remained the same with 2%. If the cross-fall is steep (third graph of Figure 5.33) the distribution significantly changes. The back flow from the downstream edge has disappeared due to the increased bypassing flow rate. The contribution from the

outer edge also significantly changed; approximately 40% of the intercepted flow is coming from the outer edge. This confirms the hypothesis that inflow from the side of the grating is not negligible.

Figure 5.34 shows the flow distribution of intercepted flow for the three edges of the grating. It can be seen that the amount of flow coming from the outer edge of the grating is proportional to the cross-fall. Despite this proportional relationship most of the flow is coming from the upstream edge. The flow coming from the downstream edge is negligible, only 2% of the total intercepted flow.

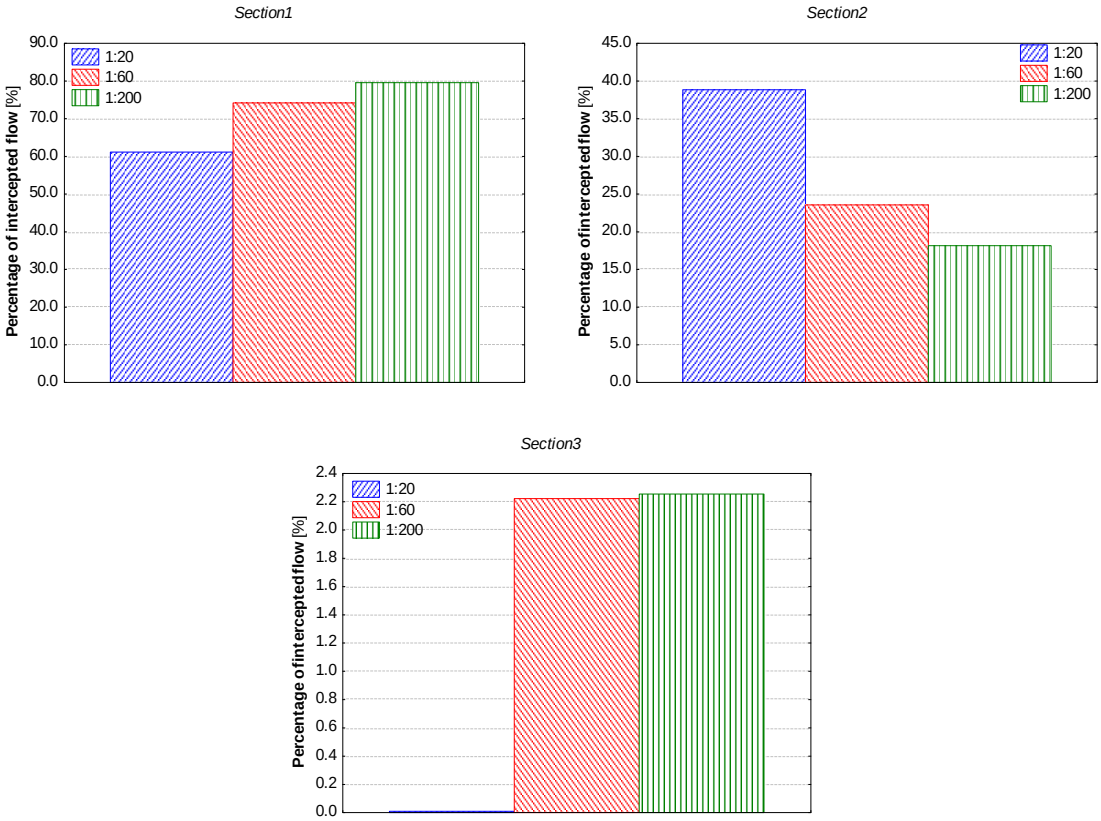

Figure 5.34 – Percentage of intercepted flow for the three edges of inlet

5.3.1.2 Waterway area

The waterway area is an important characteristic of the grating. The gratings selected for simulation have very similar waterway areas (933 cm^2, 940 cm^2 and 880 cm^2) although with different patterns, internal length, bar width and bar spacing. Figure 5.35 shows the intercepted flow against total flow for four different gratings with 1:200 longitudinal slope and cross-fall. It can be seen that the "Watershed" grating is the most efficient among the tested gratings, despite the fact it has the second largest waterway area. The "Waterflow A" grating has the largest area with transversal bars. The main difference between "Waterflow A" and "Watershed" is the bar width and bar pattern. The "Watershed" grating has a longer internal length due to the bar pattern and bar width. The situation is similar to the case of the "Briflow" and "Waterflow B" gratings. The longer internal grating length is results in greater efficiency, because the flow passing over the grating has a longer edge to fall in.

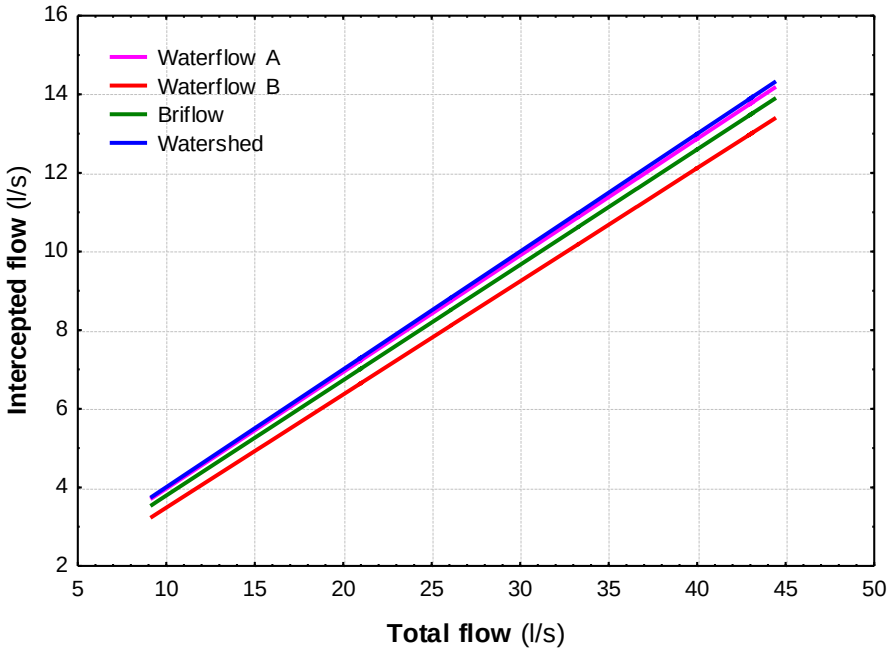

Figure 5.35 – Total flow vs. intercepted flow for different gratings

5.4 Surcharging conditions

Regarding the distinct stages and processes for the case of a surcharged drain system the urban flooding simulation models are required to accurately describe the hydraulic phenomena of a surcharged gully, particularly:

- the transition from free surface flow to pressurized flow
- the interaction between surface flow and pressurized flow
- the rise of the water level above surface level

Numerous experiments have been undertaken worldwide in connection with grate efficiency. All the experiments related to gratings/gullies are based on the most frequent situation, when the flow direction is from the surface into the gully. In this study surcharging conditions have also been investigated. This type of flow condition is getting more attention nowadays from numerical modellers; however it has not been studied experimentally before.

Figure 5.36 shows fifteen snapshots of the unsteady flow simulation following sudden short-lived surcharging of the gully. The extent of the road surface and the height of the cube are only a cropped portion of the computational domain that extends further through the top and the three sides. The cube selected here is just for the presentation of results. It can be seen that the simulation starts with an empty domain. Initially the gully is empty and the road surface is dry.

Once the water starts entering the gully from the pipe connection underneath (first row, second image), the water leaves the gully through the inlet grating in a fashion that reflects the water pressure distribution within the gully.

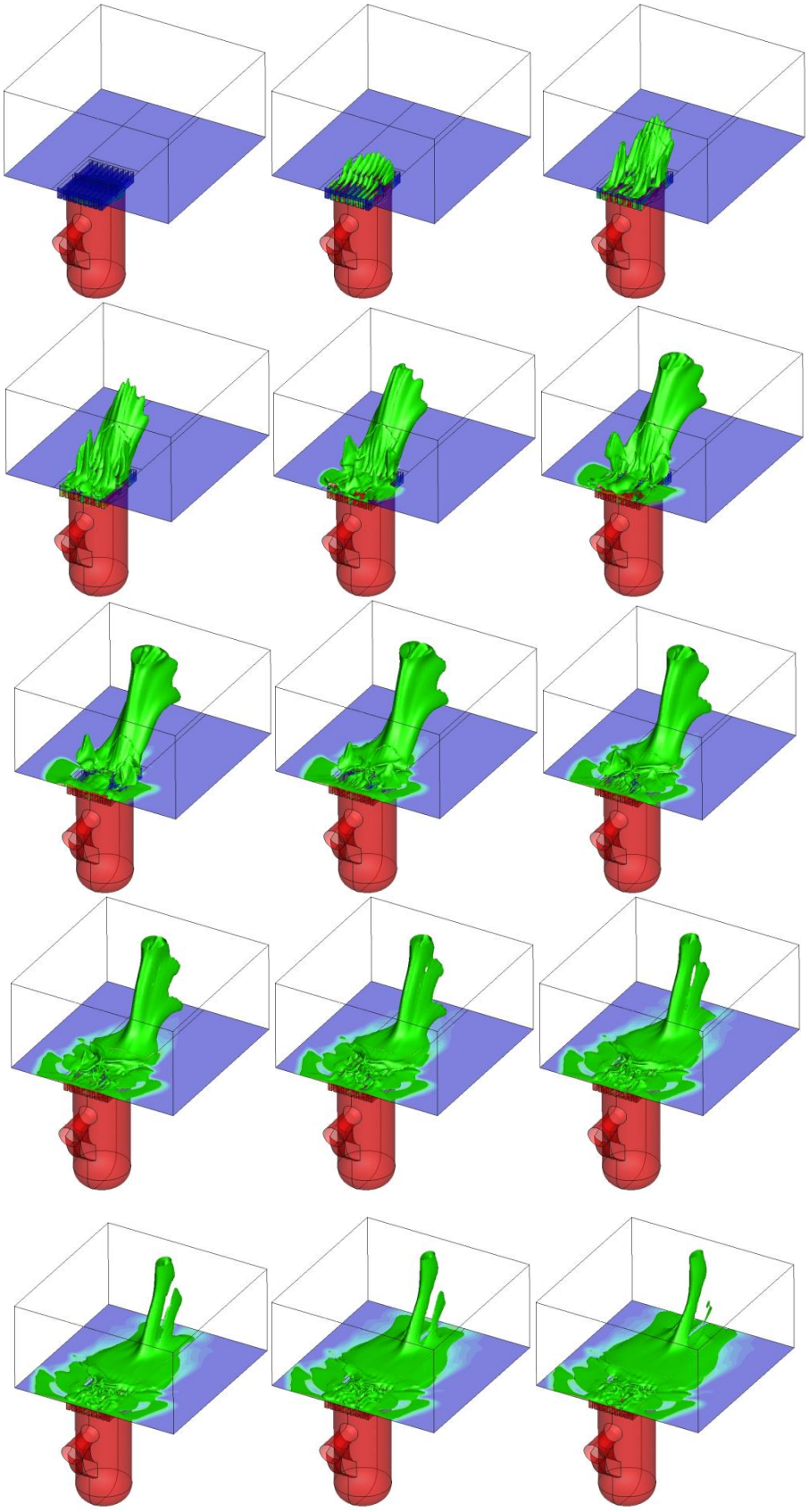

Figure 5.36 – Snapshots of sudden surcharging gully (snapshot in every 0.2s)

The position of the leaving water strongly depends on the direction of the rodding eye, which in this case is not horizontal (see Figure 3.3).

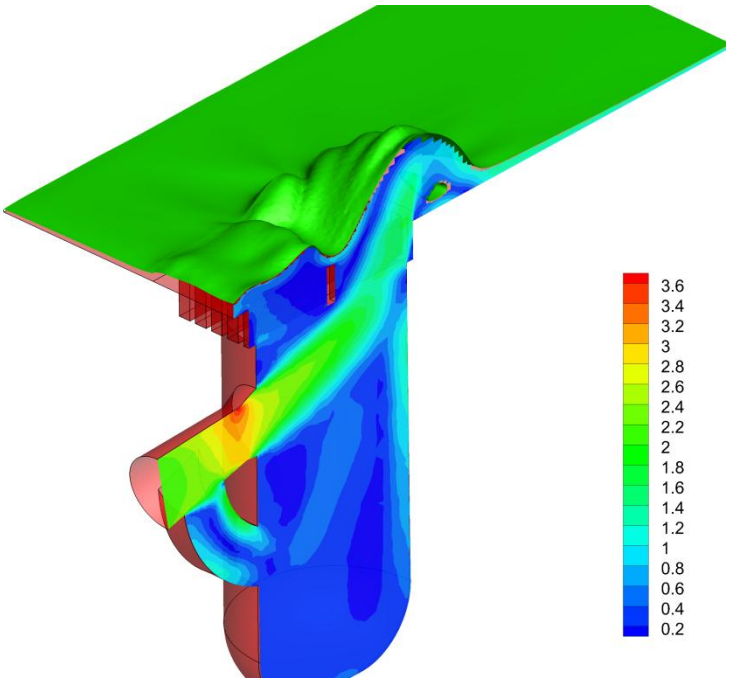

Figure 5.37 – Velocity distribution in surcharging gully, surcharge flow = 35.25 l/s

Figure 5.37 shows the water surface and the velocity distribution for a surcharged gully. It can be seen that the direction of the main stream is along the centre line of the rodding eye. The outer edge is on the opposite side to the inflow location; therefore most of the flow (approximately 70%) is leaving the gully through this edge. If the centre line of the rodding eye is perpendicular to the centre line of the gully pot, then the water hits the opposite wall of the gully pot which absorbs its energy resulting in the leaving water being almost evenly distributed among the upstream, downstream and outer edge.

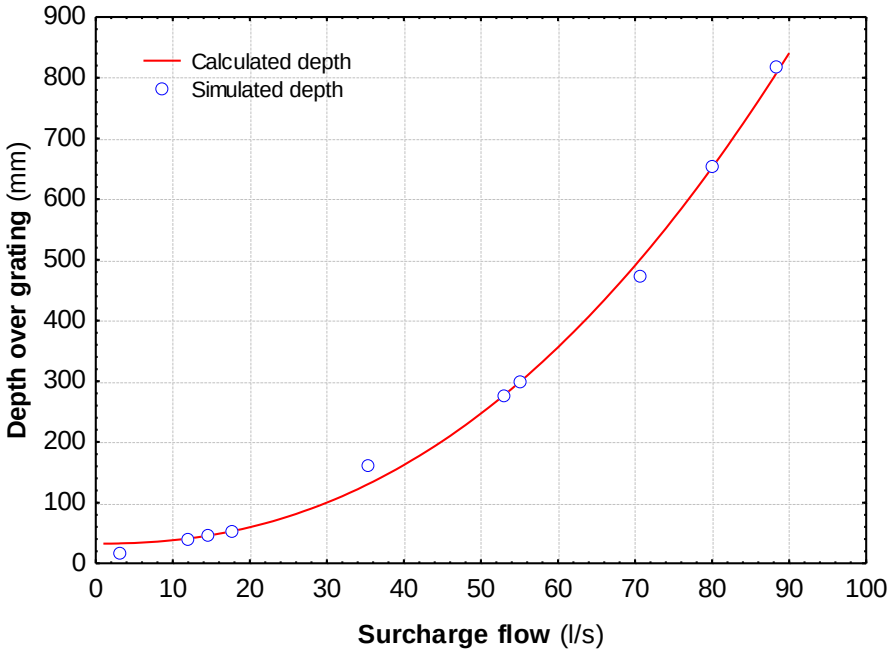

Figure 5.38 – Surcharge flow vs. depth over grating

There is a strong power function type relationship between surcharging flow rate and depth over the grating (see Figure 5.38). When the gully is surcharged head losses are based on the full gully pot area and wetted perimeter, because these characteristics are all functions of the section shape and size.

Whilst the movement of the fountain leaving the grating is rapid, the spreading of water on the surface is relatively slow. The water volume on the surface remains more or less symmetrical throughout the part of the simulation that is presented. Drying and wetting of the surface progresses as the water moves on the surface.

5.5 Discharge coefficient calculation

Many researchers have conducted tests on existing residential street inlets (Kranc & Anderson, 1993), (Larson, 1947), (Li, et al., 1951), (Li, et al., 1954),

(McEnroe, et al., 1999), (Valentin & Russo, 2007). Their results are not generally applicable unless similar conditions are applied. Even interpolation of the existing results is believed to be difficult.

Flow over the grate represents a typical example of spatially varied flow with decreasing discharge. Several authors have proposed equations for spatially varied flow profiles relating the intercepted flow to the specific energy or flow depth (Mostkow, 1957), (Noseda, 1956), (Subramanya & Senputa, 1981). These studies considered only the frontal flow for the calculation of discharge coefficient.

The inlet may operate like a weir when the water depth is shallow, or like an orifice when it is submerged (Guo, 1997), (Guo, 2000a), (Guo, 2000b), (Guo, 2000c), (Mays, 2001). For a grate inlet that operates as a weir, the intercepted flow is given by the following equation:

$$Q_i = \int_0^Q dQ = b\sqrt{2g}\int_0^{h_0}\left(h + \frac{v_1^2}{2g}\right)^{\frac{1}{2}} dh = b\sqrt{2g}\,\frac{1}{1.5}\left[\left(h + \frac{v_1^2}{2g}\right)^{\frac{3}{2}}\right]_0^{h_0} \tag{5.10}$$

$$Q_i = \frac{2}{3}\sqrt{2g}b\left[\left(h_0 + \frac{v_1^2}{2g}\right)^{3/2} - \left(\frac{v_1^2}{2g}\right)^{3/2}\right] \tag{5.11}$$

Introducing the discharge coefficient to incorporate the local losses:

$$Q_i = \frac{2}{3}C_{d1}\sqrt{2g}b\left[\left(h_0 + \frac{v_1^2}{2g}\right)^{3/2} - \left(\frac{v_1^2}{2g}\right)^{3/2}\right] \tag{5.12}$$

In case of small velocity the $-\left(\frac{v_1^2}{2g}\right)^{3/2}$ term is negligible or can be included in the discharge coefficient, therefore:

$$Q_i = C_{d1} \frac{2}{3} \sqrt{2g} b H_1^{3/2} \tag{5.13}$$

where Q_i is the discharge intercepted by the inlet, C_{d1}, is the weir discharge coefficient, which has a value between 0.6 - 0.7 (Butler & Davies, 2004), b is the length of the inlet and H_1 is the total head of water over the inlet. The key issue is the location where H_1 is measured (McEnroe, et al., 1999). The location of the critical-flow section depends on the geometry of the surrounding area of the inlet opening. Critical-flow does not necessarily occur at the perimeter of the inlet opening. In some cases, the exact location H_1 is uncertain and must be estimated.

Rehbock found experimentally that:

$$C_{d1} = 0.611 + 0.08 \frac{H}{W} + \frac{1}{305H} \tag{5.14}$$

The above equation neglects the viscous and surface tension effects, therefore is only valid when the total head is not small. Based on Rehbock's research many investigators have confirmed the value of 0.611. Most design procedures assume a constant value for the discharge coefficient regardless of the characteristics of the flow. Experience has shown that the discharge coefficient is unlikely to be invariant at all flow rates. Preliminary investigation shows that in contrast a variable discharge coefficient can help to establish better design criteria for gully inlets (Galambos, et al., 2009).

The intercepted discharge can be calculated using the kinetic energy coefficient (α), momentum coefficient (β) and the energy loss between the two sections (h_L):

$$Q_i = A_2\sqrt{\frac{2g(\beta_1 h_1 - \beta_2 h_2 - h_L)}{\alpha_2 - \alpha_1(A_2 / A_1)^2}} \tag{5.15}$$

Using (5.11) and (5.15):

$$Q = \frac{2}{3}C_{d1}\sqrt{2g}b\left[\left(h_0 + \frac{v_1^2}{2g}\right)^{3/2} - \left(\frac{v_1^2}{2g}\right)^{3/2}\right] = A_2\sqrt{\frac{2g(\beta_1 h_1 - \beta_2 h_2 - h_L}{\alpha_2 - \alpha_1(A_2 / A_1)^2}} \tag{5.16}$$

A rearrangement yields:

$$C_{d1} = \frac{3}{2}\frac{A_2\sqrt{\frac{(\beta_1 h_1 - \beta_2 h_2 - h_L}{\alpha_2 - \alpha_1(A_2 / A_1)^2}}}{b\left[\left(h_0 + \frac{v_1^2}{2g}\right)^{3/2} - \left(\frac{v_1^2}{2g}\right)^{3/2}\right]} \tag{5.17}$$

where,

$$\alpha = \frac{\int_0^A v^3 dA}{\bar{V}^3 A} \approx \frac{\sum_{i=1}^{N} v_i^3 dA}{\bar{V}^3 A} \tag{5.18}$$

and

$$\beta = \frac{\int_0^A v^2 dA}{\bar{V}^2 A} \approx \frac{\sum_{i=1}^{N} v_i^2 dA}{\bar{V}^2 A} \tag{5.19}$$

Kinetic energy and momentum principles are often used in hydraulic problems. Generally, in the energy and momentum equations the velocity is assumed to be steady, uniform and non-varying vertically. This assumption does not introduce any error in the case of steady flows. However the boundary resistance modifies the velocity distribution. When the velocity varies across the section true mean velocity head need not necessarily equal $\frac{\overline{v}^2}{2g}$, therefore a correction factor is required to be used for both energy and momentum calculations. For

approximate values of coefficients, Rehbock assumed a linear velocity distribution, while Chow used a logarithmical one. King and Brater (King & Brater, 1963) provide experimentally determined values for kinetic energy and momentum correction coefficients for open channels of various cross-sectional shapes. In practice, the velocity distribution coefficients have often been assumed to be unity and the flow equations solved in an approximate way (Chen, 1992). In reality the velocity distribution is not uniform over the cross-section and hence the velocity and momentum coefficient is not equal to unity.

Different theoretical expression for α and β have been derived by many authors. In this study the values of α and β were determined by a numerical integration method using the CFD calculated velocity distributions according to equations (5.18) and (5.19). α and β have been calculated at the above mentioned three locations.

$$\alpha = A_\alpha + B_\alpha * S_T + C_\alpha * Q_u + D_\alpha * \mathrm{Re} \tag{5.20}$$

$$\beta = A_\beta + B_\beta * S_T + C_\beta * Q_u + D_\beta * \mathrm{Re} \tag{5.21}$$

where $A_\alpha, A_\beta, B_\alpha, B_\beta, C_\alpha, C_\beta, D_\alpha, D_\beta$ are regression parameters, S_T is cross-slope, Q_u is approaching surface flow and Re is Reynolds number.

Both the individual sections and averaged values (for three section S1, S2 and S3 see Figure 5.32) were investigated. Figure 5.39 and Figure 5.40 show the comparison of simulated and calculated α for the upstream and outer edge sections. It can be seen that the calculation predicts the kinetic energy coefficient for these two sections very well. This is also supported by the

regression statistics for calculation of kinetic energy and momentum coefficients (Table 5.3). The calculation for the downstream section is not as reliable (see Figure 5.41 and Table 5.3) as for the other two sections. The calculated values are very close to the simulated one for higher intercepted flow rate; however the estimation is not sufficiently precise for low flows.

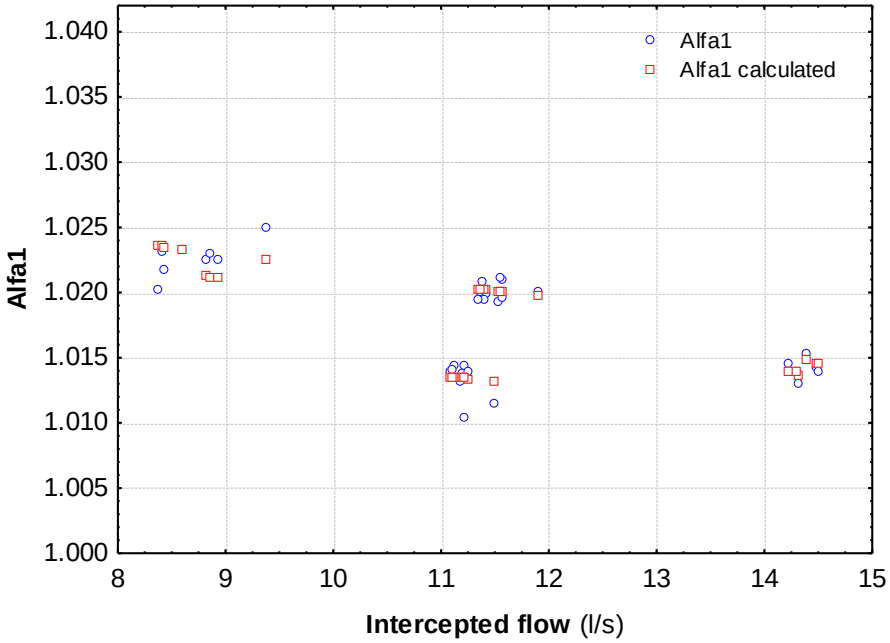

Figure 5.39 – Comparison of simulated and calculated kinetic energy coefficient at upstream section (S1)

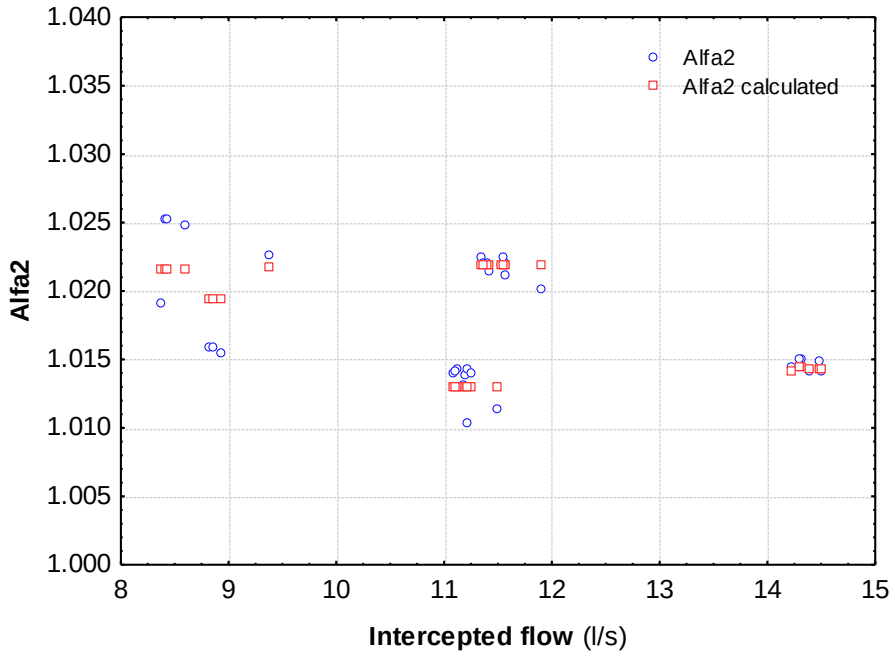

Figure 5.40 – Comparison of simulated and calculated kinetic energy coefficient at outer edge section (S2)

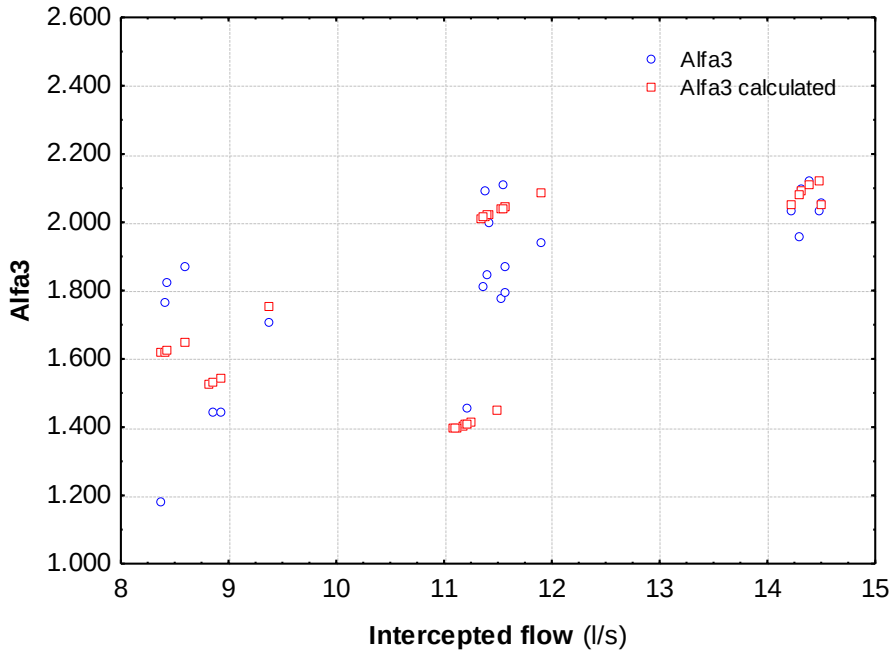

Figure 5.41 – Comparison of simulated and calculated kinetic energy coefficient at downstream section (S3)

This is due to the changing flow direction at the downstream edge. Higher flows and steeper longitudinal slopes decrease the uncertainty at the downstream section since the mixed flow (flow into the gully and from the gully in same time) disappears. An averaged kinetic energy and momentum coefficient for the three sections has been calculated. The averaged value gives more reliable results due to the elimination of uncertainty in the calculation of α at the downstream edge. Correlations between flow rate, surface slope, Reynolds number and the correction coefficients were calculated and a strong relationship was found between these hydraulic parameters (R^2 above 0.96). Figure 5.42 and Figure 5.43 shows the comparison of α and β as calculated by multiple linear regression equation and CFD simulation.

Table 5.3 – Regression summary of kinetic energy and momentum coefficient calculation for investigated sections

	S1		***S2***		***S3***	
	$\boldsymbol{\alpha}$	$\boldsymbol{\beta}$	$\boldsymbol{\alpha}$	$\boldsymbol{\beta}$	$\boldsymbol{\alpha}$	$\boldsymbol{\beta}$
R	0.9884	0.9186	0.9659	0.9207	0.7001	0.7833
R^2	0.9769	0.8438	0.9330	0.8477	0.4901	0.6136
p-level	0.0000	0.0000	0.0000	0.0000	0.0012	0.00006

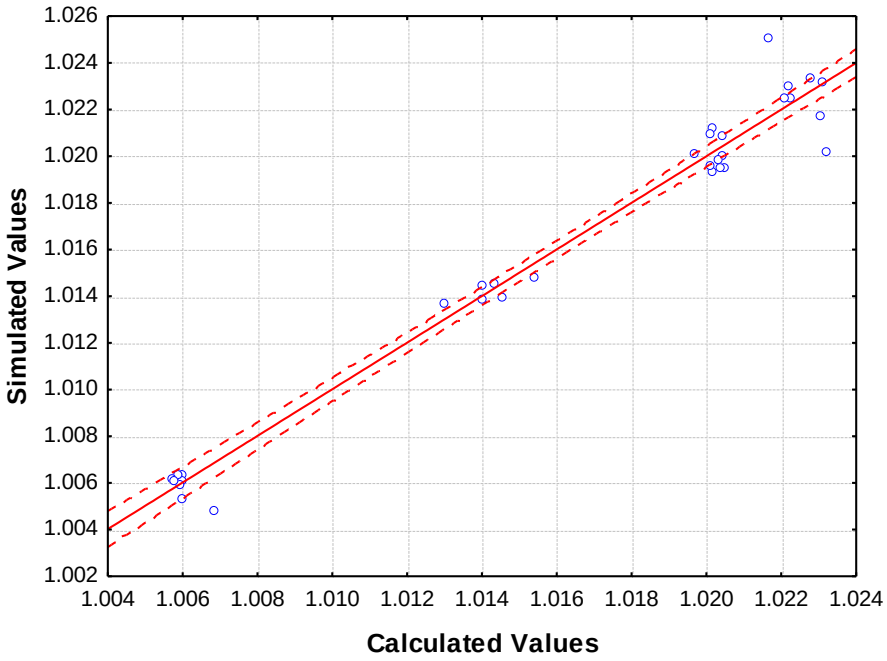

Figure 5.42 – Simulated vs. calculated values of kinematic energy coefficient

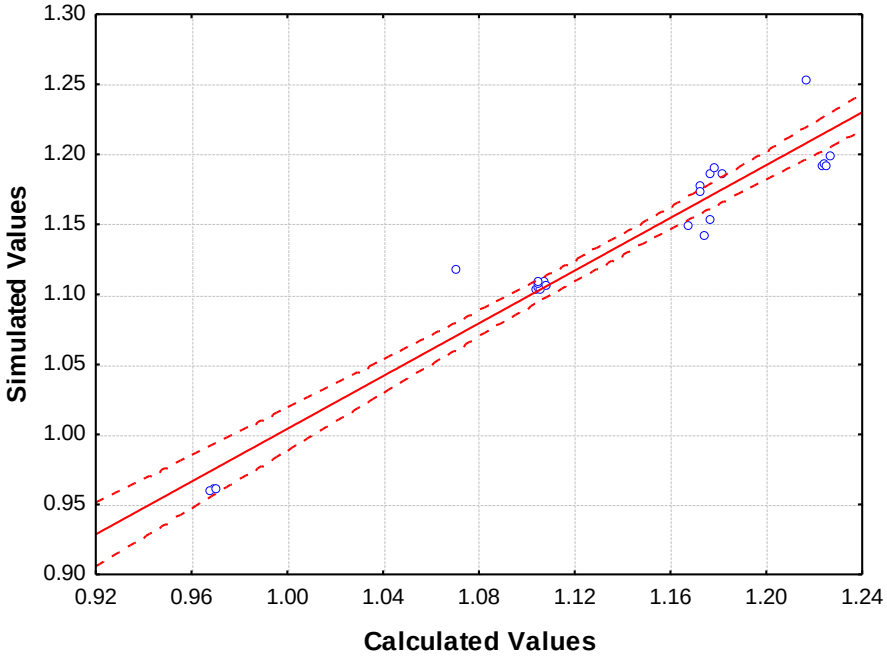

Figure 5.43 – Simulated vs. calculated values of momentum coefficient

The figures and the statistical parameters shows that the kinetic energy and momentum coefficient can be calculated reliably using the suggested equations.

After calculation of kinematic energy and momentum coefficients equation (5.17) was used to calculate the discharge coefficient.

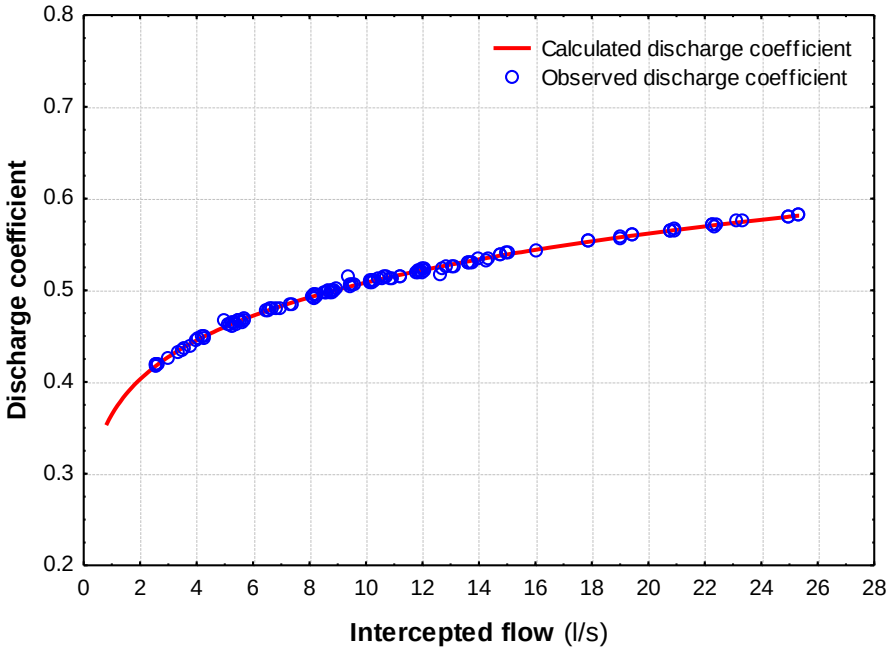

Figure 5.44 – Calculated and observed discharge coefficient

Figure 5.44 shows the relationship between intercepted flow rate and discharge coefficient. It can be seen that the discharge coefficient is not constant as its value is changing between 0.4 and 0.6. The theoretically determined 0.611 value has not been reached. There are two reasons for that: firstly higher inflows (resulting in higher depths over the grating) are needed to reach the orifice type behaviour of inlet; secondly the velocity head was considered in the discharge coefficient calculation, while many authors have neglected this term of the equation.

Chapter 6

Discussion and Conclusion

The studies presented in this thesis have been carried out in order to improve the understanding of the performance of local controls linking the above and below ground components of urban flood flows. The studies have involved the development of computational fluid dynamics models, validation of 3D and 2D/3D CFD models and a number of computational simulations on different gratings to better understand the effect of various geometric and road alignment on the intercepted flow. Simulations of surcharging flow conditions have also been completed. Analysis of simulation data has resulted in methods for determining the intercepted flow, a method for determining the efficiency of gate inlets, a method for determining the discharge coefficient and in numerical models for predicting the flow into and from gully pots. This Chapter will presents the main conclusion of the investigation, discuss the work completed and make suggestions for further work.

The numerical simulations of the different flow configurations provide a detailed insight into the dynamics of the flow. In particular the computational results provide all the flow details which are inaccessible by present experimental

techniques. They are used to prove the theoretical assumptions and yield the required information for analytical modelling.

This study shows that an advanced CFD model can be used to evaluate inlet performance due to different inlet geometries, longitudinal slope and cross slope instead of conducting large numbers of expensive laboratory tests.
The capabilities of interface capturing procedure based on Volume-of-Fluid method were assessed. The three dimensional computational model for two-phase flow with interface capturing was extended with two dimensional model and a link between the two computational domains. A special type of boundary has been used to connect the 2D and 3D domains. This switches velocity and pressure between fixed value and zero gradient depending on the direction of flow. The nesting has a significant positive effect on simulation time. Special attention has been made to mesh generation because the design and construction of a quality mesh is crucial to the success of the CFD analysis. The advantages and disadvantages of different mesh types have been assessed.
The models were validated by comparing the computational results with experimental results.

In Chapter 5 the distribution of intercepted flow among the edges of the grating has been investigated and it was shown that the contribution to intercepted flow from the outer edge of grating can be significant in certain conditions. This result apparently contradicts the observations that led NEENAH Foundry

Company and Engineering Laboratory Design to suggest that a negligible amount of the intercepted flow arrives through the outer edge of the inlet. It was shown that the amount of flow arriving from the outer edge of the grating is proportional to the cross-fall.

An improvement to the bypassing flow calculation was suggested. Different sloping conditions and inflows were tested and it was found that the included parameters give sufficient information to calculate the bypassing flow rate. It was shown that the empirical constant K_1 is a function of cross-slope.

Intercepted flow – depth functions were identified for three commonly used gratings. The regression analysis showed that the suggested equation can reliably predict the intercepted flow rate. Similarly to *Q-H* curve the *Efficiency-Q/d* curve was identified for the selected gratings.

Factors affecting grating efficiency have been investigated and yielded the following observations and conclusions. Under certain conditions a larger opening does not increase the effectiveness of a grating. This is because the dimensions and bar pattern influence the way that the flow is captured. Streamlines for different cross-fall scenarios were calculated and its effect on efficiency was investigated.

A regression relationship that related the approaching flow and water depth to inlet efficiency was identified.

The surcharging condition has been investigated to better understand the interaction between the surface and subsurface elements of urban flood models. A surcharge flow – depth function was identified as part of the investigation.

A realistic value for the street inlet can be calculated for certain flow conditions. The assumption that the discharge coefficient is constant and equal to 0.6 was proven to be wrong. A methodology for calculation of variable discharge coefficient was established.

Suggestions for further work

Numerical simulation of floods is very complex and interesting hydraulic problem. However, modelling is not only the objective but has serious ambitions in terms of reducing the flood consequences. All these problems are always further intensified by the combined effect of climate change and population growth. Below are listed some of the problems which could be in the focus of research in the future.

- Although the numerical models were validated successfully against water depths data collected during experimental tests, it would be interesting to make a further comparison of the velocity distribution at selected sections.
- Parasitic currents are attributed to the inaccurate determination of free surface and this is commonly encountered in VOF method based simulations. It has been found that the VOF method remain one of the most suitable methods for interface capturing in the framework of finite volume method without explicit free surface reconstruction. However, possibilities for improvement of interface sharpness with level set method should be further analysed.

- The computational 2D/3D link should be further extended to include tetrahedral type linkage, which would increase the flexibility and probably the effectiveness of the existing link.
- The gully inlets frequently blocked by debris. Proper design and management of these systems are essential to minimize flood damage and disruptions in urban areas during storm events. The effect of blockage has not been tested either experimentally or numerically. The CFD modelling of debris blockage and its effect on inlet efficiency would generate valuable knowledge both for designers and modellers as well.
- Similarly to debris, the sedimentation of gully pots and connected pipe system is frequently causing flood damage and disruption of urban transport. The developed multi-phase model can easily be extended into three phase model (water, air and sediment), which would provide a powerful tool to investigate the sedimentation process and could help to develop sediment management methods.
- The gratings has a significant effect on inlet efficiency. The applied CFD model could help to develop hidrodynamically optimal gratings.

References

Almedeij, A. O.,Houghtalen, R. J. (2003): Urban hydrology: hydraulics and storm water quality. *John Wiley & Son.*

Andersson, B. et al. (2012): Computational Fluid Dynamics for Engineers. *Cambridge: Cambridge University Press.*

ANSYS (2006): Fluent 6.3 User Guide.

Aris, R. (1989): Vectors, tensors and the basic equations of fluid mechanics. *Dover Publications.*

Aulisa, E., Manservisi, S., Scardovelli, R. (2003): A mixed markers and volume-of-fluid method for the reconstruction and advection of interfaces in two-phase and free boundary flows. *Journal of Computational Physics*, Volume 188, pp. 611-639.

Aulisa, E., Manservisi, S., Scardovelli, R. (2004): A geometrical area-preserving volume-of-fluid advection method. *Journal of Computational Physics*, Volume 192, pp. 355-364.

Balmforth, D., Digman, C., Kellagher, R., Butler, D. (2006): Design for exceedence in urban drainage - good practice

Bates, P. D., Lane, S. N., Ferguson, R. I. (2005): Computational Fluid Dynamics - Applications in Environmental Hydraulics.*John Wiley & Sons Ltd.*.

Blazek, J. (2001): Computational Fluid Dynamics: Principles and Applications. *Oxford: Elsevier.*

Borghei, S. M., Jalili, M. R., Ghodsian, M. (1999): Discharge coefficient for sharp-crested side weir in subcritical flow. *Journal of Hydraulic Engineering*, 125(10), pp. 1051-1056.

Bourchard, M. G., Towsend, R. D. (1984): Laboratory tests on the influence of grating pattern on street inlet hydraulics. Montreal, pp. 685-698.

Brackbill, J. U., Kothe, D. B., Zemach, C. (1992): A continuum method for modelling surface tension. *Journal of Computational Physics,* Volume 100, pp. 335-354.

Brennan, D. (2001): The numerical simulation of two-phase flows in settling tanks, *PhD thesis*

Brown, S. A., Stein, S. M., Warner, J. C. (2001): Urban Drainage Design Manual - Hydraulic Engineering Circular 22

Burgi, P. H., Gober, D. E. (1978): Hydraulic and Safety Characeristics of Selected Grate Inlets. *Transportation Research Record,* Issue No. 685, pp. 29-31.

Butler, D., Davies, J. W. (2004): Urban Drainage. *New York: Spon Press.*

Buxton, A., Tait, S., Stovin, V., Saul, A. (2002). Developments in a methodology for the design of engineered invert traps in combined sewer systems. *Water Science and Technology,* 45(7), pp. 133-142.

Chen, C. L. (1992): Momntum and Energy Coefficient Based on Power-Law Velocity Profile. *ASCE Journal of Hydraulic Engineering,* pp. 118 (11) 1571-1584.

Chow, V. T., 1959. *Open channel hydraulics.* New York: McGraw-Hill.

Croce, R., Griebel, M., Schweitzer, M. A. (2004): A Parallel Level-Set Approach for Two-Phase Flow Problems with Surface Tension in Three Space Dimensions

Cullivan, J. C., Williams, R. A., Dyakowski, T., Cross, C. R. (2004): New understanding of a hydrocyclone field and separation mechanism from computational fluid dynamics. *Mineral Engineering,* Volume 17, pp. 651-660.

Datei, C. (1966): Remarks on the effects of surface tension on the shape of fluid jets. Bressanone, *NATO Advanced Study Institute.*

De Martino, G. Ragone, A. (1979): L'influenza della viscosita e della tensione superficiale sull'efflusso da lucci. *Nouva Serie,* Volume XXVIII.

Despotovic, J., Tomanovic, A., Batinic, B. (1990): Hydraulic explanation and modelling of the capacity of urban storm drainage gutter pavment grate inlets. Osaka, Japan, pp. 18-23.

Djordjevic, S. (2009): 1D, 2D and 3D modelling of urban flooding. *Proceedings of the 8th International Conference on Urban Drainage Modelling,* Tokyo, Japane

El-Kashab, A., Smith, K. V. H. (1976): Experimental investigation of flow over side weirs. *Journal of Hydraulic Engineering,* 102(9), pp. 1255-1268.

Enright, D., Fedkiw, R., Ferziger, J., Mitchell, I. (2002): A hybrid particle level set method for improved interface capturing. *Journal of Computational Physics,* Volume 183, pp. 83-116.

ERCOFTAC (2000): Best Practice Guidlines for Industrial Computational Fluid Dynamics of Single-Phase Flows, Lausanne

Evans, E. P., Ashley, R., Hall, J. W., Pennin-Rowsell, E. C., Saul, A., Sayers, P. B., Thorne, C. R., Watkinson, A. (2004a): Foresight Flood and Coastal Defence Project: Scientific Summary Vol. I, Future Risks and their drivers, London, *Office of Science and Technology.*

Evans, E. P. , Ashley, R., Hall, J. W., Pennin-Rowsell, E. C., Saul, A., Sayers, P. B., Thorne, C. R., Watkinson, A. (2004b): A Foresight Flood and Coastal Defence Project: Scientific Summary: Volume 2, Managing future risks, London, *Office of Science and Technology.*

Fach, S., Sitzenfrei, R., Rauch, W.(2009): Determining the spill flow discharge of combined sewer overflows using rating curves based on computational fluid dynamics instead of the standard weir equation. *Water Science & Technology,* 60(12), pp. 3035-3043.

Fang, X., Jiang, S., Alam, S. R. (201): Numerical simulation of efficiency of curb-opening inlets. *Journal of Hydraulic Engineering,* 136(1), pp. 62-66.

Ferziger, J. H., Peric, M. (1996): Computational methods for fluid dynamics. *Springer.*

Galambos, I., Djordjevic, S., Tabor, G. (2009): FRMRC2 WP3.7 Improved understanding of interaction between surface and underground drainage systems*, Progress Report,* University of Exeter.

Gavis, J. (1964): Contribution of surface tension to expansion and contraction of capillary jets. *The Physics of Fluids.*

Ghetti, A. (1966): Effects of surface tension on the shape of liquid jets. Bressanone, *NATO Advanced Study Institute.*

Gomez, M., Russo, B. (2011): Methodology to estimate hydraulic efficiency of drain inlets. *Water Management,* 164(WM2), pp. 81-90.

Guo, J. C. (1997): Street Hydraulics and Inlet Sizing, Littleton, Colorado: *Water Resources Publication.*

Guo, J. C. (2000a): Design of grate inlets with clogging factor. *Advances in Environmental Research,* pp. 4, 181-186.

Guo, J. C. (2000b): Street Storm Water Conveyance Capacity. *ASCE Journal of Irrigation and Drainage Engineering,* pp. Vol. 126, No. 2.

Guo, J. C. (2000c): Street Storm Water Storage Capacity. *Journal of Environmental Research,* pp. Vol. 27, No. 6.

Hager, W. H. (1987.):Lateral outflow over side weirs. 113(4), pp. 491-504.

Hansen, G. A., Douglass, R. W., Zardecki, A. (2005): Mesh enhancement. London, *Imperial College Press.*

Harvie, D. J. E., Fletcher, D. F. (2000): A new volume of fluid advection algorithm: the stream scheme. *Journal of Computational Physics,* Volume 162, pp. 1-32.

Harvie, D. J. E., Fletcher, D. F. (2001): A new volume of fluid advection algorithm: The defined donating region scheme. *International Journal for Numerical Methods in Fluids,* Volume 35, pp. 151-172.

Hill, D. P. (1998): The computer simulation of dispersed two-phase flows*, PhD thesis*

Hirsch, C. (2007): Numerical Computation of Internal and External Flows*. Oxford: Elsevier.*

Hirt, C. W., Nichols, B. D. (1981): Volume of fluid (VOF) method for the dynamics of free boundaries. *Journal of Computational Physics,* Volume 39, pp. 201-225.

Honar, T., Keshavarzi, A. (2008): Effect of rounded-edge entrance on discharge coefficient of side weir in rectangular channels. *Irrigation and drainage.*Wiley Interscience

Huang, J. C., Weber, L. J., Lai, Y. G. (2002): Three dimensioanl numerical study of flows in open channel junctions. *Journal of Hydraulic Engineering,* 128(3), pp. 268-280.

Ismail, M., Nikraz, H. (2008): Experimental and Numerical Modeling of VersaTrap Type G. *Agricultural Engineering International,* December, Volume X..

Issa, R. I. (1986): Solution of the implicit discretized fluid flow equations by operator-splitting. *Journal of Computational Physics,* Volume 62, pp. 40-65.

Jarman, D. S., Faram, M. G., Butler, D., Tabor, G., Stovin, V. R., Burt, D., Thorp, E. (2008): Computational fluid dynamics as a tool for urban drainage system analysis: A review of applications and best practice*. Proceedings of 11th International Conference on Urban Drainage,* Edinburgh, Scotland

Jasak, H. (1996). Error analysis and estimation for the finite volume method with application to fluid flows*, PhD thesis*

Jiang, G. S., Peng, D. (2000): Weighted ENO Schemes for Hamilton-Jacobi Equations. *Journal of Scientific Computing,* Issue 21, pp. 21-26.

John Hopkins University (1956): The design of storm-water inlets*, Report of the Storm Drainage Research Committe,* Baltimore

Johnson, M. C. (2000): Discharge coefficient analysis for flat-topped and sharp-crested weir. *Irrigation Science,* Volume 19, pp. 133-137.

Kindsvater, C. E., Carter, R. W. (1957): Discharge characteristics of rectangular thin-plate weirs. *Proceedings,* December.Volume HY6.

King, H. W., Brater, E. F. (1963): Handbook of Hydraulics*. New York: McGraw-Hill.*

Kranc, S. C., Anderson, M. W. (1993): Investigation Discharge through Grated Inlets*, Technical Report,* University of South Florida.

Lafaurie, B., Nardone, C., Scardovelli, R., Zaleski, S., Zanetti, G. (1994): Modelling merging and fragmentation in muliphase flows with SURFER. *Journal of Computational Physics,* Volume 113, pp. 134-147.

Larson, C. L. (1947): Investigation of Flow Through Standard and Experimental Grate Inlets for Street Gutters*, Project Report,* St. Antony Falls Hydraulic Laboratory University of Minesota.

Leandro, J., Chen, A., Savic, D. A. (2009): Comparison of 1D/1D and 1D/2D coupled (sewer/surface) hydraulic models for urban flood simulation. *Journal of Hydraulic Engineering ASCE,* 135(6), pp. 495-504.

Leonard, B. P. (1991): The ULTIMATE conservative difference scheme applied to unsteady one-dimensional advection. *Computational Methods in Applied Mechanics and Engineering,* Volume 19, pp. 17-74.

Linquist, E. (1929): Precise weir measurement. *Transaction,* Volume 93.

Li, W. H., Geyer, J. C., Benton, G. S. (1951): Hydraulic Behaviour of Storm-Water Inlets: I. Flow into Gutter Inlets in straight Gutter without Depression. *Sewage and Industrial Wastes,* 23(1), pp. 34-46.

Li, W. H., Goodel, B. C., Geyer, J. C. (1954): Hydraulic Behavior of Storm-Water Inlets: IV. Flow into Depressed Combination Inlets. *Sewage and Industrial Wastes,* 26(8), pp. 967-975.

Lopez, J., Hernandez, J., Gomez, P., Faura, F. (2004): A volume of fluid method based on multidimensional advection and spline interface reconstruction. *Journal of Computational Physics,* Issue 195, pp. 718-742.

Mangani, L. (2008): Development and validation of an object oriented CFD solver for heat transfer and combustion modeling in turbomachinery applications*, PhD thesis*

MARNET-CFD, (1999): Best practice guidlines for marine application of computational fluid dynamics,*Project Report*

Martino, G. D., Ragone, A. (1984): Effects of viscosity and surface tension on slot weir flow. *Journal of Hydraulic Research,* 22(5), pp. 327-341.

Matthew, G. D. (1963): On the influence of curvature, surface tension and viscosity on flow over round-crested weirs*. Proceedings of the Institute of Civil Engineering, ASCE*, pp. 511-524.

Mays, L. R. (2001): Water Resources Engineering. *New York: John Wiley & Son.*

McEnroe, B. M., Wade, R. P., Smith, A. K. (1999): Hydraulic performance of curb and gutter inlets*, Technical Report*, Department of Civil and Environmental Engineering University of Kansas

Menter, F. R. (1992): Assessment of higher order turbulence models for complex two- and three-dimensional flowfields*, Project Report,* NASA-TM-103944*,* National Aeronautics and Space Administration (NASA).

Menter, F. R. (2002): CFD Best Practice Guidlines for CFD Code Validation for Reactor Safety Applications*, Technical Report*, FIKS-CT-2001-00154, ECORA.

Mignot, E. Bonkadari, H., Knothe, P., Lipene Kouyi, G., Bessette, A., Riviere, N., Bertrand-Krajewski, J. L., (2012): Experiments and 3D simulations of flow structures in junctions and their influence on location of flow meters. *Water Science and Technology.*

Mostkow, M. A. (1957): A theoretical study of bottom type water intakes. *La Houille Blanche,* 4(12), pp. 570-580.

NEENAH Foundry Company, Engineering Laboratory Design (1987): Inlet grate capacities for gutter flow and ponded water*, Research Report*

Noh, W. F., Woodward, P. (1976): SLIC (Simple Line Interface Calculations). *Lecture Notes in Physics,* Volume 59, pp. 330-340.

Noseda, G. (1956): Correnti permanenti con portata progressivamente decrescente, defluenti su griglie di fondo. *L'Energia Electrica,* 33(6), pp. 565-584.

OpenCFD (2008):OpenFOAM, The Open Source CFD Toolbox*, User Guide*

Osher, S. J., Sethian, J. (1988): Fronts Propagating with Curvature Dependent Speed: Algorithms Based on Hamilton-Jacobi Formulations. *Journal of Computational Physics,* Issue 79, pp. 12-49.

Osher, S., Sethian, J. A. (1988): Fronts propagating with curvature dependent speed: Algorithms based on Hamilton-Jacobi formulations. *Journal of Computational Physics,* Issue 79, pp. 12-49.

Pan, D., Chang, C. H. (2000): The capturing of free surfaces in incompressible multi-fluid flows. *International Journal of Numerical Methods in Fluids,* Volume 33, pp. 203-222.

Pantakar, S. V. (1980): Numerical heat transfer and fluid flow, *Hemisphere Publishing Corporation.*

Peric, M. (1985): A finite volume method for the prediction of three-dimensional flow in complex ducts*, PhD thesis.*

Pilliod, J. E., Pucket, E. G. (2004): Second-order accurate volume-of-fluid algorithms for tracking material interfaces. *Journal of Computational Physics,* Issue 199, pp. 465-502.

Pointwise (2008): Pointwise User Manual

Ranga Raju, K. G., Prasad, B., Gupta, S. K. (1979): Side weir in rectangular channel. *Journal of Hydraulic Division,* 105(5), pp. 547-554.

Rehbock, T. (1929): Hydraulic laboratory practice. *New York: American Society of Mechanical Engineers*

Renardy, Y., Renardy, M. (2002): PROST : A Parabolic Reconstruction of Surface Tension for the Volume-Of-Fluid Method. *Journal of Computational Physics,* Volume 183, pp. 400-421.

Rider, W. J., Kothe, D. B. (1998): Reconstructing volume tracking. *Journal of Computational Physics,* Volume 141, pp. 112-152.

Rudman, M. (1997): Volume-tracking methods for interfacial flow calculations. *International Journal for Numerical Methods in Fluids,* Volume 24, pp. 671-691.

Rusche, H. (2002): Computational Fluid Dynamics of dispersed two-phase flows at high phase fractions, *PhD thesis*

Russo, B., Gomez, M., Martinez, P., Sanchez, H. (2005): Methodology to study the surface runoff in urban streets and the design inlet systems. Application in a real case study. *Proceedings of the 10th International Conference on Urban Drainage,* Copenhagen, Denmark.

Sabtu, N. (2012): FRMRC2: Work Package 3.7, *Progress Report*

Sain-Gobain Pipelines (2007): Ductile Iron Access, Covers & Gratings - Product Specification Guide, *Catalogue*

Sarginson, E. J. (1972): The influence of surface tension on weir flow. *Journal of Hydraulic Research,* 10(4).

Sarpkaya, T. (1958): Discharge characteristics of rectangular thin-plate weirs. *Discussion Proceedings,* Volume HY2, ASCE.

Scardovelli, R., Zaleski, S. (2003): Interface reconstruction with least-square fit and split Eulerian–Lagragian advection. *International Journal of Numerical Methods in Fluids,* Issue 41, pp. 251-274.

Schmitt, F., Milis, V., Bertrand-Krajewski, J. L., Laplace, D., Chebbo, G. (1999): Numerical modelling of bed load sediment traps in sewer systems by density currents. *Water Science and Technology,* 39(9), pp. 153-160.

Schmitt, T. G., Thomas, M., Ettrich, N. (2004): Analysis and modeling of flooding in urban drainage systems. *Journal of Hydrology,* Issue 299, pp. 300-311.

Schuetz, S., Mayer, G., Bierdel, M., Piesche, M., (2004): Investigation on the flow and separation behaviour of hydrocyclones using computational fluid dynamics. *International Journal of Mineral Processes,* Volume 73, pp. 229-237.

Shakibainia, A., Tabatabai, M. R., Zarrati, A. R. (2010): Three dimensional numerical study of flow structure in channel confluence. *Canadian Journal of Civil Engineering,* Issue 37, pp. 772-781.

Singh, R., Manivannan, D., Satyanarayana, T. (1994): Discharge coefficient of rectangular side weirs. *Journal of Irrigation and Drainage Engineering,* 120(4), pp. 814-819.

Spalding, D. B. (1974): A method for computing steady and unsteady flow possessing discontinuities of density*,* Research Report.

Spaliviero, F., May, R. W. (1998): Spacing of road gullies. Hydraulic performance of BS EN 124 gully gratings*, Technical Report*, HR Wallingford

Stovin, V. R., Saul, A. J. (1998): A computational fluid dynamics (CFD) particle tracking approach to efficiency prediction. *Water Science & Technology,* 37(1), pp. 285-293.

Sturm, T. W. (2001): Open Channel Hydraulics. International Edition, *New York: McGraw Hill.*

Subramanya, K., Awashty, S. C. (1972): Spatially varied flow over side weirs. *Journal of Hydraulic Division,* 98(1), pp. 1-10.

Subramanya, K., Senputa, D. (1981): Flow through bottom racks. *Indian Journal of Technology,* 19(2), pp. 64-67.

Sussman, M., Pucket, E. G. (2000): A coupled level set and volume-of-fluid method for computing 3 D and axisymmetric incompressible two-phase flows. *Journal of Computational Physics,* Issue 162, pp. 301-337.

Swamee, P. K., Pathak, S. K., Mohan, M., Agrawal, S. K., Ali, M. S. (1994): Subcritical flow over rectangular side weir. *Journal of Hydraulic Engineering,* 120(1), pp. 212-217.

Swift, H. W. (1926): Orifice flow as effected by yviscosity and capillarity. *Philosophical Magazine,* Issue 10.

Tomanovic, A., Despotovic, J., Batinic, B. (1990): Hidraulico objasnjenje prijemne moc'I slivnika kisne kanalizaciie*. Proceeding of 10th JDHI Conference,* Sarajevo, pp. 1-8, [in Serbo-Croat]

Ubbink, O. (1997): Numerical prediction of two fluid system with sharp interface*, PhD thesis*

Ubbink, O., Issa, R. I. (1999): A method for capturing sharp fluid interface on arbitrary meshes. *Journal of Computational Physics,* Volume 153, pp. 26-50.

Valentin, M. G., Russo, B. (2007): Hydraulic Efficiency of Macro-inlets*. Proceedings of NOVATECH 2007*

Versteeg, H. K., Malalasekera, W. (2007): *A*n Introduction to Computational Fluid Dynamics*.* Harlow, England: Pearson Education Limited.

Weller, H. G., Tabor, G., Jasak, H., Fureby, C. (1998): A tensorial approach to computational continuum mechanics using object oriented techniques. *Computers in Physics*, Volume 12, pp. 620-631,

Wilkening, H., Baraldi, D., Heitsch, M. (2006): On the importance of validation when using commercial CFD codes in nuclear reactor safety. *Proceedings of CFD4NRS,* Garching, pp. 525-538.

Xiao, F., Honma, Y., Kono, T. (2005): A simple algebraic interface-capturing scheme using hyperbolic tangent function. *International Journal for Numerical Methods in Fluids,* Volume 48, pp. 1023-1040.

Yoloi, K. (2007): Efficient implementation of THINC scheme: a simple and practical smoothed VOF algorithm. *Journal of Computational Physics,* Volume 226, pp. 1985-2002.

Youngs, D. L. (1982): Time-dependent multimaterial flow with large fluid distortion. In: *Numerical Methods for Fluid Dynamics.* New York: Academic Press, pp. 273-285.

Zikanov, O. (2010): Essential Computational Fluid Dynamics. New Jersey: John Wiley & Sons.